# Control of the stability of pulsed 2 µm lasers

JAMES BROOKS

A thesis presented in partial fulfilment of the requirements for the degree of Doctor of Engineering

Department of Physics,

University of Strathclyde,

Glasgow, UK

April, 2019

This thesis is the result of the author's original research. It has been composed by the author and has not been previously submitted for examination which has led to the award of a degree.

Signed:
Date:

# Abstract

Pulse-to-pulse fluctuations in the output of Q-switched 2 µm lasers are a major obstacle to commercialisation. This jitter is present in all pulse parameters: build-up time, pulse duration, peak power and energy. The severity of the jitter is dependent on how far above threshold the laser can be pumped; lower gain coupled with reabsorption losses contribute to the level of jitter observed in 2 µm lasers. This thesis presents a detailed investigation into the jitter in a Q-switched Tm:YAP laser and tests methods of reducing the jitter. Target jitter levels of <1 ns for the build-up time and <3 % for the energy were identified based on similar commercial Nd-based systems.

A full characterisation of the level of jitter in all pulse parameters was undertaken and the results were used as a benchmark to gauge the efficacy of subsequent improvements.

The use of etalons to limit the laser mode content increased the build-up time jitter by an order of magnitude and the energy jitter by a factor of three. This is thought to be due to increased mode competition.

The cavity was transferred to a ruggedised housing with the minimum degrees of freedom required for alignment. This was done to reduce the variation of losses due to mechanical vibrations and was successful in reducing the jitter. This housing also allowed the purging of the cavity with dry air to reduce atmospheric water absorption. Through this combination, the build-up time jitter was reduced to 1.9 ns and pulse energy jitter to 1.8 %, representing the best performance achieved in this work.

The pre-lase technique was employed to enforce laser oscillation on a single longitudinal mode. Pre-lase is a two-step process that allows the build-up of a weak single-frequency pulse that seeds the main output. This led to increased jitter in the build-up time (to 19 ns) and energy (to 16 %) due to the inherent levels of jitter in the high-threshold seed pulse.

# Contents

# List of Figures

# List of Tables

# Acknowledgements

I would like to take this opportunity to thank the many people who helped me get to this juncture. First to my supervisors, Prof. Alan Kemp, Dr Gerald Bonner and Dr David Stothard. Thank you for this opportunity, your guidance and support.

Thanks are also due to John Leck for his assistance with the mechanical design in chapter 4 and to Barry Ferns for his help with all things electrical, the pre-lase electronics in chapter 5 particularly. Thanks also to David Jones for designing said circuit.

My thanks go also to Elforlight Ltd for the loan of a Pockels cell and to Emerson Cascade for the thin-film polariser used throughout this work. Without these critical components, this work would not have been possible.

My gratitude also to the staff and students at Fraunhofer CAP for their help, jokes, weird lunch-time discussion topics and local pub knowledge!

Finally, it goes (almost) without saying, thanks are most definitely due to my family for supporting (and occasionally pushing) me in this endeavour.

# Chapter 1

# Introduction

Q-switching as a method of producing pulses of coherent light has been understood since almost the invention of the laser itself; it was first demonstrated in 1962 [1], with the first experimental realisation of the laser in 1960 [2]. This has led to such lasers being employed in laboratories and products across the world. However, such lasers emitting around 2 µm directly are not available commercially to the author's knowledge. One reason for this is that pulse-to-pulse variations (known as jitter) are currently too large in such lasers for a commercially-viable system to be marketed. This thesis aims to present the outcomes of the research study as defined below with a view to addressing this commercial opportunity.

## 1.1 Research problem

**The purpose of this research was to investigate the causes of jitter in a Q-switched thulium laser, to identify potential routes to jitter-free operation and to evaluate these methods of reducing jitter. Such methods should aim to be as simple as possible and be applicable to other laser systems that suffer from jitter.**

## 1.2 Thesis overview

This thesis is structured as follows. Chapter 1 will introduce the materials that can be used to generate 2 µm laser light before discussing Q-switching as a method of obtaining high-peak-power pulses and finally defining the problem of jitter. Chapter 2 will cover the laser under investigation and the initial characterisation of the jitter in the system. Chapter 3 will discuss the first attempts made at reducing the jitter by controlling the mode content of the laser. Chapter 4 will describe the design and implementation of a ruggedised housing for the system. Chapter 5 will discuss the application of the pre-lase technique to the laser in a further effort to control the mode content. Chapter 6 will summarise the thesis and set out the best combination of techniques for controlling the jitter in a Q-switched laser.

## 1.3 Introduction to 2 µm lasers

Pulsed 2 µm lasers have applications in materials processing [3] and laser surgery [4–7] due to the strong absorption of plastics and water respectively around this wavelength [3]. Lasers operating around 2 µm are useful for remote sensing [6, 8, 9] due to the "eye-safe" wavelength [10, 11]. Depending on the sensing application, atmospheric transmission (for LIDAR) [10] or absorption features (for gas sensing, particularly $H_2O$ and $CO_2$) [11] around 2 µm can be taken advantage of. Finally, 2 µm lasers can be used to pump non-linear materials to reach the 3 µm – 12 µm range [5, 8, 12]; this unlocks applications in spectroscopy [13, 14] and defence [5, 13]. 2 µm lasers are used in these cases as they are able to reach the desired wavelength range in a single non-linear step, which improves the efficiency of the system. Most non-linear crystals used to access the 3 µm – 12 µm range exhibit significant losses at 1 µm which precludes pumping with more established Nd or Yb lasers [15].

There are several options for producing a 2 µm laser: diode lasers, V(E)CSELs, frequency converted 1 µm lasers, fibre lasers and bulk crystalline or glass lasers. As pulses with high peak power and pulse energy are desired, Q-switching (see section 1.4) will be used. As such, there are problems with a number of these possibilities. First, diode lasers and V(E)CSELs are not suitable for Q-switching due to the short lifetime of semiconductor lasers (a long lifetime is desirable as it allows more energy to be stored and therefore extracted in the pulse [16]). Fibre lasers suffer from detrimental non-linear effects at high powers including stimulated Raman and Brillouin scattering [17] due to the high power density being maintained over long interaction lengths [18]; furthermore, the high power can lead to damage or failure of the fibre [19]. Frequency converting a 1 µm laser adds a complicated non-linear step and limits efficiency, especially if the application requires a subsequent non-linear step to longer wavelengths [20]. Therefore, bulk solid-state lasers that directly emit 2 µm light will be used for this work. The following section will introduce the ions that can emit at 2 µm, section 1.4 will discuss Q-switching as the method used to obtain pulses of laser light.

### 1.3.1 Potential ions for 2 µm emission

The two main ions used to obtain 2 µm emission are the trivalent rare-earth ions thulium ($Tm^{3+}$) and holmium ($Ho^{3+}$). Other options are available including erbium (Er), cobalt (Co) and uranium (U). While lasers based on these ions have been demonstrated (see for example reference [21]), they suffer from a number of disadvantages. Erbium emitting at 2.94 µm (Er:YAG) or 2.8 µm (Er:YLF) suffers from a large quantum defect [21] and is at a longer wavelength than this work is interested in. A Co:$MgF_2$ laser was demonstrated to be tunable between 1.75 µm – 2.50 µm [22]; however, the laser suffered substantial losses from nonradiative decay and had a small gain cross-section [23]. Uranium has also been demonstrated as a laser material operating at 2.6 µm [24] but its radioactivity precludes its use in this work.

#### 1.3.1.1 Thulium

Thulium can be used to create lasers that operate in the range 1.85 µm – 2.05 µm [3]. Thulium has a useful pumping scheme based on a cross-relaxation process which is very efficient in most hosts and allows efficient pumping with widely available diode lasers [3]. Figure 1.1 shows the cross-relaxation process. In this process, one ion is excited to the $^3H_4$ level, this ion then transitions to the $^3F_4$ state. Due to the near

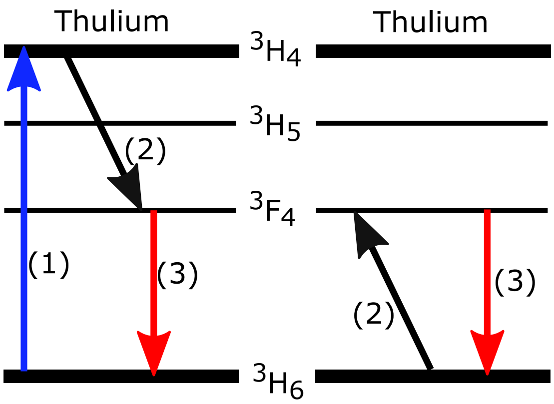

Figure 1.1: Energy levels and transitions of interest in thulium. (1) Pumping, (2) cross-relaxation, (3) laser transitions. Adapted from [25].

resonance of the $^3H_4$ – $^3F_4$ and $^3H_6$ – $^3F_4$ transitions [25], the energy released in the transition from pump level ($^3H_4$) to upper laser level ($^3F_4$) is absorbed by a second ion which is excited from the ground state ($^3H_6$) to the upper laser level ($^3F_4$), as shown in figure 1.1. This process therefore reduces the effective quantum defect compared to that expected from comparing the pump and laser wavelengths (around 795 nm and 1940 nm respectively). This process efficiently populates the upper laser level but is strongly dependent on the thulium ion separation which is controlled by the concentration [25] - a higher concentration improves the efficiency of the cross-relaxation process. The cross-relaxation process is often called the 2-for-1 pumping process as two ions in the upper laser level can be generated from one pump photon [21].

Other pumping schemes have been proposed in some hosts. Pumping of $Tm:Lu_2O_3$ at 1.2 µm was reported to be efficient because a lower doping could be used; this was due to both the higher absorption of this wavelength in this particular host and the the fact that there is no cross-relaxation in this scheme [26–28]. In-band pumping of Tm-doped fibre lasers has also been demonstrated using either another Tm-doped fibre [29] or Tm:YLF [30] as the pump source around 1910 nm. The downside of pumping at either 1.2 µm or 1.9 µm is the need for an extra laser as laser diodes at these wavelengths suffer from low ($\sim 10\,\%$) electro-optical efficiencies [31].

Three common crystalline hosts for thulium will now be discussed; bulk glass hosts have been discounted due to their generally lower thermal conductivity and higher

Table 1.1: Comparison of thulium-doped crystals.

| Property | Tm:YAG [ref.] | Tm:YLF [ref.] | Tm:YAP [ref.] |
|---|---|---|---|
| Crystal symmetry | Isotropic | Uniaxial | Biaxial |
| $\lambda_\mathrm{p}$ (nm) | $\sim$ 785 [32] | $\sim$ 792 [3] | $\sim$ 795 [4] |
| $\sigma_\mathrm{a}(\lambda_\mathrm{p})$ (cm$^2$) | $6.5 \times 10^{-21}$ [33] | $6.5 \times 10^{-21}$ [34] | $9.1 \times 10^{-21}$ [33] |
| $\lambda_\mathrm{L}$ (µm) | 1.87 – 2.16 [9] | 1.70 – 1.95 [35] | 1.80 – 2.02 [4] |
| $\sigma_\mathrm{e}(\lambda_\mathrm{L})$ (cm$^2$) | $2.2 \times 10^{-21}$ [36] | $3.3 \times 10^{-21}$ [36] | $5.0 \times 10^{-21}$ [33] |
| $\sigma_\mathrm{a}(\lambda_\mathrm{L})$ (cm$^2$) | $0.077 \times 10^{-21}$ [33] | $0.28 \times 10^{-21}$ [37] | $0.486 \times 10^{-21}$ [33] |
| $\tau$ (ms) | 11 [32] | 18 [34] | 4.4 [38] |
| $k$ (Wcm$^{-1}$K$^{-1}$) | 0.13 [39] | 0.06 [40] | 0.11 [39] |

thresholds compared to single crystals [21]. A high thermal conductivity is desirable as the crystal will be pumped hard to store a large amount of energy which also deposits heat that needs dissipating. A lower threshold is important as more energy can be extracted by the pulse if the system has a low threshold for reasons that will be discussed in section 1.4. While thulium-doped tungstates and sesquioxides are available, this work will focus on the more well-established YAG, YLF and YAP hosts. A comparison of the key properties of Tm:YAG, Tm:YLF and Tm:YAP is presented in table 1.1 and are discussed below. All three crystals are available commercially. In the table, $\lambda_\mathrm{p}$ ($\lambda_\mathrm{L}$) is the pump (laser) wavelength, $\sigma_\mathrm{a}(\lambda_\mathrm{p})$ ($\sigma_\mathrm{a}(\lambda_\mathrm{L})$) is the absorption cross-section at the pump (laser) wavelength, $\sigma_\mathrm{e}(\lambda_\mathrm{L})$ is the emission cross-section at the laser wavelength, $\tau$ is the upper laser level lifetime and $k$ is the thermal conductivity.

**Tm:YAG** Perhaps the most well known crystalline host material, yttrium aluminium garnet (YAG) is a good laser host due to its large thermal conductivity (0.13 W cm$^{-1}$ K$^{-1}$ [39]), mechanical robustness and good optical quality [41]. Thulium doped in YAG has a stimulated emission cross-section of $\sigma_\mathrm{e} = 0.22 \times 10^{-20}$ cm$^2$ (at an emission wavelength of 2011 nm) [36] and a peak in its absorption around 785 nm [32]. For comparison, the stimulated emission cross-section of Nd:YAG is around $2.8 \times 10^{-19}$ cm$^2$ (at an emission wavelength of 1064 nm) with the main absorption band for diode pumping around 808 nm [21] . With a thulium concentration above 3 % (recall that higher concentrations improve the cross-relaxation efficiency), there is efficient cross-relaxation [32] and at 12 % thulium concentration the pumping quantum efficiency is nearly 2 [9]. Tm:YAG has a fluorescence lifetime of $\tau \sim 11\,\mathrm{ms}$ at 4 % thulium [32].

Tunable output between 1.87 µm – 2.16 µm was demonstrated in a Tm:YAG laser with 12 % thulium concentration with the fluorescence peak at 2.02 µm [9]. The peak fluorescence wavelength was reported to be $\lambda \sim 2.01\,\mu\mathrm{m} - 2.02\,\mu\mathrm{m}$ for 6 % thulium concentration [3,41]. The main problem with YAG is that its cubic structure means that there is no polarisation selection in the gain medium. This becomes a drawback in high power lasers when thermally-induced birefringence causes depolarisation losses [41].

**Tm:YLF** Another potential host for thulium is yttrium lithium fluoride (YLF), chemical formula $\mathrm{LiYF_4}$. Tm:YLF emits in the range $\lambda \approx 1.7\,\mu\mathrm{m} - 1.95\,\mu\mathrm{m}$ [35] with an emission cross-section of $0.33 \times 10^{-20}\,\mathrm{cm}^2$ at a wavelength of 1902 nm [36]. Tm:YLF has a fluorescence lifetime of 18 ms [34]. The optimum thulium concentration has been found to be 2 % – 3.5 % in YLF [42] and the peak of its absorption is at 792 nm [3].

YLF has a natural birefringence allowing lasers based on it to produce linearly polarised outputs with very low depolarisation losses [35]. Also, there is only a weak thermal lensing effect in YLF (especially for the $\sigma$ polarisation [43]). This is because the refractive index of YLF decreases with increasing temperature, producing a negative thermal lens; this is partly offset by the positive lens caused by the bulging of the crystal end faces [43,44]. However, Tm:YLF has a low thermal stress fracture limit [44] ($\sim 40\,\mathrm{MPa}$ which is around 5 times lower than YAG [45]) and so requires careful thermal management to prevent cracking during operation.

**Tm:YAP** Yttrium aluminium perovskite (YAP) has the chemical formula $\mathrm{YAlO_3}$ and has similar mechanical properties to YAG [25]. In particular, it has a similar thermal conductivity ($0.11\,\mathrm{W\,cm^{-1}\,K^{-1}}$ [39]) and optical transmission range [46]. Tm:YAP has an effective stimulated emission cross-section of $0.5 \times 10^{-20}\,\mathrm{cm}^2$ (more than double that in Tm:YAG) at 1936 nm [33]. Unlike YAG and YLF, YAP is a biaxial crystal and so its properties differ depending on the crystal axis being considered (in YAG all axes are equivalent and in YLF two axes are the same). YAP is an orthorhombic crystal

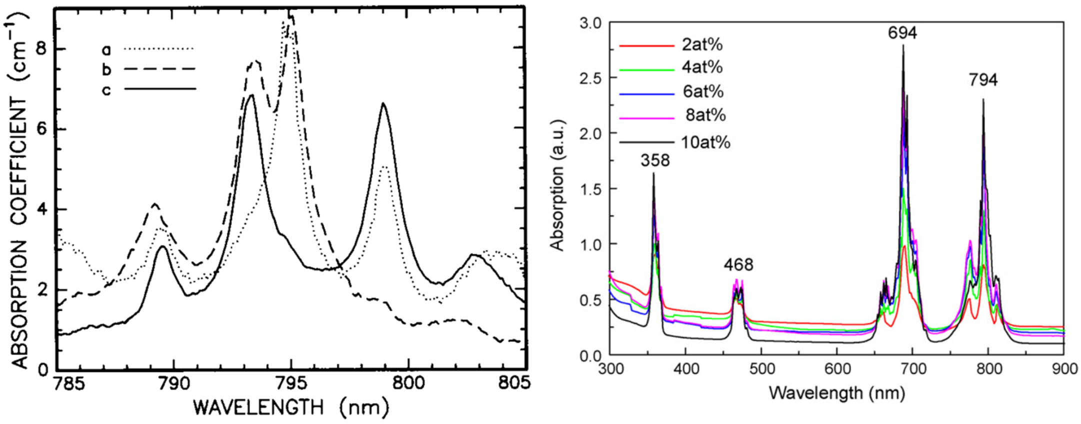

(a) (b)

Figure 1.2: (a) Absorption spectra for Tm(4 %):YAP for light polarised along the *a*-, *b*- and *c*-crystal axes [4]. (b) Absorption spectra for Tm:YAP at different thulium concentrations [47].

belonging to the $D_{2h}^{16}$ space group, this group's lattice parameters can be described using one of two equivalent notations, $P_{nma}$ and $P_{bnm}$, which are related by the transformation $(a,b,c)P_{bnm} \leftrightarrow (c,a,b)P_{nma}$ [37]. This thesis will use the $P_{nma}$ notation when referring to the crystal axes.

Tm:YAP has absorption peaks at 795 nm and 793 nm (depending on which axis the light is polarised along, see figure 1.2a) [4]. For light polarised along the *a*-axis, it is best to pump at 795 nm and at 793 nm for the *c*-axis; the absorption feature for light polarised along the *b*-axis is broad enough to absorb at either pump wavelength. Figure 1.2b shows the effect of Tm concentration on the absorption spectrum of Tm:YAP; from this graph, it can be seen that higher concentrations of thulium lead to increased absorption. An efficient excitation of ions throughout the gain medium is important to minimise reabsorption losses, therefore a higher thulium concentration is desirable.

Tm:YAP has a fluorescence lifetime (for the transition of interest from the $^3F_4$ level) of 4.4 ms [38, 48] and emits in the range $\lambda \sim 1.80\,\mu m - 2.02\,\mu m$ [4] (see figure 1.3a). Figure 1.3b shows that increasing the thulium concentration above 4 at.% reduces the peak fluorescence intensities emitted due to concentration quenching [47]. Combining this fact with the concentration-dependent absorption spectra in figure 1.2b leads to the conclusion that the optimum doping level for Tm:YAP is around 4 at.% [47].

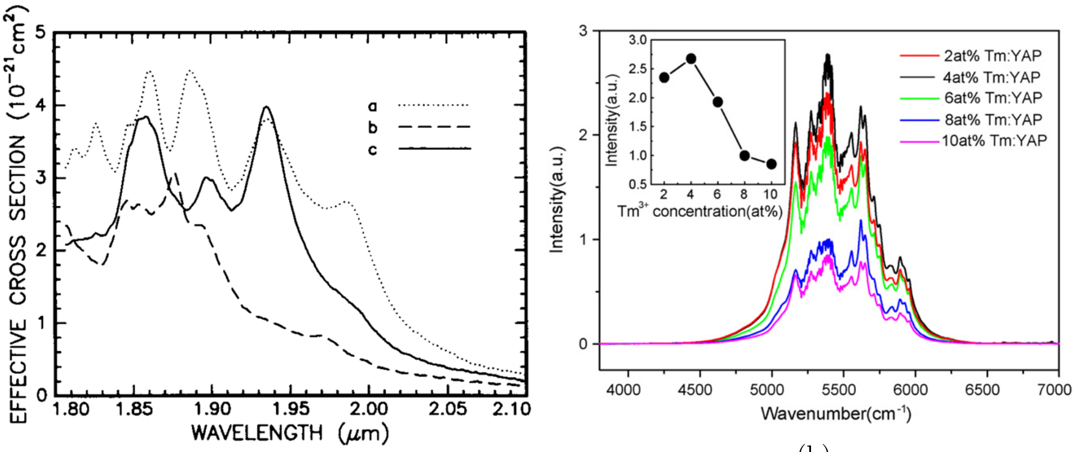

(a)

(b)

Figure 1.3: (a) Emission spectra for Tm(4 %):YAP for light polarised along the *a*-, *b*- and *c*-crystal axes [4]. (b) Fluorescence spectra for Tm:YAP at different thulium concentrations [47]. For comparison, $4000\,\text{cm}^{-1}$ – $7000\,\text{cm}^{-1}$ is equivalent to 2500.00 nm – 1428.57 nm.

As shown in figures 1.2a and 1.3a, the absorption and gain properties of Tm:YAP are polarisation dependent; therefore the laser performance can be influenced by crystal orientation [13]. It was found that the *c*-cut (meaning the cavity axis is aligned to the crystal *c*-axis) gives superior performance (greater output power in this case) over the *a*-cut [13]. However, this orientation will oscillate on the $\lambda \sim 1.99\,\mu\text{m}$ peak as well as at $\sim 1.94\,\mu\text{m}$ which may not be desirable for all applications.

Tm(4 at.%):YAP was chosen as the gain medium for this work due to its relatively high thermal conductivity and stimulated emission cross-section as well as its naturally polarised output (it will be shown in section 1.4 that this complements the chosen method of Q-switching). An *a*-cut crystal was used to ensure the laser oscillated on the same gain peak (at 1.94 μm) regardless of the losses in the cavity (see section 1.3.2), this was done to ensure fair comparison between output couplers.

#### 1.3.1.2 Holmium

Although Tm:YAP was used as the gain medium in this work, holmium will be briefly discussed here for completeness as it is the other main ion used for 2 μm emission. Holmium emits in the range 1.8 μm – 2.2 μm dependant on the host [36,49–51]. Holmium absorbs around 1.9 µm [35, 52]; potential pump sources are therefore thulium lasers operating around 1.9 µm [12, 53], laser diodes at ∼795 nm if the crystal is co-doped with thulium [25, 52] or, more recently with the invention of high-power laser diodes at the appropriate wavelength, direct diode-pumping at ∼1.9 µm [54–56].

The pump scheme for the co-doped system is similar to that for thulium and will be described here. Thulium absorbs pump radiation (usually from a laser diode around 795 nm) then energy transfer takes place between the thulium and holmium to create a population inversion in the holmium ions [25]. This energy transfer method of pumping holmium takes advantage of the cross-relaxation process in thulium (as described in section 1.3.1.1). In order to make creating a population inversion easier, it is usual to use a high concentration of thulium and a low concentration of holmium [52]. This allows the greatest pump absorption by the thulium and then energy transfer from a large population to a small one ensures that the maximum amount of holmium is excited to the upper laser level. However, a low holmium concentration, while minimising threshold, makes the laser susceptible to simultaneous laser action from both the holmium and thulium [57]. In addition, these double-doped materials suffer from greater heat load (compared to singly-doped crystals) due to upconversion losses and the reversible energy transfer between the holmium and thulium [12, 25]; due to this, such systems are often operated at sub-zero temperatures: −40 °C in [51], −15 °C in [57] and cooled with liquid nitrogen in [58].

Holmium was not used in this work due to the extra complexity of pumping with a thulium laser and the problems described above with co-doped media.

### 1.3.2 Quasi-three-level laser material properties

Both thulium and holmium are quasi-three-level laser materials. This means that there is a thermally-dependent population in the lower laser level as the lower laser level is close to the ground state [21] (in both thulium and holmium, the lower laser level is a high-lying Stark level of the ground-level manifold [25]). Therefore, it is necessary to pump a quasi-three-level material harder than a four-level (such as neodymium emitting at 1064 nm) to overcome the thermal population and create a population inversion at room temperature [21]. This can be described as the medium having an effective inversion reduction factor (reduction in population inversion upon emission of a laser photon) greater than 1 [59]; the upper laser level population is reduced by 1 and the lower laser level is increased by the Boltzmann occupation factor because of the thermal population of this level. This population in the lower laser level acts as a saturable loss which decreases as the intensity in the cavity increases [60], this is due to the increasing intensity saturating the reabsorption. To overcome this, the pump is often double-passed through the crystal [5, 49]. Multi-pass pumping (as an extension and generalisation of double-pass pumping) has been shown to reduce reabsorption losses in high-energy Yb-based nanosecond laser amplifiers [61].

A general feature of quasi-three-level lasers is that the emission wavelength depends on the population inversion and hence the level of loss in the cavity; therefore, the output wavelength can be tuned to some extent by changing the output coupler transmission [41]. Also, a quasi-three-level laser's performance strongly depends on temperature and will show significant re-absorption of the laser wavelength due to the population in the lower laser level [3].

Despite the issues presented here, the quasi-three-level materials thulium and holmium are used for 2 µm lasers because they are the only options available. It is possible to use a frequency down-converted 1 µm laser, but this needs a non-linear conversion step that adds complexity and reduces efficiency. Starting from 1 µm becomes a less attractive option if the application calls for non-linear conversion of the 2 µm light to the 3 µm – 12 µm range due to efficiency concerns [20].

Having discussed 2 µm laser materials and settled on the use of Tm:YAP, the next point to discuss is the generation of high-energy pulses from thulium-based lasers.

## 1.4 Introduction to Q-switching

There are three main methods of producing a pulsed laser: mode-locking, gain switching and Q-switching. Mode-locking is a technique that, using careful control of the laser modes, can produce so-called ultra-short pulses with durations in the fs regime [21].

Such pulses can have high peak powers (for example, the $\mathrm{M}^2$ Laser Sprite system outputs pulses shorter than 150 fs at a repetition rate of 80 MHz with an average power $> 0.7\,\mathrm{W}$ across its tuning range which corresponds to peak powers $> 58\,\mathrm{kW}$ [21]) but with low pulse energies due to the high repetition rate (approximating the pulse as a triangle, the pulse energy of the Sprite is around 4 nJ) [16]. Gain switching uses a short, high-intensity pump pulse to produce pulses with durations of the order 10 ns – 100 ns [16]. In gain switching, the peak power and pulse width of the pump pulse and laser output are similar [21]. Q-switching uses control of the cavity losses to produce pulses with durations in the ps – µs regime with both high peak power and pulse energy by using the population inversion to store energy and then rapidly releasing it. These pulse properties make Q-switched lasers suitable for the applications discussed in section 1.3. The technique will be discussed in detail below.

Q-switching is a well-established technique (see for example references [16, 21, 62]) used to produce high-peak-power pulses of laser light. The general method can be imagined as having a shutter in the cavity; with the shutter closed to prevent oscillation, the gain medium is pumped to store energy in a large population inversion (many times larger than that in a CW laser). When the shutter is opened, a pulse builds up from noise and rapidly depletes the large population inversion. The pulse therefore has high energy and a duration in the ps – µs range, hence the interest in the technique. In practice, the shutter is implemented by controlling the cavity losses (or cavity Q) using one of the methods that will be discussed in section 1.4.1. A high-loss (or low Q) state corresponds to the shutter being closed and low loss (or high Q) is equivalent to having the shutter open.

The general method is shown schematically in figure 1.4. The laser starts with the shutter closed (high losses) while energy is stored in the population inversion. Some time later, the shutter is opened (fast transition to low losses) and a pulse is produced, sweeping out the gain stored in the population inversion as it builds. The pulse reaches its peak when the population inversion is at the CW threshold value. After this point, the pulse decays over a timescale defined by the cavity lifetime (which is dependent on the losses and cavity length).

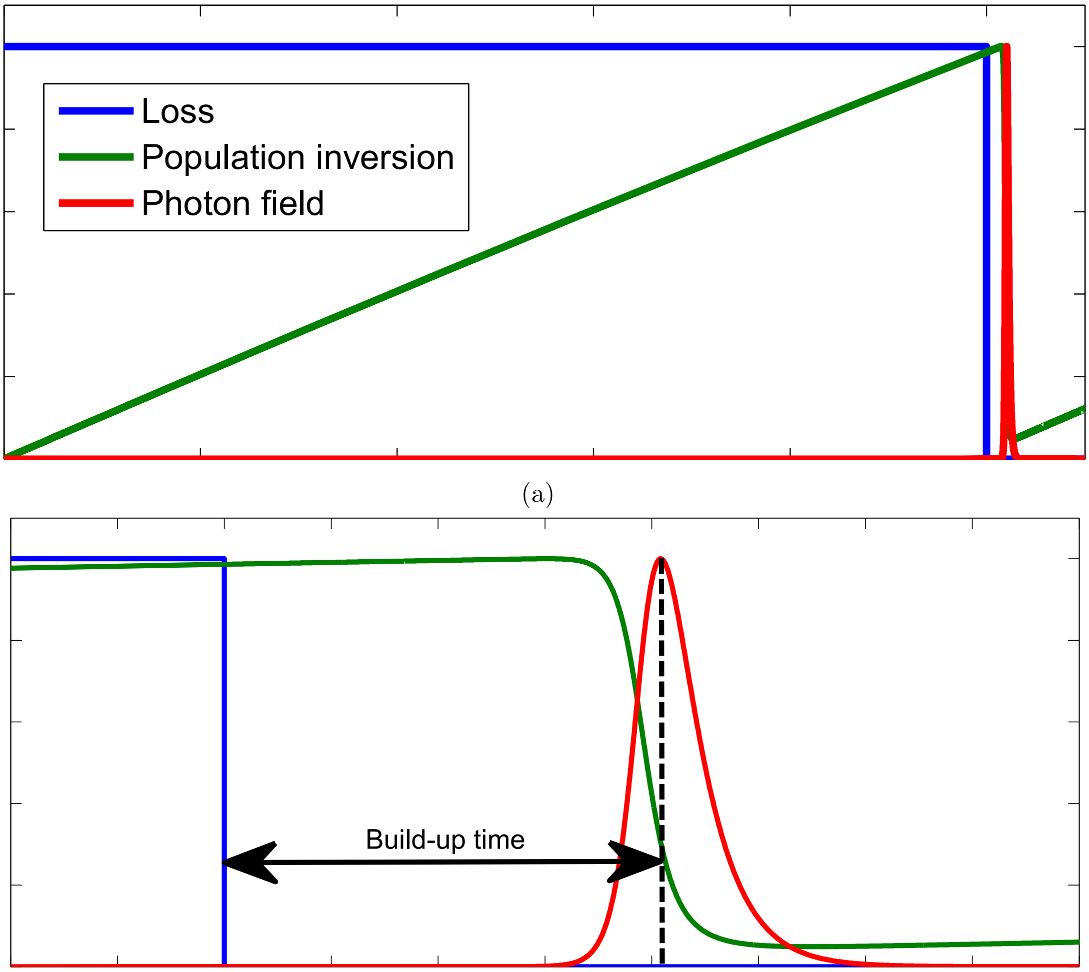

(a)

(b)

Figure 1.4: (a) Schematic showing the evolution of the population inversion and intracavity field with time during the Q-switching process. (b) A zoomed view on the pulse with the build-up time marked. Colours are kept the same in each figure.

This section will introduce the most common methods of Q-switching before looking at the rate equations describing the process and deriving some useful expressions from them. An extension of Q-switching called Q-switched cavity dumping will be discussed and finally the concept of jitter will be introduced.

### 1.4.1 Methods of Q-switching

The main methods of Q-switching involve using a rotating mirror, electro- or acousto-optic modulator or a saturable absorber to control the cavity losses. These are shown in figure 1.5 and explained below. Q-switching methods are classified as active or passive depending on whether an external trigger is needed to switch the system. The rotating mirror, electro-optic and acousto-optic Q-switches are active devices while the saturable absorber is a passive technique.

In considering these methods, two important properties are the speed of the switch and its hold-off ratio. The switch must be capable of opening fast enough that the low-loss state is reached before the pulse has appreciably built up, ie. the switching time must be shorter than the build-up time (which is typically tens to hundreds of nanoseconds) [16]. Failure to fully open the switch in this time frame can lead to multiple pulses being emitted [16], limiting the peak power and energy of each pulse. The hold-off ratio is a measure of how much loss is presented when in the high-loss state compared to the low-loss. A high hold-off ratio is desirable to prevent laser oscillation in the high-loss state.

#### 1.4.1.1 Rotating mirror/prism

In the rotating mirror method (figure 1.5a), one of the cavity mirrors is mounted on a rapidly spinning motor shaft. Due to this, the laser can only oscillate during the brief periods when the mirrors are aligned [16, 62]. This has the advantages of being cheap and simple to implement but suffers from uncertain timing, a slow switching speed and mechanical noise which leads to alignment difficulties [62].

To simplify the alignment of such a system, a 90° roof-top prism can be used in place of the mirror [16]. Such a prism ensures alignment in the plane perpendicular

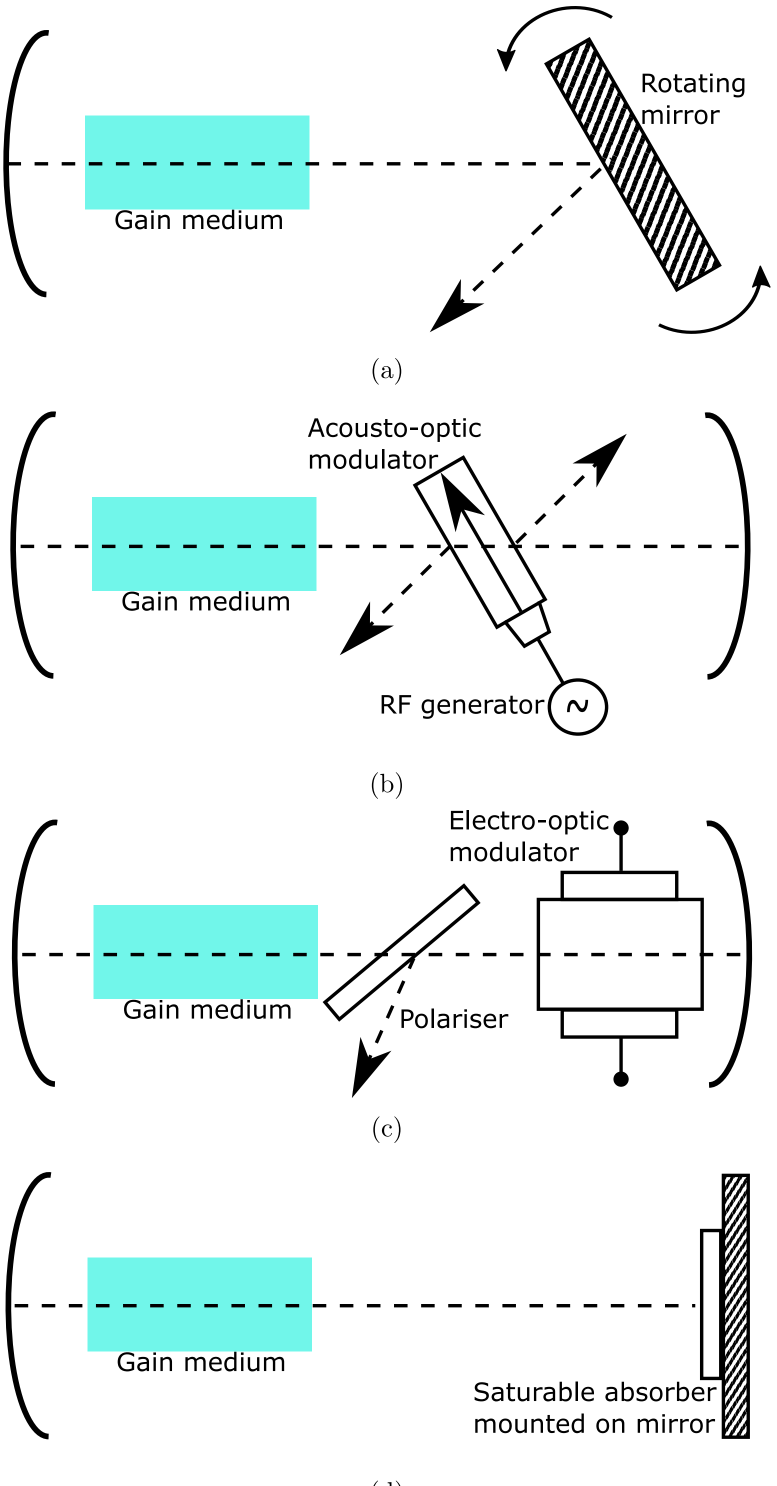

(a)

(b)

(c)

(d)

Figure 1.5: The four main methods of Q-switching: (a) rotating mirror, (b) acousto-optic, (c) electro-optic and (d) saturable absorber.

to the rotation [16]. Rotating prism Q-switches have the same pros and cons as the rotating mirror - cheap and simple but noisy and slow [16]. Due to these disadvantages, this method will not be considered further for this work although it is still used in some commercial systems.

#### 1.4.1.2 Acousto-optic

An acousto-optic modulator consists of a block of transparent optical material in which an ultrasonic wave is launched by a radio-frequency oscillator driven transducer [16]. The modulator is designed to prevent the acoustic wave forming a standing wave pattern in the medium by suppressing reflections [16]. The strain induced by the ultrasonic wave changes the local refractive index of the material, creating a grating in the medium that acts to diffract a fraction of any incident light out of the cavity [16, 62], as shown schematically in figure 1.5b. This additional loss prevents the laser from oscillating; the cavity can be returned to a high Q state by switching the transducer voltage off [16].

Advantages of acousto-optic Q-switching include its ease of use, simple radio-frequency circuitry [62] and low optical insertion losses [16]. However, acousto-optic Q-switches suffer from slow opening times and low hold-off ratios [16, 62]. The turn-off time of an acousto-optic Q-switch is determined by the transit time of the acoustic wave across the beam diameter; assuming a beam diameter of 1 mm, the transit time is around 200 ns for a typical device made of fused quartz [21]. The loss presented in the high-loss state (and therefore the hold-off ratio) is determined by the diffraction efficiency of the device and the applied RF power [21]; commercial devices are available quoting loss modulations $> 45\%$ (Gooch & Housego).

#### 1.4.1.3 Electro-optic

The electro-optical Q-switching method makes use of a cell exploiting an electro-optical effect, usually the Pockels effect. A Pockels cell consists of a suitable non-linear crystal in which an applied voltage induces a birefringence in the crystal [16]; this causes orthogonal polarisation components of an incident beam to travel at different speeds through the crystal, thereby rotating the polarisation state of the beam [21]. The full

Q-switch consists of electro-optic cell and a polarising element [62] (as shown in figure 1.5c), the components are oriented such that the birefringence axes of the Pockels cell are at 45° to the polarising element's transmission axis [16].

To illustrate the use of a Pockels cell and polariser as a Q-switch, consider a laser beam propagating in the cavity with a polarisation parallel to the polariser axis. This beam will be transmitted by the polariser and will then encounter the Pockels cell. If a voltage is applied to the Pockels cell such that it acts as a quarter-wave plate, the beam will be circularly polarised after one pass through the cell then reflect off the mirror and pass through the cell again, undergoing a 90° rotation in the round trip. Therefore, the beam will now be reflected out of the cavity by the polariser; this forms the high loss state. The Q-switch is then opened by removing the voltage on the Pockels cell, removing the voltage-induced birefringence and transmitting the beam without changing its polarisation. This logic can be inverted by adding a quarter-wave plate to the cavity between the polariser and mirror, adding an additional 90° rotation on a round-trip. Switching the logic in this way does not affect the characteristics of the switch but may make the system safer as the laser is held-off if the voltage fails in this case, although the extra optical element will introduce more losses to the cavity. In order to act as a Q-switch, the Pockels cell must be supplied with a high voltage (usually a few kV) that can be switched on or off in a time shorter than the rise time of the pulse (typically around 20 ns) [16].

Advantages of electro-optical Q-switching include its speed, precise timing, good stability and large hold-off ratio (due to the polarising element's discrimination between polarisation states - the polariser used in this work is coated to reflect $> 99\%$ of the S polarisation and is used at Brewster's angle for maximum transmission of the P polarisation) [62]. Disadvantages include the cost of the crystal and voltage source as well as the increased losses from adding extra elements to the cavity and the potential for damage to such elements [62]. Assuming typical anti-reflection coatings of $R < 0.1\%$ on the Pockels cell and a coated thin-film polariser at Brewster's angle, the Q-switch could be expected to introduce round-trip losses around 2 % to the cavity. It should also be noted that there is an additional disadvantage when using this method with an isotropic gain medium; under high-power pumping, the laser will suffer from depolarisation losses due to thermally-induced birefringence changing the polarisation state of the beam, a component of which is then rejected by the polariser [21].

#### 1.4.1.4 Saturable absorber

A saturable absorber consists of a material that absorbs at the laser wavelength and has a low saturation intensity [16]. The absorber is generally placed directly in front of the output coupler (as shown in figure 1.5d) or at a focus in the cavity. Laser action starts when the gain of the active medium exceeds the loss of the saturable absorber plus the unsaturable cavity losses [16]. As the intra-cavity intensity increases, the absorber begins to bleach which lowers the losses and allows a Q-switched pulse to develop [16].

It is important to note that the build-up time (the time taken for the pulse to reach its peak value from when the absorber begins to saturate, as shown in figure 1.4) is very long when using this method. Typical build-up times are several µs (or many hundreds of round-trips [63]) for this method and of the order of 100 ns (corresponding to tens of round-tips [63]) for the active techniques discussed above [21]. This is due to the gain barely exceeding the high threshold set by the absorber during the build-up phase [16]. Therefore, a large number of round trips are required for the pulse to attain its maximum intensity which results in a natural selection of cavity modes due to gain competition that makes single-frequency operation easier to achieve [16, 63].

The advantages of using a saturable absorber as a Q-switch are its simplicity, the lack of external drive circuitry and minimal intra-cavity elements (all due to the inherent internal triggering of this method) [62]. However, there is no pulse-on-demand capability and some of the pulse parameters (eg. repetition rate) are strongly dependent on the pump power [64]. There are problems with timing jitter and shot-to-shot amplitude fluctuations [62]. As a stable output is desirable for many applications, this method will not be explored further.

The electro-optical Q-switching method was chosen for this work due to its high hold-off ratio and speed. It also fits very well with the naturally polarised output of Tm:YAP as detailed in section 1.3.1.1 (meaning there will be no depolarisation losses).

Having chosen both a gain medium and a Q-switching method, the rate equation model that describes the Q-switched laser system will be discussed.

### 1.4.2 Rate equations

This section will introduce the rate equations describing active Q-switching for a quasi-three-level laser. Equations 1.1 are from reference [16] and describe the evolution of the population inversion density, $N(t)$, and photon number, $n(t)$, with time. $R_\mathrm{p}$ is the pump rate density, $f = \sigma_\mathrm{a}/\sigma_\mathrm{e}$ is the ratio of the effective re-absorption and stimulated emission cross-sections, $\sigma_\mathrm{a}$ and $\sigma_\mathrm{e}$ respectively. It should be noted that $\sigma_\mathrm{a}$, $\sigma_\mathrm{e}$ (and therefore $f$) and $N(t)$ are temperature dependent. The effective cross-section is the product of the cross-section of individual transitions and the fraction of electrons in each level of the upper manifolds (described by the Boltzmann distribution). $N_\mathrm{t}$ is the total active ion density and $\tau$ is the upper laser level lifetime. $V$ is the laser mode volume in the cavity and $V_\mathrm{a}$ is the mode volume in the gain medium. $\tau_\mathrm{c} = L/c\gamma$ is the cavity lifetime where $L$ is the optical length of the cavity, $\gamma$ is the logarithmic loss per pass and $c$ is the speed of light in vacuum. It should be noted that, in order to describe a quasi-three-level medium, the population inversion density is given by $N = N_2 - fN_1$ where $N_2$ ($N_1$) is the population density of the upper (lower) laser manifold. This reflects the fact that the emission of a photon reduces the population inversion by more than 1 as $N_2$ is reduced by 1 and $N_1$ is increased by 1 [16].

$$\frac{\mathrm{d}N(t)}{\mathrm{d}t} = R_\mathrm{p}(1+f) - \frac{fN_\mathrm{t} + N(t)}{\tau} - \frac{(\sigma_\mathrm{e}+\sigma_\mathrm{a})c}{V}N(t)n(t) \tag{1.1a}$$

$$\frac{\mathrm{d}n(t)}{\mathrm{d}t} = \left[\frac{\sigma_\mathrm{e}c}{V}V_\mathrm{a}N(t) - \frac{1}{\tau_\mathrm{c}}\right]n(t) \tag{1.1b}$$

It is possible to derive approximate equations for the build-up time $\tau_\mathrm{b}$, peak power $P_\mathrm{p}$, pulse energy $E_\mathrm{p}$ and pulse duration $\tau_\mathrm{p}$ from equations 1.1 (following the derivation used in [16] for a four-level laser). The build-up time is defined to be the time from the losses being switched to the peak of the pulse, as shown in figure 1.4. These equations (1.2 – 1.5) are given below. $N_\mathrm{i}/N_\mathrm{p}$ is the over-pumping ratio (a measure of how far above threshold the laser is), $N_\mathrm{i}$ is the population inversion density before the pulse and $N_\mathrm{p}$ is the value at the peak of pulse (which is equivalent to the CW threshold value). Reference [16] also defines the over-pumping ratio as the ratio of pump energy at the utilised pump rate (ie. the pump power) to the pump energy required for threshold operation, it will be explained in section 1.4.4.1 that there are issues with this definition. $\gamma_2$ is the logarithmic loss due to the output coupler, $A_\mathrm{b}$ is the mode area and $\eta_\mathrm{E}$ is the energy utilisation factor which is a measure of how much of the energy stored in the population inversion has been extracted by the pulse. Equations 1.2 – 1.5 differ from their equivalents for a four-level system by the $\frac{1}{1+f}$ factor that acts to reduce the build-up time, peak power and pulse energy for the quasi-three-level system.

$$\tau_\mathrm{b} = \frac{\tau_\mathrm{c}}{N_\mathrm{i}/N_\mathrm{p} - 1} \ln\left[\frac{V_\mathrm{a} N_\mathrm{p}}{1+f}\left(\frac{N_\mathrm{i}}{N_\mathrm{p}} - \ln\left(\frac{N_\mathrm{i}}{N_\mathrm{p}}\right) - 1\right)\right] \tag{1.2}$$

$$P_\mathrm{p} = \frac{\gamma_2}{2}\frac{h\nu}{\tau_\mathrm{c}}\frac{A_\mathrm{b}}{\sigma_\mathrm{e}}\frac{1}{1+f}\left(\frac{N_\mathrm{i}}{N_\mathrm{p}} - \ln\left(\frac{N_\mathrm{i}}{N_\mathrm{p}}\right) - 1\right) \tag{1.3}$$

$$E_\mathrm{p} = \frac{\gamma_2}{2}\frac{A_\mathrm{b}}{\sigma_\mathrm{e}}\frac{h\nu}{1+f}\eta_\mathrm{E}\frac{N_\mathrm{i}}{N_\mathrm{p}} \tag{1.4}$$

$$\tau_\mathrm{p} = \frac{E_\mathrm{p}}{P_\mathrm{p}} = \tau_\mathrm{c}\frac{(N_\mathrm{i}/N_\mathrm{p})\eta_\mathrm{E}}{(N_\mathrm{i}/N_\mathrm{p}) - \ln(N_\mathrm{i}/N_\mathrm{p}) - 1} \tag{1.5}$$

During the derivation of equations 1.2 – 1.5, it was assumed that changes in population inversion due to spontaneous emission and the pumping process can be neglected during the pulse build-up and that the switching is instantaneous. The first of these assumptions is justified as the population inversion (in the absence of stimulated emission) changes with a characteristic timescale of the upper state lifetime (4.4 ms in Tm:YAP, see section 1.3.1.1) while the pulse build-up time is typically in the 100 ns – µs range (see section 2.4). The second is also called the fast switching case and holds as long as the population inversion does not significantly change during the switch [65]; this is justified for electro-optic Q-switching as the switch can be opened within a few ns which is fast compared to the build-up time.

### 1.4.3 Cavity dumping

An extension of the traditional Q-switching technique that is particularly suited to generating short pulses is Q-switched cavity dumping [21]. In this technique, energy is stored in the intra-cavity field rather than in the population inversion (as it is in Q-switching). Therefore, an HR cavity is used to contain the intra-cavity field and the Q-switching element effectively acts as a variable output coupler. To start, the method is the same as for standard Q-switching; the cavity is held in a high loss state while the pumping process creates a large population inversion. Next, the laser is switched to low loss and the intra-cavity field builds up from noise but is held inside the HR cavity. Finally, the losses are switched back to high and the entire field is coupled out of the cavity within a few round trips. This process is shown schematically in figure 1.6. To illustrate the difference in pulse durations produced using Q-switching and cavity-dumping, the laser built for this work and described in section 2.1 produced pulses with durations $\sim 40\,\mathrm{ns}$ when Q-switched and $\sim 2\,\mathrm{ns}$ when cavity dumped.

In the case of implementing this technique with an electro-optic Q-switch (comprising a Pockels cell and polariser, see section 1.4.1), a voltage is applied to the Pockels cell to prevent laser oscillation while energy is pumped into the gain medium. The applied voltage causes the Pockels cell to rotate the polarisation such that any beam is rejected by the polariser. When the voltage is removed, laser action begins from noise until a pulse is formed but is kept in the cavity. At the peak of the pulse, the voltage is re-applied to the Pockels cell causing the entire intra-cavity field to be ejected from the cavity by the polariser within a few round-trips (dependent on polariser discrimination).

As can be seen in equation 1.5, the Q-switched pulse duration strongly depends on the initial population inversion and the threshold value. Using the cavity dumping technique, the pulse duration is decoupled from the gain dynamics and depends only on the round trip time of the cavity and the opening time of the Q-switch [66]. This is what makes it a useful method of producing short pulses in low gain systems (such as thulium) as the pulse duration will be independent of the gain. There are two downsides to this technique; first, the second switch must be very fast ($\sim$ few ns) as it sets the pulse duration. Secondly, the timing of the cavity dump is critical; if it is triggered too late, the pulse remains trapped in the cavity and its high intensity can damage optics.

### 1.4.4 Jitter

Having introduced methods of pulse generation, the characteristics of these pulses (particularly jitter) will be discussed. While jitter is a well-known phenomenon, and is present to some degree in all Q-switched lasers, it is not extensively discussed in the literature. Therefore, it shall be defined and explained here and the few solutions presented previously will be discussed.

#### 1.4.4.1 Definition

In many papers on Q-switching, a pulse train is shown such as that in figure 1.7a. It can be clearly seen that there are fluctuations in the peak power of the pulses in the train. However, these variations are not often analysed or explained (reference [67] is one of the exceptions where the amplitude stability is measured). Similar variations were seen in Q-switched and cavity-dumped thulium lasers built at Fraunhofer CAP. Subsequent investigations (see chapter 2) have revealed that there are pulse-to-pulse fluctuations in build-up time, pulse duration, peak power and pulse energy (as shown in figure 1.7b) which will now be termed jitter in those pulse parameters. Prior to the commencement of this work, no investigations in to the causes or methods of analysing the jitter in all pulse parameters of Q-switched lasers have appeared in the literature to the best of the author's knowledge.

However, it is worth mentioning the analysis [68] by Martin *et al.* on pulse timing jitter in a single-frequency Nd:YAG laser Q-switched using an acousto-optic modulator and the pre-lase technique (see section 1.4.4.2). It is also worth noting that the authors state that they "are aware of no comparable work that combines experiments with detailed numerical simulations of the Q-switching process with classical noise" [68], demonstrating the paucity of literature on jitter. The method used in [68] centred on recording 5000 consecutive pulses and comparing the build-up times (called the peak time in the paper). This is similar to the characterisation techniques applied in this thesis, which were conceived and implemented independently, prior to the publication

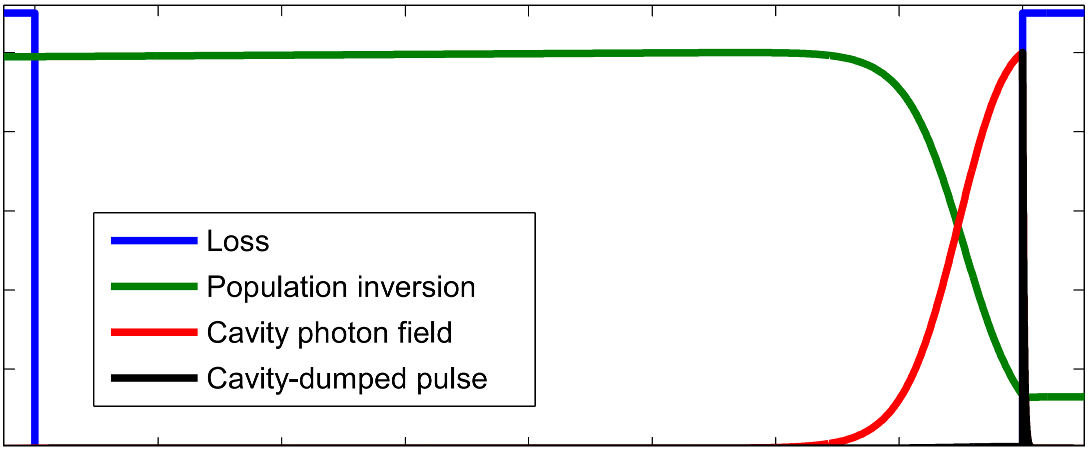

(a)

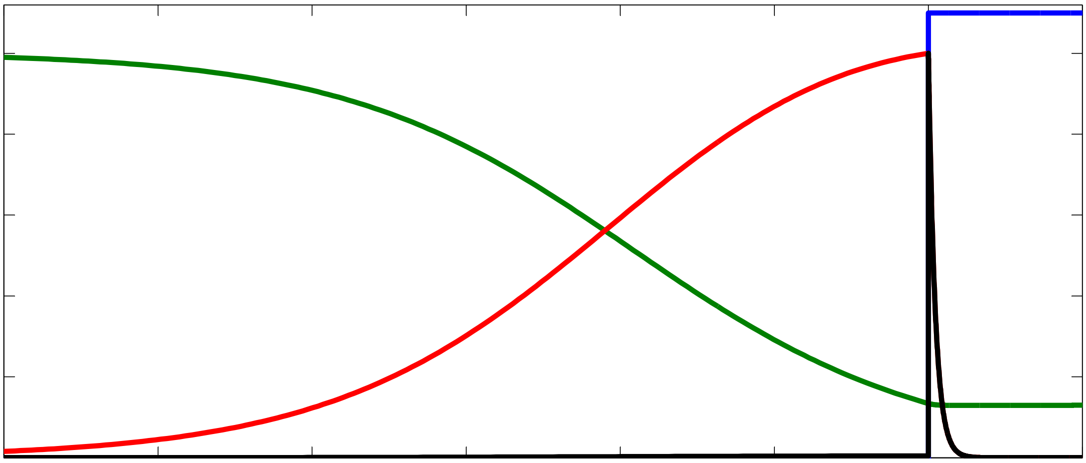

(b)

Figure 1.6: (a) Schematic showing the evolution of the cavity losses, population inversion, intra-cavity field and laser output during the Q-switched cavity dumping process. The pump period before the first switch has been omitted. (b) A zoomed view on the cavity-dumped pulse. Colours are kept the same in each figure.

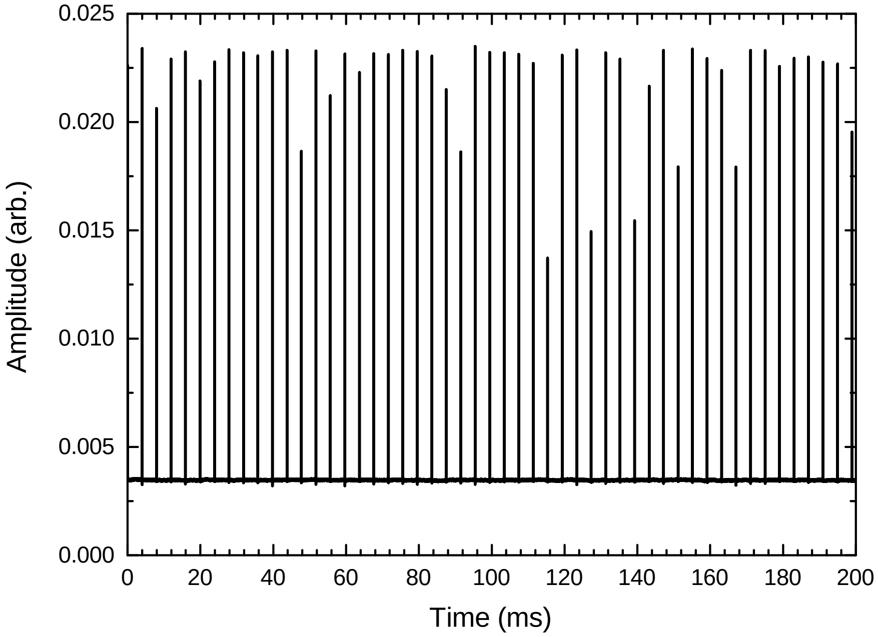

(a)

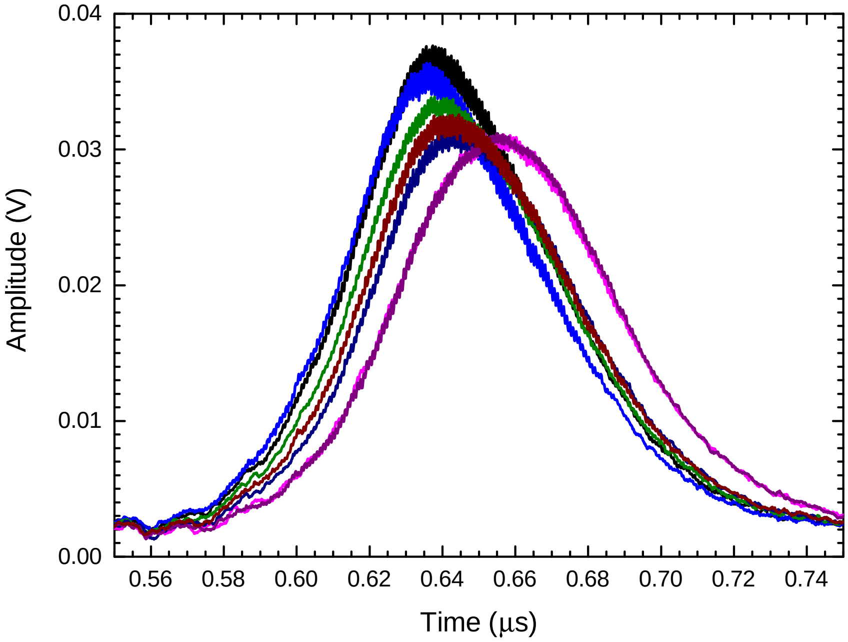

(b)

Figure 1.7: (a) Pulse train from the Tm:YAP laser similar to those shown in the literature showing peak power jitter. (b) Smoothed pulses showing build-up time jitter in pulses of around 20 ns (smoothing necessary to remove mode beating for visibility).

of [68]. In their analysis, evidence was found of both stochastic and oscillatory effects on the jitter; an FFT showed the oscillatory component was at 105 Hz. A numerical model was able to reproduce the main features of the jitter and it is postulated that the periodic perturbations are due to mechanical or electrical resonances in the system.

The analysis in [68] is, to the author's knowledge, the only jitter investigation undertaken on an actively Q-switched laser. The jitter in passively Q-switched lasers has been investigated more frequently; again, however, not in the detail undertaken in this work. Qiao *et al.* [69] and Lin *et al.* [70] briefly look into the amplitude jitter of their Tm:LuAG and Nd:YAG lasers (respectively) as part of the characterisation of new saturable absorber materials. In these works, the pulse train is recorded and the clock amplitude jitter (CAJ) is calculated according to equation 1.6 as in [71] where $\sigma$ is the standard deviation and $M$ is the mean value of the intensity. CAJ values of 2.1 % in the thulium laser [69] and 4.97 % in the Nd:YAG [70] were reported. Qiao *et al.* also recorded the average power over a 2 h period and found the variation to be about 10 mW on an average of 1.74 W, leading them to quote better than 1 % power stability over this period [69]. More often, jitter is only briefly mentioned; the work in reference [72] is an example where the pulse train is recorded and stabilities are claimed (in this case "low intensity instabilities ($< 10\,\%$) and rms pulse-to-pulse timing jitter ($< 7\,\%$)") with no detail on how these values are obtained.

$$\mathrm{CAJ} = \frac{\sigma}{M} \times 100\% \tag{1.6}$$

Jitter is problematic for applications that depend on accurate timing (for example, laser ranging where timing information is converted into position information [68] or pump-probe experiments requiring temporal overlap of pulses [73]) or requiring specific peak power or energy (such as nonlinear optics experiments, for example). Furthermore, any build-up time jitter in a Q-switched laser is translated into amplitude variations if that system is then cavity-dumped. This is due to the peak power of the cavity-dumped pulse being determined by the Q-switched pulse amplitude at the time of the dump; therefore if the Q-switched build-up time is varying, the peak will occur at a time other than the dump time and so a different (lower) peak power will be output for that cavity-dumped pulse. This specific problem is illustrated in figure 1.8, where it is clear that the pulses have different amplitudes as well as some time jitter (some of which could be due to jitter between the signal triggering the cavity dump and that triggering the initial Q-switch and oscilloscope). Stable cavity dumping would require the jitter in the Q-switched build-up time to be much less than the pulse duration; therefore, variations in the build-up time less than 1 ns is a good target. As the end goal would be to commercialise a stable Q-switched 2 µm laser, manufacturer specifications of jitter in similar neodymium systems will form the target levels of jitter for this work. Elforlight claim $< \pm 1$ ns jitter from an external trigger in their SPOT laser [74] and the Coherent HELIOS has $< \pm 2$ ns jitter between sequential pulses [75]. Quantel Laser advertise a high-energy Nd:YAG laser with a jitter of ±1 ns with respect to the Q-switch trigger for 99 % of 500 shots and ±2 % energy stability [76]. Continuum offer an Nd:YLF laser with time jitter $< 3$ ns RMS and energy stability of 0.5 % RMS (output energy 30 mJ – 60 mJ depending on model) [77]. Laser2000 offer various wavelengths around 1 µm with power stability of 3 % RMS (average power of 2 W) [78]. Based on these specifications, this work will aim to produce a Q-switched Tm:YAP laser with build-up time jitter $< 1$ ns and pulse energy stability $< 3$ % with the best possible stability in pulse duration and peak power.

During previous work conducted at Fraunhofer, it was qualitatively observed that the jitter in a Q-switched Tm:YAP laser was worse than would be typical for a similar Nd:$YVO_4$ laser. This is understood by the author to be due to the higher gain in the Nd laser and will be explained using equation 1.2 for the build-up time, although the reasoning also applies to the other pulse parameters. This equation is plotted for a range of over-pumping ratios in figure 1.9 using the parameter values detailed in table 1.2.

Using a high-gain laser medium, such as Nd:$YVO_4$, it is easy to attain high values of the over-pumping ratio due to the larger stimulated emission cross-section and lack of reabsorption losses. To illustrate this, a quick calculation of the value of the over-pumping ratio for an Nd:$YVO_4$ and Tm:YAP laser is presented. For each material, it is assumed that the pump power at the appropriate wavelength is 4 W (experiments

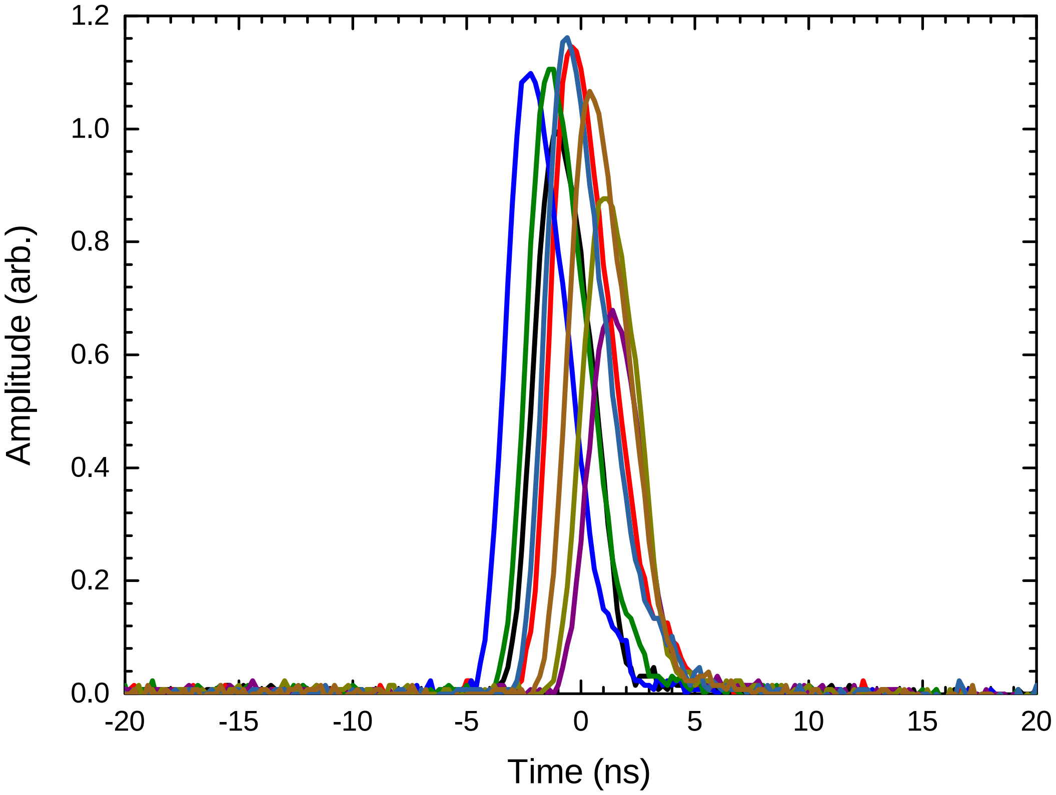

Figure 1.8: Example cavity-dumped pulses showing amplitude fluctuations.

conducted in later chapters are done with pump powers around this value) and the pumped volume is the same. It is further assumed that the pump phase in both cases has a duration equal to the fluorescence lifetime $\tau$. In order to find $N_\mathrm{i}$, equation 1.1a is solved at $t = \tau$ with $n(t) = 0$ (ie. before the Q-switch occurs) and is given in equation 1.7. Using the values given in table 1.2, over-pumping ratios of 9.1 and 67.2 are obtained for Tm:YAP and Nd:YVO$_4$ respectively. As can be seen in figure 1.9, the curves are considerably steeper in the region about 10 (where the Tm:YAP can be expected to operate) and so a small change in the over-pumping ratio will cause a large change in the pulse parameters which constitutes a large jitter. Changes in over-pumping ratio can be caused by variations in the pumping process and/or changes in the cavity loss (including mechanical vibrations and air currents). Therefore, efforts to reduce the jitter will focus on controlling the pump and losses.

$$N_\mathrm{i} = (R_\mathrm{p}\tau(1+f) - fN_\mathrm{t})(1-\mathrm{e}^{-1}) \tag{1.7}$$

It should be noted that the over-pumping ratio could not be experimentally defined as there is no way to measure the population inversion before the pulse ($N_\mathrm{i}$). In equation 1.7, it was assumed that the system started with no population inversion before the pump phase. In reality, a Q-switched pulse cannot sweep out all of the gain stored in the medium and so some population inversion will be left at the start of the pump phase. This starting population inversion becomes more important at higher repetition rates where there is less pumping time and so $N_\mathrm{i}$ could be very different for consecutive pulses. As such, CW threshold pump powers ($P_\mathrm{th}$) will be given in experimental chapters but the over-pumping ratio as defined by $\mathrm{OP} = N_\mathrm{i}/N_\mathrm{p} = P_\mathrm{pump}/P_\mathrm{th}$ will not be an accurate value.

An initial look into the jitter present in a Q-switched Tm:YAP laser produced the histogram of build-up times shown in figure 1.10. Pulses were recorded using a fast photodetector (EOT5000) and oscilloscope (Rohde & Schwarz RTO 1044) at a repetition rate of 250 Hz with an incident pump power of 3.7 W. The build-up time was extracted following the procedure detailed in chapter 2. It can be seen that the width of the distribution is around 40 ns; therefore, the jitter is too great for stable

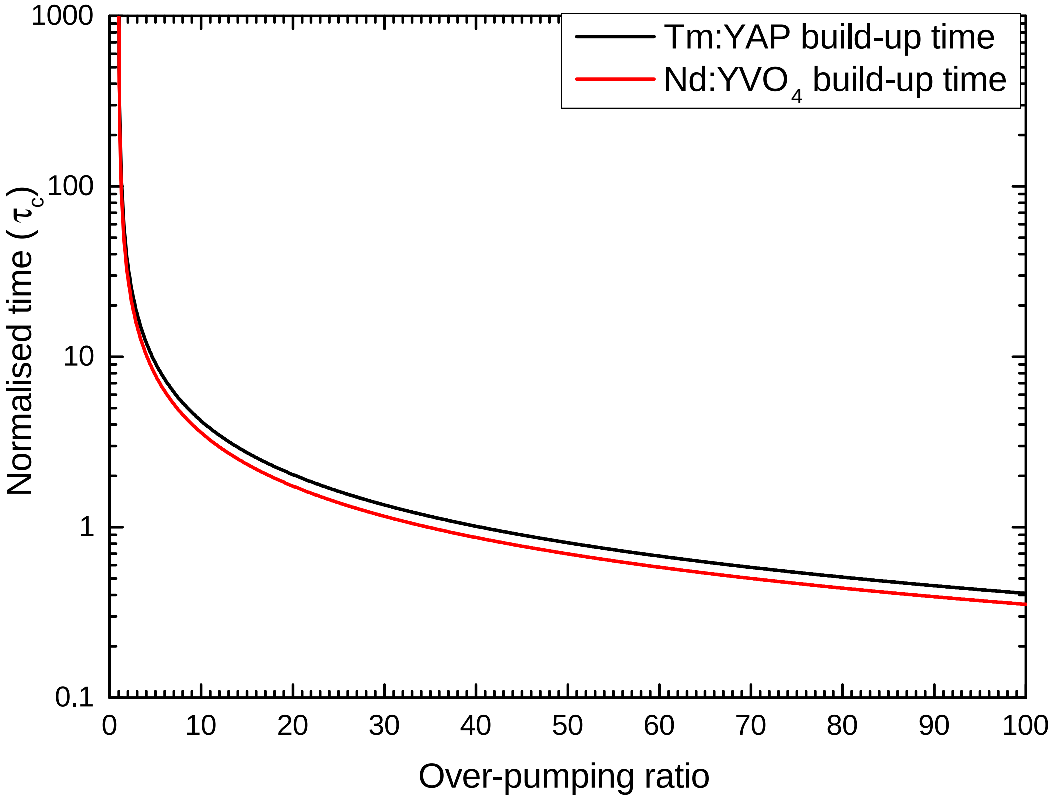

Figure 1.9: Dependence of the build-up time (in units of the cavity lifetime $\tau_c$) on the over-pumping ratio for Tm:YAP and Nd:YVO$_4$.

Table 1.2: Parameters used to generate figure 1.9. Unreferenced values are either calculated (equation given) or describe the modelled cavity.

| Parameter | $Nd:YVO_4$ [ref.] | Tm:YAP [ref.] |
|---|---|---|
| $\lambda_L$ (nm) | 1064 | 1940 |
| $\omega$ (µm) | 140 | 140 |
| $l$ (mm) | 3 | 3 |
| $V_a = \pi\omega^2 l$ ($10^{-10}$ m) | 1.85 | 1.85 |
| $\gamma$ | 0.0357 | 0.0357 |
| $\sigma_e(\lambda_L)$ ($cm^2$) | $1.44 \times 10^{-18}$ [79] | $5 \times 10^{-21}$ [33] |
| $\sigma_a(\lambda_L)$ ($cm^2$) | 0 | $0.486 \times 10^{-21}$ [33] |
| $N_p = \frac{\gamma}{\sigma_e l}$ ($m^{-3}$) | $8.26 \times 10^{22}$ | $2.38 \times 10^{25}$ |
| $f = \frac{\sigma_a}{\sigma_e}$ | 0 | 0.0972 |
| $\eta_E$ | 0.5 | 0.5 |
| $\tau$ (µs) | 100 [21] | 4400 [48] |
| $N_t$ @ 4 at.%Tm ($m^{-3}$) | – | $7.86 \times 10^{26}$ [38] |
| $\lambda_p$ (nm) | 808.5 [21] | 795 [4] |

cavity dumping. There is also some structure in the data which lead to the recording of the benchmark data set (detailed in chapter 2) to investigate this.

#### 1.4.4.2 Solutions in literature

Most mentions of jitter in the literature occur in discussions of passively Q-switched systems due to such lasers inherently suffering from uncertain timing (as stated in section 1.4.1). However, some papers have suggested methods of reducing this problem.

The first proposed solution is a hybrid Q-switching technique that uses both active and passive Q-switches [80–83]. This technique can produce pulses that are shorter and more symmetric than either acousto-optic or passive Q-switching [80]. Combining a passive Q-switch with an electro-optic modulator in a Nd:YAG laser, the authors of [81] quote that jitter in the pulse energy and pulse width could be reduced to ±3.65 % and ±2.58 % respectively (from ±5.25 % and ±4.55 % for pure electro-optic Q-switching and ±8.91 % and ±5.17 % for pure passive Q-switching). The combination of acousto-optic and passive Q-switch was shown to have a minimum build-up timing jitter of approx-

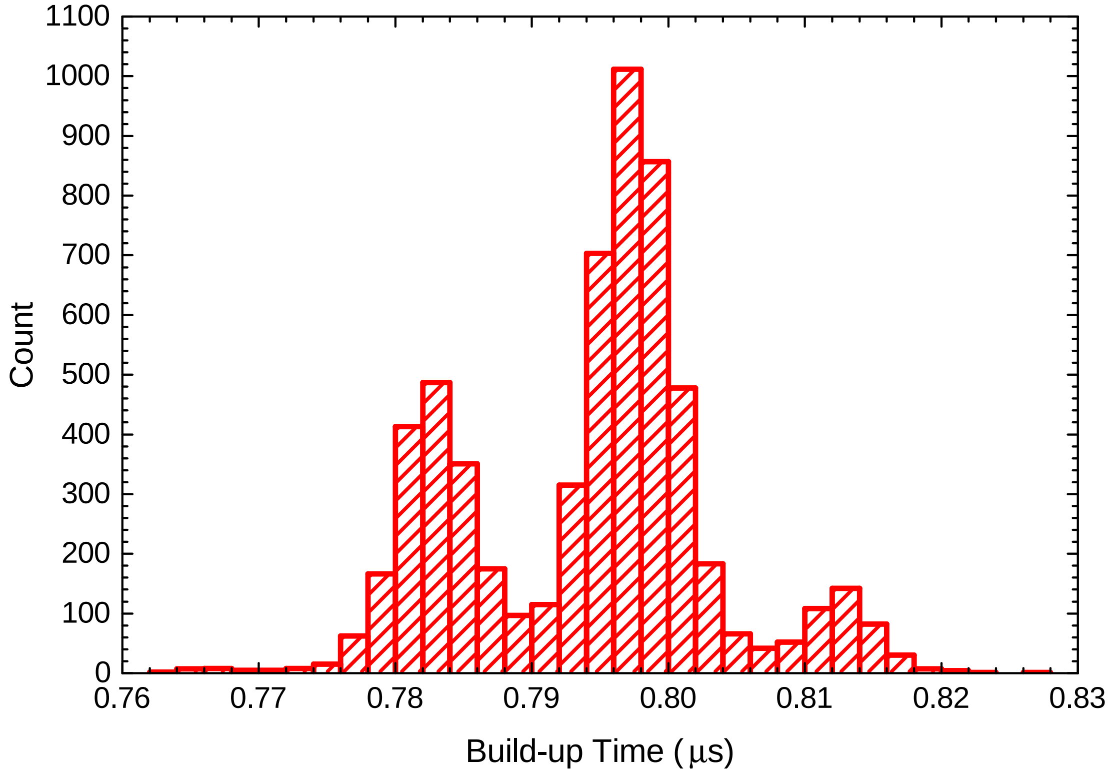

Figure 1.10: Histogram from early data taken at a repetition rate of 250 Hz and incident pump power of 3.7 W.

imately 400 ns which was a reduction of 162 times compared to the purely passively Q-switched system (although the pure acousto-optically Q-switched system showed a jitter of around 200 ns and the authors stress these are the minimum timing jitters but do not elaborate further) [83]. This dual-switch approach improves the jitter in passively Q-switched systems as the external trigger of the active switch determines the jitter rather than the statistical build-up of the passive Q-switch [83].

Another method of improving the jitter in a passively Q-switched laser is to optically trigger the Q-switch by bleaching the saturable absorber with a second laser [84]. This method showed a reduction in pulse-to-pulse timing jitter of around 12 times – from 241 ns for free-running to 20 ns with the optical triggering [84]. Both methods covered so far are for improving passively Q-switched systems and so are not applicable to the actively Q-switched Tm:YAP laser studied in this work.

Several publications have linked single-frequency operation to reduced jitter [85–87]; although this has, to the author's knowledge, only been examined in passively Q-switched systems, it should work similarly in an active system. The instability dynamics of a passively Q-switched Nd:YAG laser were investigated in reference [86] by observing the pulse trains under different pump powers, see figure 1.11. Stable oscillation was observed when the laser ran on a single mode; however, a modulation of the output intensity was seen when the laser was oscillating on two modes [86]. This was attributed to cross-saturation due to spatial hole burning coupling the modes together via competition for population inversion and the non-linear absorption of the saturable absorber [86]. As the gain competition is not specific to passive Q-switching, it is reasonable to deduce that single-frequency operation will reduce the jitter in an actively Q-switched laser in the same fashion.

Timing jitter and amplitude variation were reduced to better than ±1 % and ±0.6 % from around ±5 % and ±3 % respectively by operating a passively Q-switched microchip laser on a single longitudinal mode [87]. It has been shown that the instabilities seen in passively Q-switched two-mode microchip lasers (such as those in [86,87]) are due to longitudinal-mode competition [86]. Although the Tm:YAP laser investigated in this work does oscillate on more than two longitudinal modes when free-running, single-

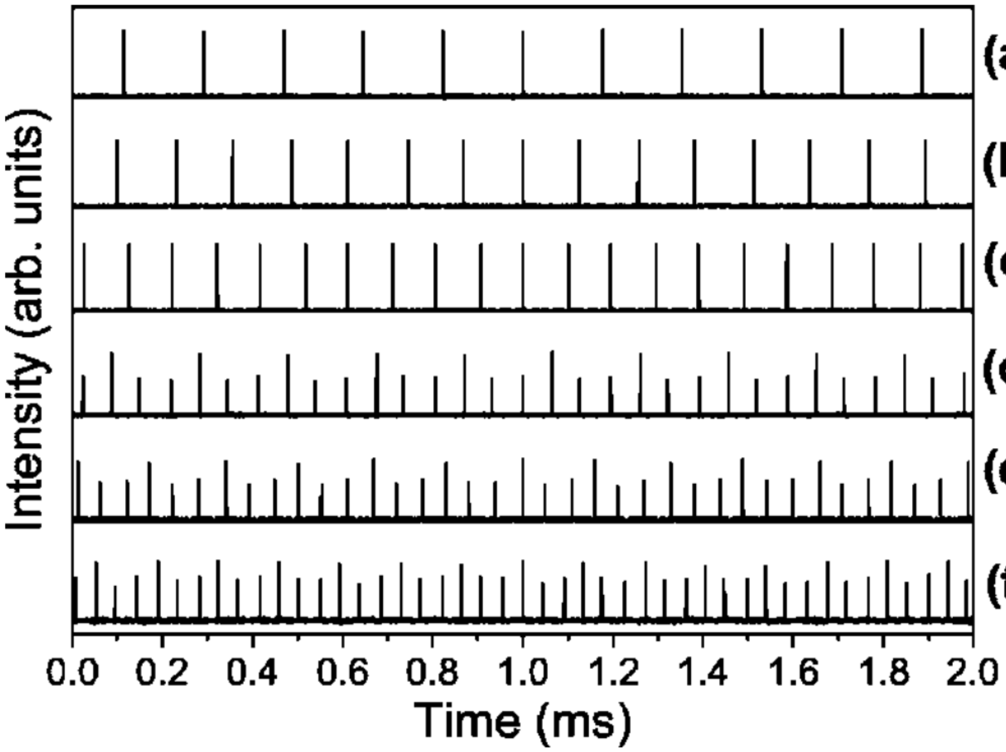

Figure 1.11: Pulse trains from a passively Q-switched Nd:YAG laser operating on a single-mode in (a)–(c) and two modes in (d)–(f). From [86].

frequency operation will be investigated as a means of reducing jitter (see chapters 3 and 5). Operating on a single longitudinal mode is expected to reduce the jitter in the laser by removing mode competition (reported to be the source of instabilities in [86]) and ensuring that each Q-switched pulse is at a reproducible wavelength [85], making all pulses more similar.

As a route to single-frequency operation, variations of injection seeding can be used to reduce the jitter in a laser [88, 89]. In reference [88], a fibre delay line is used to feed a small portion of a previously emitted pulse back in to the Nd:YVO$_4$ laser shortly before the build-up of the next pulse. Injection seeding may help reduce the jitter in a laser by forcing the same initial conditions on every pulse; controlling how each pulse starts should lead to them developing in the same way every time, thereby reducing jitter. This technique reduced the timing jitter to significantly below the pulse duration [88]. In reference [89], an actively stabilised pre-lase technique is used to self-seed the Nd:YAG laser to achieve single-frequency operation and reduced jitter. The pre-lase technique (see references [90–92]) is a modified Q-switching technique during which, using the shutter analogy again, the shutter is slightly opened after the usual pump phase. This allows a high-threshold build-up in a single longitudinal mode. After this mode has built to an empirically-defined pre-set level, the shutter is opened fully and the chosen mode acts as a seed and out-competes all others.

## 1.5 Summary

In summary, Tm:YAP has been chosen as the gain medium for this work due to its good thermal properties and relatively high stimulated emission cross-section. Electro-optic Q-switching was selected as the Q-switching method for the superior speed and hold-off offered by this technique compared to others as well as its compatibility with the naturally polarised output of Tm:YAP. Jitter has been introduced and demonstrated to be a problem. Specifically, a goal of reducing the build-up time jitter to below 1 ns has been proposed. Analysis of the effect of the over-pumping ratio on the pulse parameters implied that control of the pump and cavity losses will reduce jitter and single-frequency operation has been identified in the literature as another potential route to low jitter. However, it is expected that reducing the jitter in a thulium laser will be harder than in a neodymium laser due to the lower gain and reabsorption losses due to the quasi-three-level nature of thulium.

The next chapter describes the laser system built as well as the method for and results of recording a benchmark data set for characterising and investigating jitter.

# Chapter 2

# Benchmark Data Set

Having introduced jitter in the previous chapter, this section will begin to characterise it. The method detailed in section 2.3 was used in an initial investigation into the distribution of the build-up time from a different laser to that presented in section 2.1. The results are shown in the histogram in figure 1.10 and reproduced in figure 2.1a. The grouping of the build-up time values into three distinct clusters was unexpected and suggests that there may be a pattern in the jitter. Plotting the build-up time for each pulse as shown in figure 2.1b also hints at, perhaps, regions of stability that the laser likes to oscillate in. After this, the decision was made to take a comprehensive data set to see if such patterns could be understood more thoroughly.

This data set will also be valuable as a baseline for gauging the effectiveness of improvements made in subsequent chapters; as well as for the light that a detailed understanding of the characteristics of the jitter might throw on its origins. In order to do this, pulses were recorded for different pump powers, repetition rates and output couplers. These were then analysed to obtain the build-up time, pulse duration, peak power and pulse energy for each pulse. A statistical analysis was then performed on each distribution to obtain the standard deviation as a measure of the jitter in each parameter. It was concluded that the jitter becomes worse at higher repetition rates, and is generally too high for a commercially viable laser, and in particular too high for stable cavity dumping, for reasons that will be discussed further in this chapter.

This chapter will begin with a description of the laser built for this work before

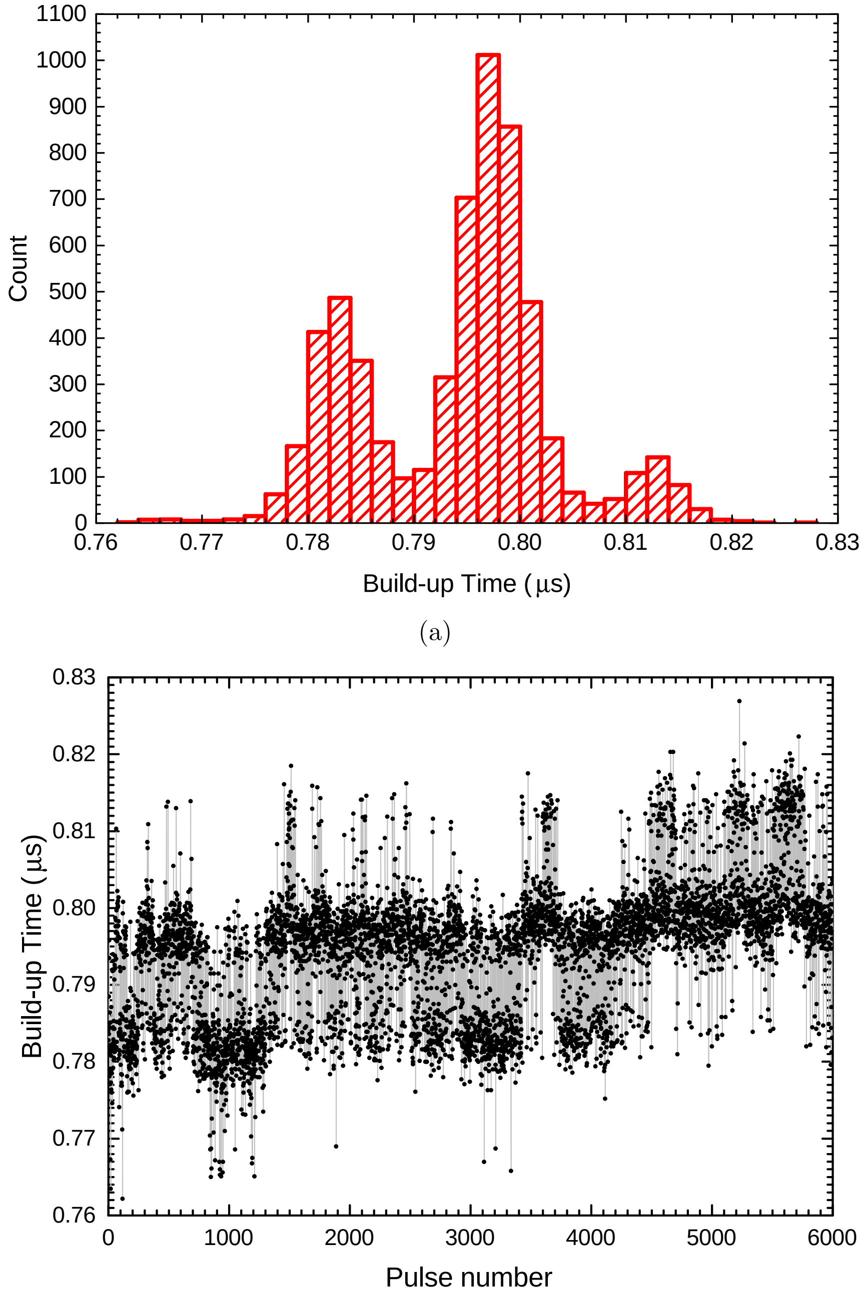

(a)

(b)

Figure 2.1: (a) Histogram from early data taken using a different laser to that presented in section 2.1, operating at a repetition rate of 250 Hz and incident pump power of 3.7 W, showing a distinct pattern in the distribution. (b) Plot of the build-up time values in (a) against pulse number, again highlighting a pattern in the distribution.

defining the aims and objectives of this experiment. Section 2.3 describes the method used to analyse the jitter in the laser in more detail. Section 2.4 presents the results of the experiment, section 2.5 details an investigation in to the pump stability as a cause of jitter and the conclusions drawn from these experiments are discussed in section 2.6.

## 2.1 The test laser

A diagram of the test laser created for this work is shown in figure 2.2a. The system can be split into two main parts: a pump section for shaping the pump beam and controlling the incident power and the laser cavity. The system will be described here, going from left to right in figure 2.2a and starting with the pump section.

The pump source used is a DILAS fibre-coupled 795 nm 25 W diode laser (model number M1F2S22-795.3-25C-SS2.1). The pump light is delivered to the breadboard by a 200 µm diameter core, 0.22 numerical aperture fibre. The beam is collimated by a 35 mm focal length lens and then enters a variable attenuator. The attenuator comprises two polarising beamsplitters and a half-wave plate as shown. Rotation of the half-wave plate allows the selection of a pump power while keeping the diode current and temperature (and hence wavelength and mode content) constant. The attenuated pump beam then passes through a 30:70 (R:T) non-polarising beamsplitter that allows monitoring of the unabsorbed pump before being focussed by a 50 mm focal length lens to a spot radius of ∼140 µm at the centre of the crystal (measured using the knife-edge technique). The use of the attenuator limited the maximum pump power usable during these experiments due to the first polariser immediately rejecting half of the unpolarised pump power, the non-polarising beamsplitter removing another 30 % and losses at surfaces further reducing the transmitted power. The maximum pump power through the attenuator setup was measured to be 7.5 W.

The crystal used was an *a*-cut ($P_{nma}$ notation) 4 at.% Tm:YAP from Scientific Materials with dimensions of 4 mm × 4 mm × 3 mm. The crystal is coated on one side to be HR at the laser wavelength ($T < 0.2\,\%$ @ 1940 nm and 1990 nm) and HT at the pump wavelength ($T > 99\,\%$ @ 793 nm – 795 nm), with the other side vice versa ($T > 99.4\,\%$ @ 1940 nm and 1990 nm and $T < 1.2\,\%$ @ 793 nm – 795 nm). This means

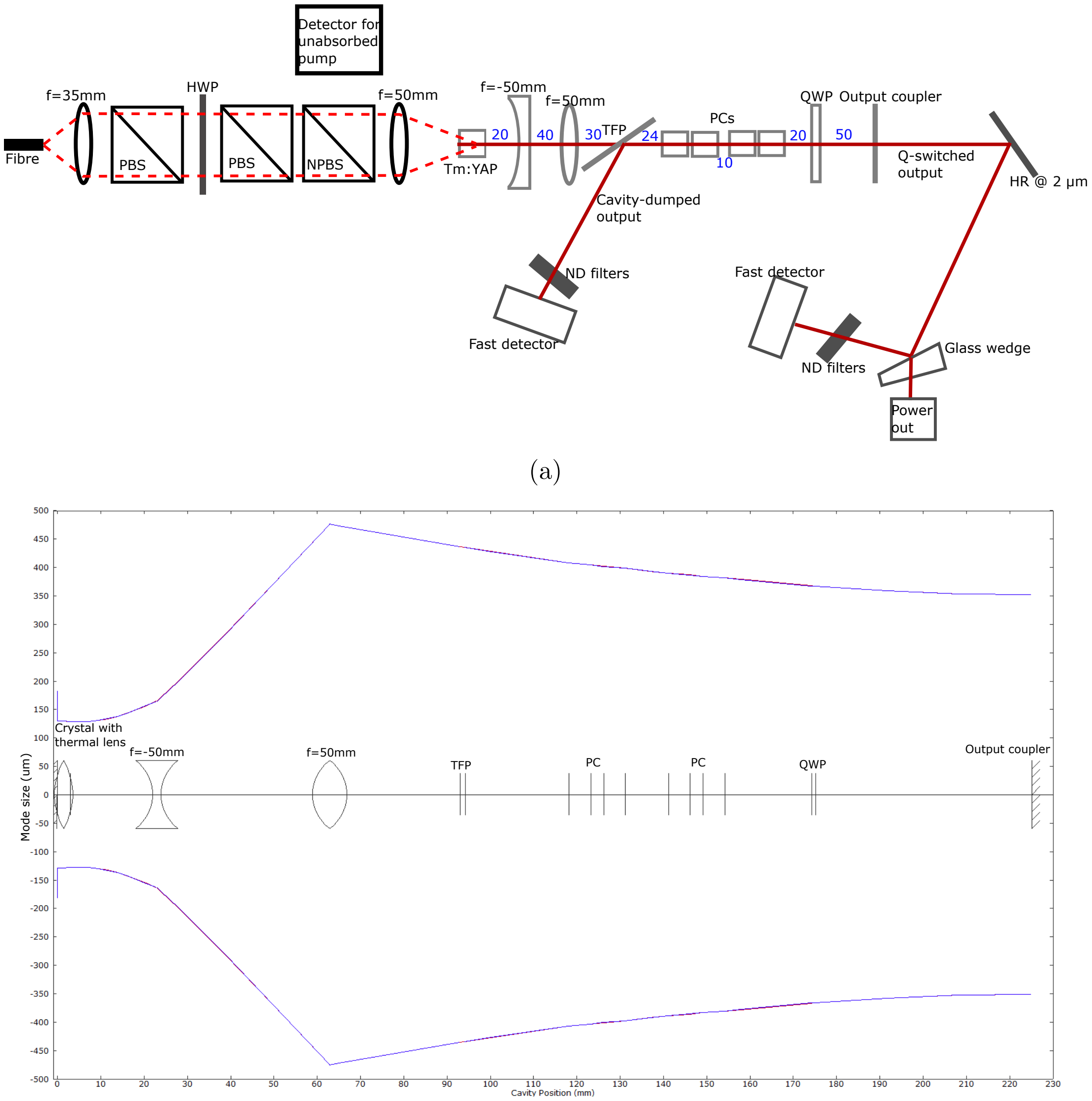

(a)

(b)

Figure 2.2: (a) Schematic of the test laser built for this work. PBS = polarising beamsplitter, NPBS = non-polarising beamsplitter, HWP = half-wave plate, TFP = thin-film polariser, PCs = Pockels cells, QWP = quarter-wave plate. The laser is built to be capable of Q-switching or cavity dumping; for the work described in this chapter, the laser was run Q-switched. Optic spacings in mm are shown in blue. There is a 3 mm gap between the crystals that make up each Pockels cell. (b) Mode spacing throughout the cavity when the simulated thermal lens has a focal length of 120 mm.

that the crystal face forms one end mirror in the cavity and the pump is double-passed, for the reasons discussed in section 1.3.2. The cavity has been designed (using a model in LaserCanvas – an interactive ABCD solver available from P. Schlup, Colorado State University, Fort Collins) so that the laser mode is $\sim 140\,\mu\text{m}$ in radius in the crystal to ensure good overlap with the pump. The LaserCanvas model includes a thermal lens with focal length variable across the range 1 mm – 1000 mm, figure 2.2b shows the mode spacing throughout the cavity for a simulated thermal lens focal length of 120 mm. Following the crystal are two infrasil lenses with focal lengths of $-50$ mm and 50 mm to make the cavity mode as collimated as possible in the next part of the cavity. The collimation is desirable in order to optimise wavefront matching and therefore get the best transmission and selectivity from the etalons that will be added to the cavity in chapter 3. The cavity sensitivity to the exact positions of these lenses is shown in figure 2.3 and was judged to be minimal. Following the lenses is a thin-film polariser from LAYERTEC designed for use at Brewster's angle. The polariser is coated to be highly reflective for the S-polarisation (in this case vertically out of the page and optical bench). After the polariser are two Pockels cells supplied by Cristal Laser, each cell is made up of a pair of $3\,\text{mm} \times 3\,\text{mm} \times 5\,\text{mm}$ RTP crystals which are AR coated for the laser wavelength around 1940 nm. Next is a zero-order quarter-wave plate from Thorlabs designed for operation at 2020 nm but suitable for use at 1940 nm. Finally, there is a plane output coupler to complete the cavity. Output coupler transmissions of 5 %, 10 % and 20 % were used in this work. The laser is operated with continuous pumping; therefore, any mention of repetition rate refers to the Q-switching.

The diagnostics used for the experiments in this chapter will be discussed in section 2.3 along with how they were used.

## 2.2 Aims & objectives

Now that the test laser system has been introduced, the first experiment to be done was the collection of a large data set to measure the jitter for a large number of operating conditions (different pump powers, repetition rates and output couplers). There were a number of objectives in this experiment as defined below.

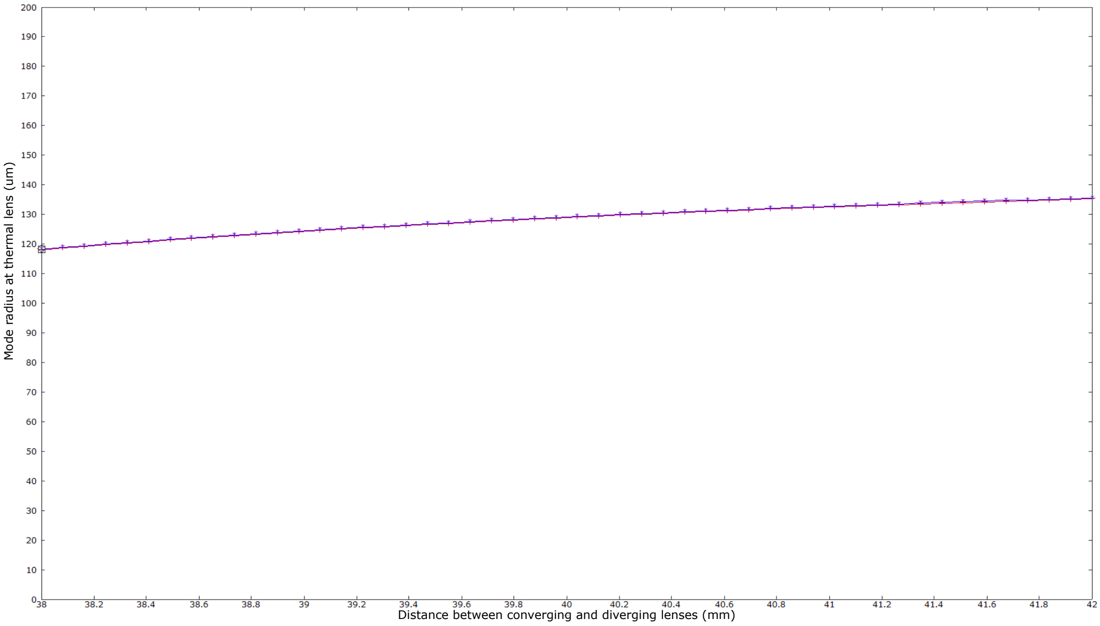

(a)

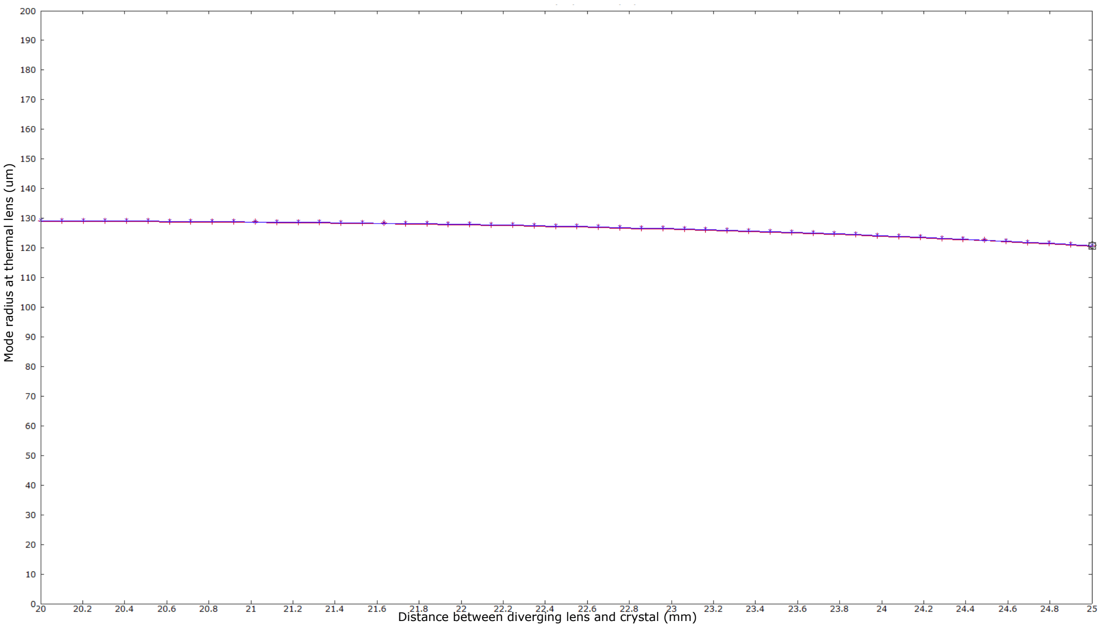

(b)

Figure 2.3: Dependency of the mode size at the thermal lens on (a) the position of the converging lens and (b) the diverging lens while the other is kept fixed at its design position and keeping the total cavity length as designed. Both shown for a thermal lens focal length of 120 mm.

1. To investigate the jitter present in the system and the effect of different operating conditions on the jitter.
2. To define a comparison point to enable the evaluation of subsequent improvements.
3. To investigate the cause of the patterns evident in the histogram and per-pulse data shown in figure 2.1.

## 2.3 Method

In order to build this benchmark data set, the waveforms of many pulses were recorded using a fast photodetector for each operating condition and then analysed in a MATLAB script. The script calculates the parameters of interest for each pulse and then returns the mean and standard deviation. This process will be discussed in more detail below.

The operating conditions studied included all possible combinations of several pump powers of 1.9 W, 2.2 W, 2.7 W, 3.5 W, 4.9 W and 6.1 W, repetition rates of 50 Hz, 125 Hz, 250 Hz, 500 Hz, 1000 Hz and 5000 Hz, and 5 %, 10 % and 20 % output couplers. Note, data was taken at extra pump powers for the combination of 250 Hz repetition rate and 5 % output coupler in order to look at one case in more detail. The maximum pump power was increased to 7.1 W when operating at 5000 Hz as this repetition rate showed a higher threshold and so more pump power was required. The CW threshold pump powers were measured to be 1.9 W, 2.2 W and 2.9 W for the 5 %, 10 % and 20 % output couplers. Table 2.1 shows the values of over-pumping ratio calculated according to $\mathrm{OP} = P_{\mathrm{pump}}/P_{\mathrm{th}}$. Recall from section 1.4.4.1 that these values are, at best, rough estimates.

Pulses were recorded using a fast photodetector (EOT5000, bandwidth >12.5 GHz, rise- and fall-time 28 ps) and a 4 GHz oscilloscope (Rohde & Schwarz RTO 1044). This model was used for two reasons: to be able to resolve mode beating at ~600 MHz on the pulses and to make use of its ‘Ultra Segmentation’ mode. This mode minimises the blind time between acquisitions by not updating the display or performing any

Table 2.1: Values of the over-pumping ratio for the pump power and output coupler combinations used in the benchmark data set. As previously stated, these are rough estimates.

| $P_{\text{pump}}$ | Output coupler | | |
|---|---|---|---|
| | 5 % | 10 % | 20 % |
| 1.9 | 1.0 | | |
| 2.2 | 1.2 | 1.0 | |
| 2.7 | 1.4 | 1.2 | 0.9 |
| 3.5 | 1.8 | 1.6 | 1.2 |
| 4.9 | 2.6 | 2.2 | 1.7 |
| 6.1 | 3.2 | 2.8 | 2.1 |
| 7.1 | | | 2.4 |

processing until after all the data has been acquired; therefore, this mode allows the recording of consecutive pulses. By contrast, a conventional oscilloscope processes the data for display after each acquisition, this processing or blind time could prohibit the recording of the next pulse. An effort was made to record 2500 consecutive pulses for each operating condition. However, the initial resolution of 0.1 ns meant that pulses with long build-up times used a large amount of memory; in these cases, pulses were recorded until the memory was full ($\sim$ 860 pulses minimum). Such a high resolution is not in fact required and so subsequent data sets presented in later chapters were taken at a lower resolution of 0.5 ns. This coarser resolution was determined to be sufficient as it allows the mode beating to be resolved and gives enough data points to measure the pulse width ($\sim$ 40 ns). The average power was measured using a Thorlabs thermal power meter (S310C). Pulses were recorded for each operating condition twice non-consecutively (ie. at least one run at a different set of parameters was done in between) and the crystal temperature and average output power were allowed to stabilise before starting the measurement.

The recorded pulses were analysed using a MATLAB script (detailed in appendix B) that calculates the build-up time, pulse duration, peak power and pulse energy for each pulse as follows. The build-up time was taken as the time period between the peak of the high-voltage noise picked up by the photodetector due to the activation of the

Pockels cell and the peak of the optical pulse, as shown in figure 2.4. The high-voltage noise was used as it is the time at which the Pockels cell activates; therefore, measuring from this time gives the true build-up time as defined in section 1.4 as the time between the losses being switched and the peak of the pulse. The pulse duration was defined as the full width at half maximum (FWHM) of the Q-switched pulse. The peak power and pulse energy require the conversion from the oscilloscope y-axis of volts to power in Watts. This was done by defining the conversion factor in equation 2.1 where $P_{avg}$ is the average power measured using the thermal power meter, $F$ is the repetition rate and $A_{avg}$ is the average area under the pulse (not the beam area). The area under each pulse is calculated by numerical integration in the script. Using this factor, the peak power (in W) is calculated as the peak value of the pulse (in V) multiplied by the conversion factor and the pulse energy (in J) is the area under the pulse (in V s) multiplied by the conversion factor.

$$C = \frac{P_{avg}}{F \times A_{avg}} \tag{2.1}$$

Once the pulse parameter values are known for each pulse, the script calculates the mean ($\mu$) and standard deviation ($\sigma$) for each parameter. The standard deviation of a distribution ($x$) is calculated using the formula in equation 2.2, where $\mu_x$ is the mean value and $n$ is the number of observations. The percentage jitter in parameter $x$ ($\Delta x$, in %) is then calculated using equation 2.3. This definition was chosen because, for the normal distribution, 99.7 % of events lie within $3\sigma$ either side of the mean as shown in figure 2.5 (it will be shown in section 2.4 that the data is approximately normally distributed). Therefore, this definition reflects the full range of values taken by the parameter and so comparisons to the targets identified in chapter 1.4.4.1 will be based on this $3\sigma$ definition; ie. $3\sigma_{\tau_{\mathrm{b}}} < 1\,\mathrm{ns}$ and $\Delta E_{\mathrm{p}} < 3\,\%$ for the build-up time and pulse energy respectively. This is a similar approach to that specified in the Quantel Laser datasheet [76], where the specified jitter is valid for 99 % of pulses. Percentage jitter values are given to 2 sf. due to the uncertainty in measurements (power meter error was ±5 % and oscilloscope resolution was 0.1 ns) and mode beating on the pulses potentially artificially amplifying the peak power. The per-pulse values for each parameter are

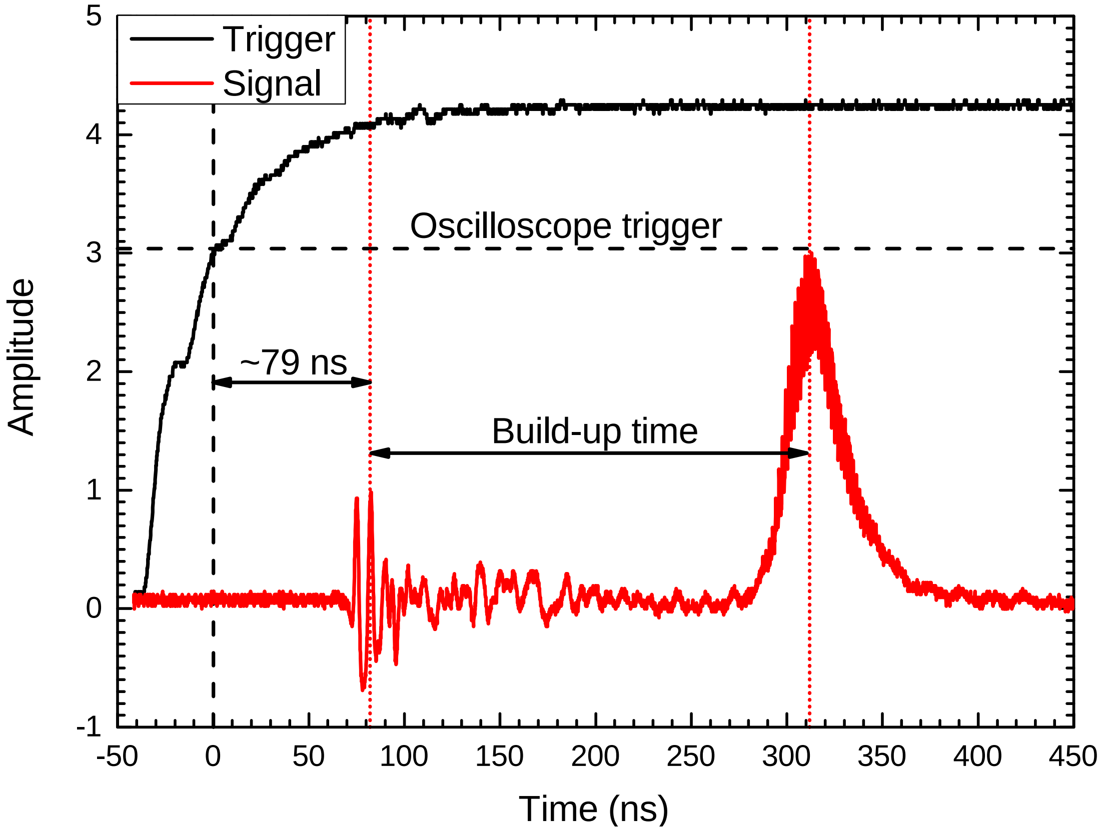

Figure 2.4: An example pulse from the benchmark data set showing the high-voltage noise in the signal. The signal has been normalised for clarity. Also marked is the build-up time definition used as well as the empirically determined time difference between the trigger signal and the Pockels cell firing (taken as the peak of the noise).

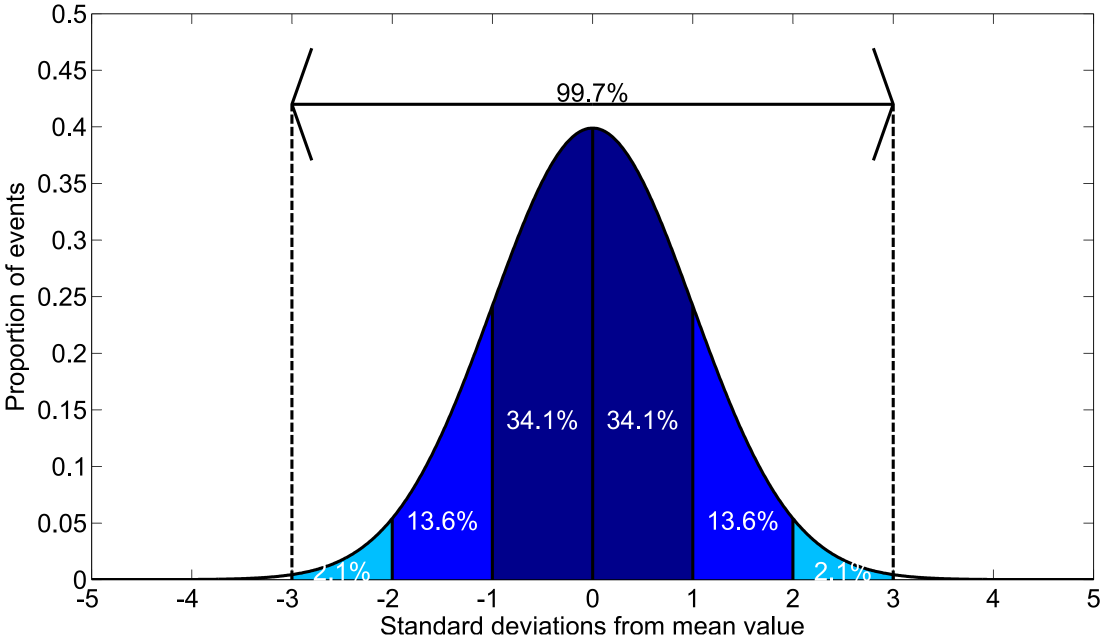

Figure 2.5: The normal distribution with the percentage of events within regions of the distribution marked. The region between $\mu - 3\sigma$ and $\mu + 3\sigma$ contains 99.7 % of events as shown.

saved to enable the visualisation of the data as shown in section 2.4.

$$\sigma_x = \sqrt{\frac{\sum(x - \mu_x)}{n}} \tag{2.2}$$

$$\Delta x = \frac{3\sigma_x}{\mu_x} \times 100 \tag{2.3}$$

In addition to the uncertainty in measurements due to the diagnostics used, there is some uncertainty introduced by the algorithm itself. Firstly, the pulses exhibit mode-beating which introduces some ambiguity into the definition of the FWHM and true position of the peak value of the pulse. This is due to the modulation causing multiple crossings of the half-maximum value and a potential shifting of the peak from pulse to pulse. This should not affect the pulse energy due to the mode-beating being averaged out during the calculation of the area under the pulse. As the mode beating is at a known frequency of $\sim 600\,\text{MHz}$, it can be expected that this will cause an uncertainty in the pulse duration and build-up time (due to potential shifting peak) of the period of the oscillation ∼ 1.7 ns. The mode-beating could be removed from the pulses by smoothing; however, this was not implemented due to the potential for artificially improving the jitter by ignoring an important phenomenon.

Another potential source of uncertainty is the potential for a change in the noise profile used to define the build-up time. Looking at the waveform shown in figure 2.4, if the first noise spike was larger than the second on the next pulse, a different build-up time would be recorded. This has the potential to introduce an uncertainty of ∼ 10 ns to the build-up time as the two noise spikes are separated by this in figure 2.4. However, it will be shown in figure 2.6a that the full range of the build-up time jitter is comparable to 10 ns making this change in noise profile, at worst, a rare occurrence in the benchmark data set. However, the histogram produced from earlier data in figure 2.1 shows three peaks separated by ∼ 10 ns. It is thought that the recording of non-consecutive pulses when taking that data introduced a selection bias that enhanced the visibility of the jitter due to the changing noise profile. As will be shown in section 2.4, no similar structure was seen in histograms when recording consecutive pulses.

## 2.4 Results

The results of applying the method discussed in the previous section will be presented here. While only some of the data will be shown here, the complete set of mean, standard deviation and percentage jitter values is given in appendix A. As stated before, the pulse parameters (build-up time, pulse duration, peak power and pulse energy) were measured under different operating conditions. These conditions included all possible combinations of pump powers between 1.9 W and 7.1 W, repetition rates in the range 50 Hz – 5000 Hz and 5 %, 10 % and 20 % output couplers. Pump powers are calculated from the angle of the half-wave plate in the variable attenuator with a calibration from a prior measurement. Values are given to 2 significant figures (sf.) as the power meter used to define the conversion has an error of ±5 %.

Upon calculating the pulse parameters for each pulse for a given set of operating conditions, the distributions can be viewed in the form of histograms. Example histograms are shown in figure 2.6 for the second measurement run for the 5 % output

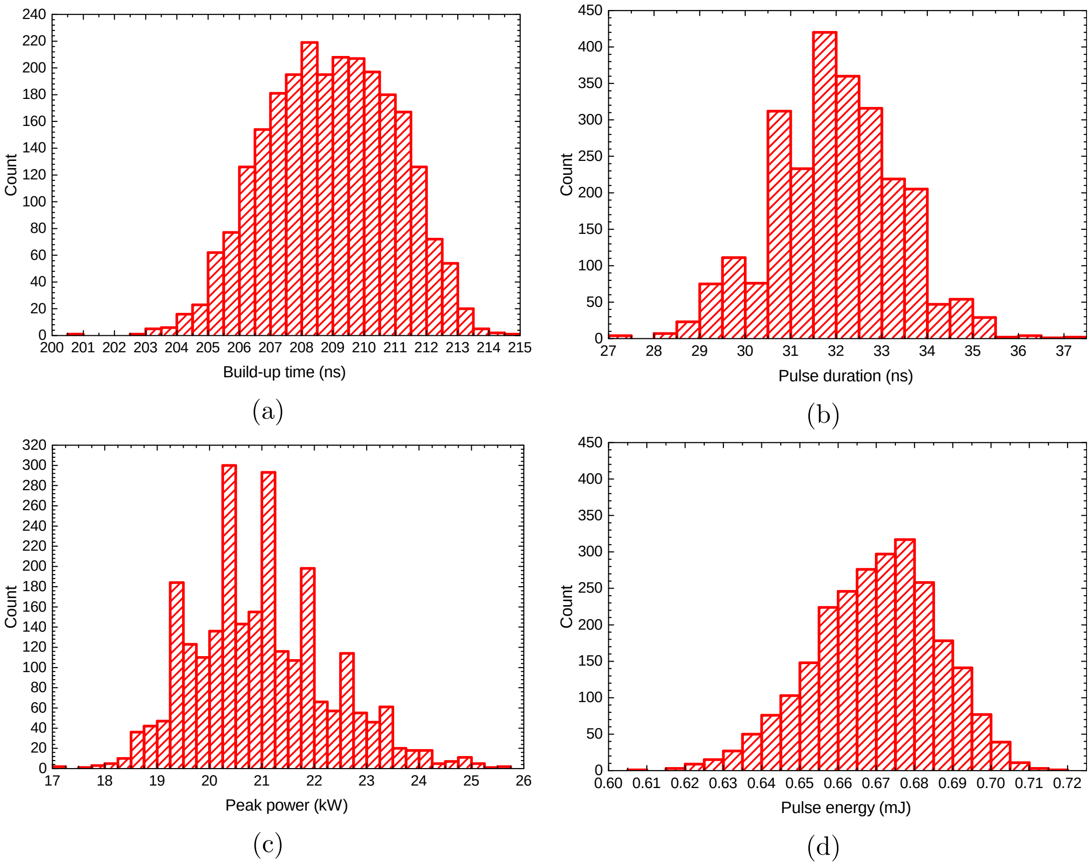

(a) (b)

(c) (d)

Figure 2.6: Histograms of the (a) build-up time, (b) pulse duration, (c) peak power and (d) pulse energy for 5 % output coupler, 250 Hz repetition rate and 4.9 W incident pump power. This is the data from the second run under the stated conditions.

coupler at 250 Hz repetition rate and 4.9 W incident pump power. The bin width of these histograms was determined by using the 'rule-of-thumb', based on the Gaussian density, given in equation 2.4 from [93], where $h_n$ is the bin width, $\sigma$ is the standard deviation (calculated previously using equation 2.2) and $n$ is the number of events (2500 in this case). The value of $h_n$ is then rounded to a number that is convenient for plotting as recommended in [93]. It should be noted that equation 2.4 only gives the optimal bin width if the data is normally distributed [93]; it can be seen in figure 2.6 that this is approximately true and the value is taken as a guide only.

$$h_n = 3.49\sigma n^{-\frac{1}{3}} \tag{2.4}$$

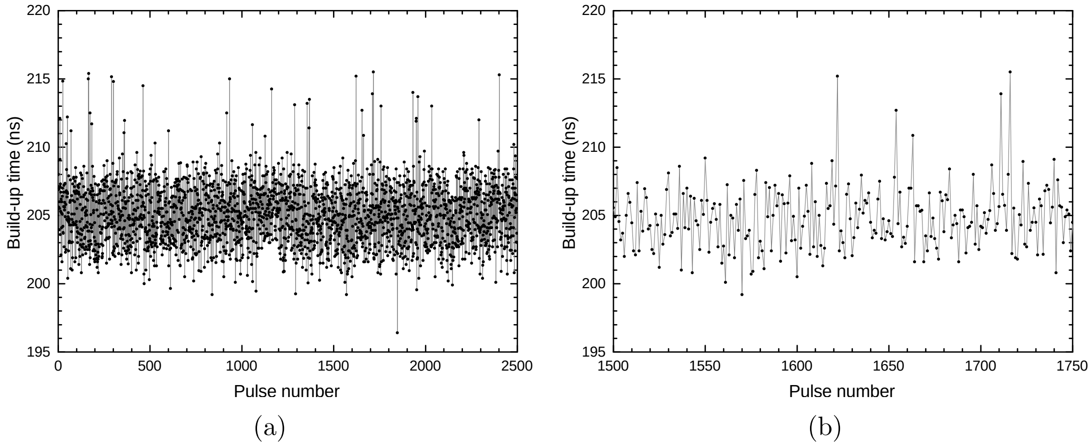

Figure 2.7: Build-up time against pulse number for the second data run with 5 % output coupler, 250 Hz repetition rate and 4.9 W incident pump power. (a) All 2500 pulses, (b) zoom in on pulses 1500 – 1750.

While the histograms show the overall distribution of the parameters as an ensemble, they give no information on pulse-to-pulse variations. Thanks to the 'Ultra-Segmentation' mode on the oscilloscope, consecutive pulses are recorded and so the pulse parameters can be plotted against pulse number to show temporal information. An example is shown in figure 2.7a for the same data shown in figure 2.6a. No obvious patterns were seen in any plots such as the one shown except for oscillations about the mean value as depicted in figure 2.7b, which shows a zoom in on 250 pulses to allow this to be seen more clearly. The fact that no patterns, such as the grouping in figure 2.1, appear in either the histograms or the per-pulse plots implies that the grouping was a rare occurrence or was due to those initial measurements not looking at consecutive pulses.

Having looked at the pulse-to-pulse variations for one set of operating conditions, this analysis will now move on to compare the jitter across operating conditions to investigate the effects on jitter. Therefore, comparisons will be made using the mean value, standard deviation and percentage jitter (defined in equation 2.3) in each parameter.

First, the effect of the incident pump power will be considered. Figure 2.8 shows the jitter against incident pump power for the case of the 5 % output coupler at a repetition rate of 250 Hz. Although there is some variation between the two data runs, the general trend shows that the jitter decreases with increasing pump power. This is to be expected as a higher pump power corresponds to a higher value of the over-pumping ratio and, as discussed in section 1.4.4.1, this should lead to a reduction in the jitter in the system. However, while operating at a higher pump power does reduce the jitter, it does not minimise it sufficiently; the minimum build-up time jitter (with the 5 % output coupler and at a repetition rate of 250 Hz) was $3\sigma_{\tau_\mathrm{b}} = 4.4\,\mathrm{ns}$ at the maximum pump power of 6.1 W. Applications discussed in section 1.4.4.1 (such as stable cavity dumping) require the build-up time jitter to be no more than $3\sigma_{\tau_\mathrm{b}} = 1\,\mathrm{ns}$. The minimum percentage jitter achieved in the pulse duration, peak power and energy were 9.0 %, 17 % and 5.0 % respectively and occurred at different pump powers (2.4 W, 6.1 W and 4.6 W), implying that there are other factors affecting the jitter than just the pump power. The percentage jitter in the pulse energy is also above the target level of $\Delta E_\mathrm{p} < 3\,\%$.

Next, the effect of the repetition rate will be investigated. Figure 2.9 shows the jitter against the repetition rate for the case of the 5 % output coupler and an incident pump power of 4.9 W. Again, there is some variation between the two data runs but it is obvious that the jitter is prohibitively high at a repetition rate of 5 kHz. The variation between the data runs was not expected and could be due to different lab conditions when the data were taken - during these experiments no effort was made to control the lab environment. This was also the case at 1 kHz for lower pump powers. In general, higher repetition rates showed more jitter at low pump powers compared to lower repetition rates (see tables in appendix A). This is to be expected as higher repetition rates mean shorter pumping times and therefore, at the same incident pump power, a smaller over-pumping ratio as outlined in section 1.4.4.1.

Finally, the effect of the output coupling on the jitter will be examined. Table 2.2 shows the mean value, standard deviation and percentage jitter of each parameter for each output coupler for the case of a repetition rate of 250 Hz and incident pump power of 4.9 W. From this table, it can be seen that the jitter is worse with the 20 % output coupler as, taking the average of the two runs, the standard deviation and percentage jitter in each parameter increases with output coupling. This is expected as a higher output coupling means greater losses in the cavity which leads to a lower

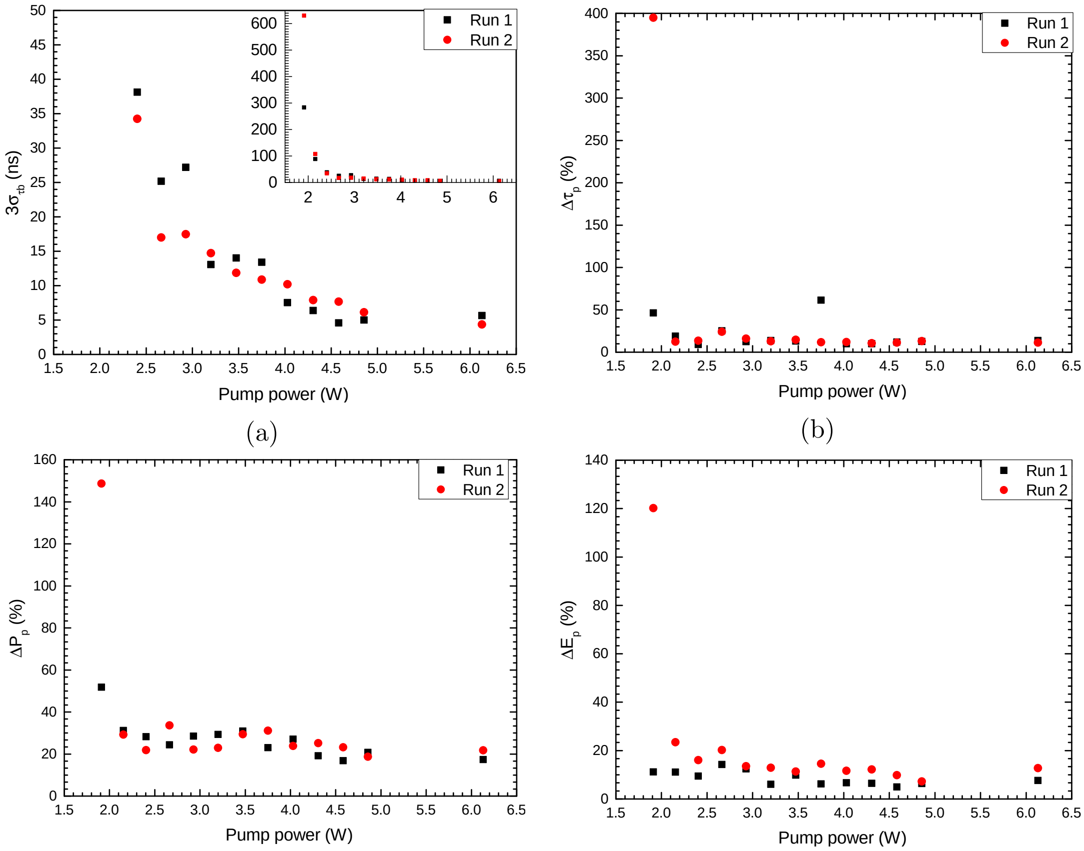

(a) (b)

(c) (d)

Figure 2.8: Jitter in (a) build-up time (where the inset shows the full range), (b) pulse duration, (c) peak power and (d) pulse energy as a function of incident pump power. Both data runs for the 5 % output coupler at a repetition rate of 250 Hz are shown.

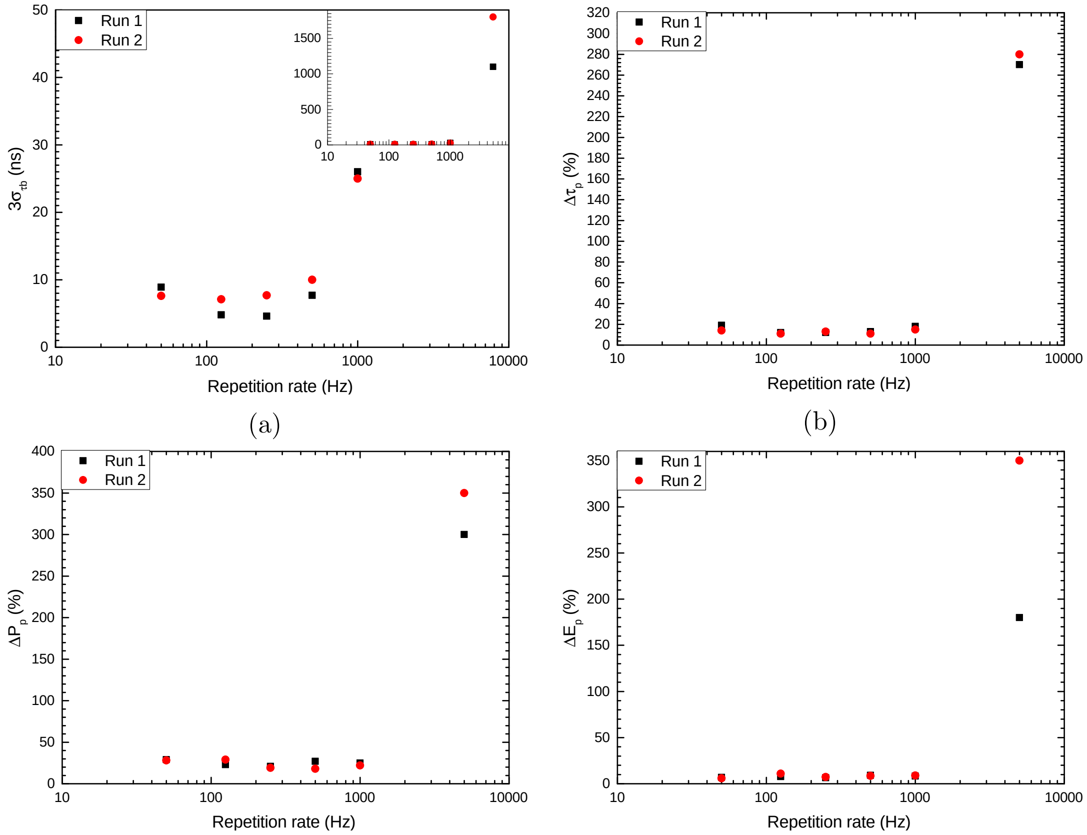

(a) (b)

(c) (d)

Figure 2.9: Jitter in (a) build-up time (where the inset shows the full range), (b) pulse duration, (c) peak power and (d) pulse energy as a function of repetition rate. Both data runs for the 5 % output coupler and an incident pump power of 4.9 W are shown.

Table 2.2: Mean, standard deviation and percentage jitter values of each parameter for the different output couplers used. All data taken at a repetition rate of 250 Hz and incident pump power of 4.9 W.

| Output coupler (%) | Build-up time | | | Pulse duration | | | Peak power | | | Pulse energy | | |
|---|---|---|---|---|---|---|---|---|---|---|---|---|
| | $\mu_{\tau_\mathrm{b}}$ (ns) | $3\sigma_{\tau_\mathrm{b}}$ (ns) | $\Delta\tau_\mathrm{b}$ (%) | $\mu_{\tau_\mathrm{p}}$ (ns) | $3\sigma_{\tau_\mathrm{p}}$ (ns) | $\Delta\tau_\mathrm{p}$ (%) | $\mu_{P_\mathrm{p}}$ (kW) | $3\sigma_{P_\mathrm{p}}$ (kW) | $\Delta P_\mathrm{p}$ (%) | $\mu_{E_\mathrm{p}}$ (mJ) | $3\sigma_{E_\mathrm{p}}$ (µJ) | $\Delta E_\mathrm{p}$ (%) |
| 5 | 200 | 5.0 | 2.6 | 31 | 3.9 | 12 | 19 | 3.9 | 21 | 0.72 | 46 | 6.4 |
| | 210 | 6.1 | 2.9 | 32 | 4.1 | 13 | 21 | 3.9 | 19 | 0.67 | 49 | 7.3 |
| 10 | 250 | 6.8 | 2.7 | 35 | 3.7 | 10 | 30 | 6.5 | 22 | 1.0 | 130 | 13 |
| | 270 | 10 | 3.7 | 37 | 17 | 45 | 28 | 6.1 | 22 | 1.1 | 120 | 11 |
| 20 | 460 | 31 | 6.7 | 54 | 5.2 | 9.6 | 17 | 4.6 | 27 | 0.86 | 150 | 18 |
| | 440 | 28 | 6.4 | 52 | 13 | 25 | 20 | 7.4 | 37 | 0.85 | 65 | 7.7 |

over-pumping ratio (for the same pump power and pumping time) and therefore more jitter, as explained in section 1.4.4.1.

## 2.5 Pump stability

As identified in chapter 1.4.4.1, changes in over-pumping ratio (and therefore causes of jitter) can be due to variations in the pump or cavity losses. Therefore, the pump laser diode stability was investigated by recording its output over timescales of interest, see figure 2.10, with a fast photodetector (Thorlabs DET10A/M). The timescales chosen correspond to the pumping time when operating at 250 Hz repetition rate (4 ms) and a longer time to judge the difference between two pumping times (10 ms). Variations of $\sim \pm 1$ mV were observed in both cases; when ND filters were removed from in front of the detector to increase the signal from $\sim 130$ mV to $\sim 400$ mV, the fluctuations remained at the $\pm 1$ mV level. This lead to the conclusion that the fluctuations are just electrical noise in the detector and the laser diode is stable to the limits of detection.

This was further evidenced in a later experiment that looked at the fluorescence from the laser crystal during Q-switching. The fluorescence rate is proportional to the population of the upper-laser-level and so recording the fluorescence around the laser wavelength can give some insight into the population dynamics of the laser [94]. The setup for monitoring the fluorescence is shown schematically in figure 2.11. The detector

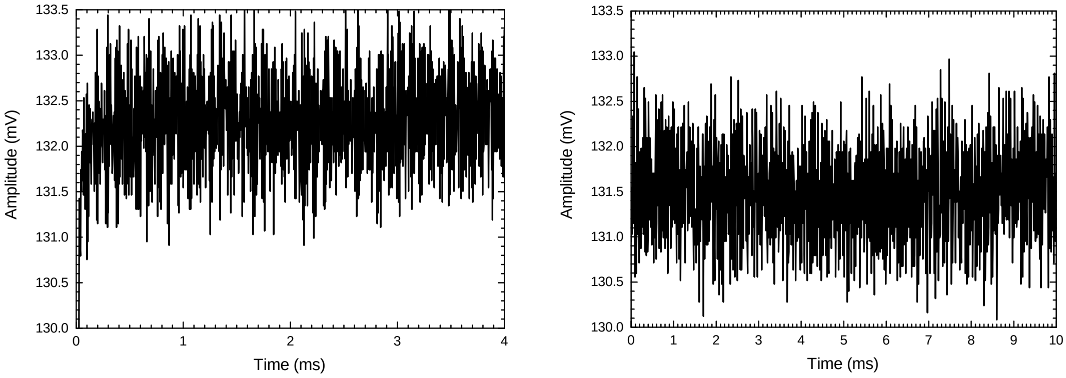

(a) (b)

Figure 2.10: Pump diode stability over (a) 4 ms and (b) 10 ms.

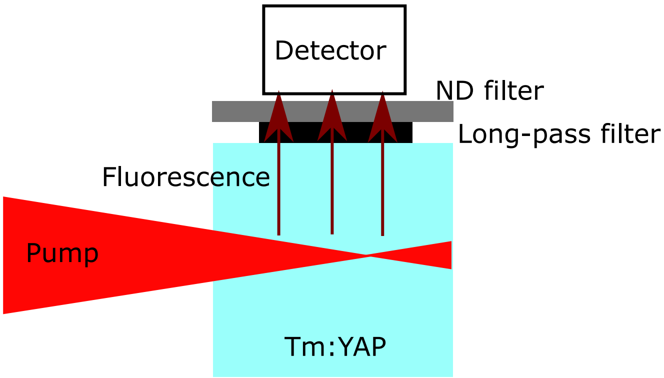

Figure 2.11: Schematic of the setup for taking the fluorescence measurements.

used was a Hamamatsu large-area (diameter 3 mm) InGaAs photodiode (G12182-030K) with a differential amplifier circuit and filter to block pump light. The detector is slow compared to the Q-switched pulse but can be used to probe the upper laser level population before the pulse. In a similar method to that described for taking jitter measurements described in section 2.3, many (444) consecutive waveforms were recorded. An average of the signal before the pulse was taken to be the fluorescence level at that point and was compared across the waveforms just as when investigating the jitter. It was found that the level before the pulse only varied by 0.082 % ($3\sigma/\mu$ value), demonstrating the stability of the pump diode as well as implying that the pumping phase "washes out" any differences in population inversion after the pulse.

## 2.6 Conclusions

Having presented the results of and explained the method used to create the benchmark data set, this section will sum up the main conclusions of this work.

First, no patterns were found in the data taken like that shown in figure 2.1 where multiple peaks appeared in the histogram. In fact, the data are approximately normally distributed. It is believed that the structure seen in figure 2.1 is due to that data not being comprised of consecutive pulses, leading to a selection bias or under-sampling in the measurement.

Secondly, the trends that were seen were expected. Increasing the pump power reduced the jitter in all parameters due to operating at higher over-pumping ratios. Higher repetition rates increased the jitter due to the reduced pumping time reducing the over-pumping ratio. Increased output coupling also lead to an increase in the jitter, this is due to higher losses reducing the over-pumping ratio for a given pump power.

Thirdly, future data sets can be made considerably smaller as it has been shown that the output coupler affects the jitter in the predicted way; the increased loss reduces the over-pumping ratio and therefore leads to more jitter. As such, future data sets will only consider one output coupler. The 5 % output coupler was chosen as this represents the lowest loss and therefore the shortest build-up times which will lead to smaller data files when recording data making data processing easier. Furthermore, the time resolution used when recording the benchmark data set (0.1 ns) was excessive and can be reduced without negatively impacting the quality of data recorded. Future data sets will use a time resolution of 0.5 ns. This will reduce file sizes and the time required to complete a data set. Additionally, there is no need to take data at all repetition rates; the percentage jitter does not appear to be correlated to the repetition rate for pump powers above $\sim$ 3.5 W (see appendix A for full data). The exception to this is that the jitter at 5 kHz is prohibitively large. Due to these arguments, it is reasonable to take data at just the one repetition rate in the future; 250 Hz was chosen as this is comparable to the inverse upper laser level lifetime (4.4 ms, see chapter 1.3.1.1) which gives the ideal pumping time [16]. Subsequent analyses will also focus on just one pump power, 4.9 W (corresponding to an over-pumping ratio of 2.6, although this is only a rough estimate) was chosen as this puts the laser comfortably above threshold but still away from the limits of operation where performance degradation might be expected.

The pump diode laser was found to be stable to the limits of detection by two methods – direct monitoring of its output over timescales of interest and by fluorescence measurements demonstrating that the population inversion before the pulse varies by only 0.082 %. Therefore, it can be concluded that the main cause of jitter is fluctuations in the cavity losses; identifying and controlling these sources of loss will be discussed in the following chapters.

Finally, it is important to remember that this data set forms a comprehensive benchmark for comparison with future data sets in order to evaluate the success of improvements made.

# Chapter 3

# Initial Mode Control Experiments

As mentioned in chapter 1.4.4.2, single-frequency operation has been linked to reduced jitter in passively Q-switched systems [85–87]. It has also been shown that the instabilities seen in passively Q-switched two-mode microchip lasers are due to longitudinal-mode competition [86]. In reference [95] it was shown that as more longitudinal modes are allowed to oscillate, periodic changes in output amplitudes appear. Similarly, a reduction in timing jitter from 18.4 µs to 4.8 µs was attained in a passively Q-switched Nd:YAG laser by enforcing single-transverse mode operation [96]. Based on this prior work, efforts were made to control the number of modes the Tm:YAP laser can oscillate on. To this end, etalons were used to reduce the number of longitudinal modes and a pinhole to restrict the transverse modes. It was found that reducing the number of longitudinal modes *increased* the jitter, although the etalons used could not enforce single-longitudinal-mode operation, while forcing the $\text{TEM}_{00}$ mode had no effect on the jitter.

This chapter will describe the initial attempts made to control both the longitudinal and transverse mode content of the Q-switched laser and the subsequent effects on the jitter.

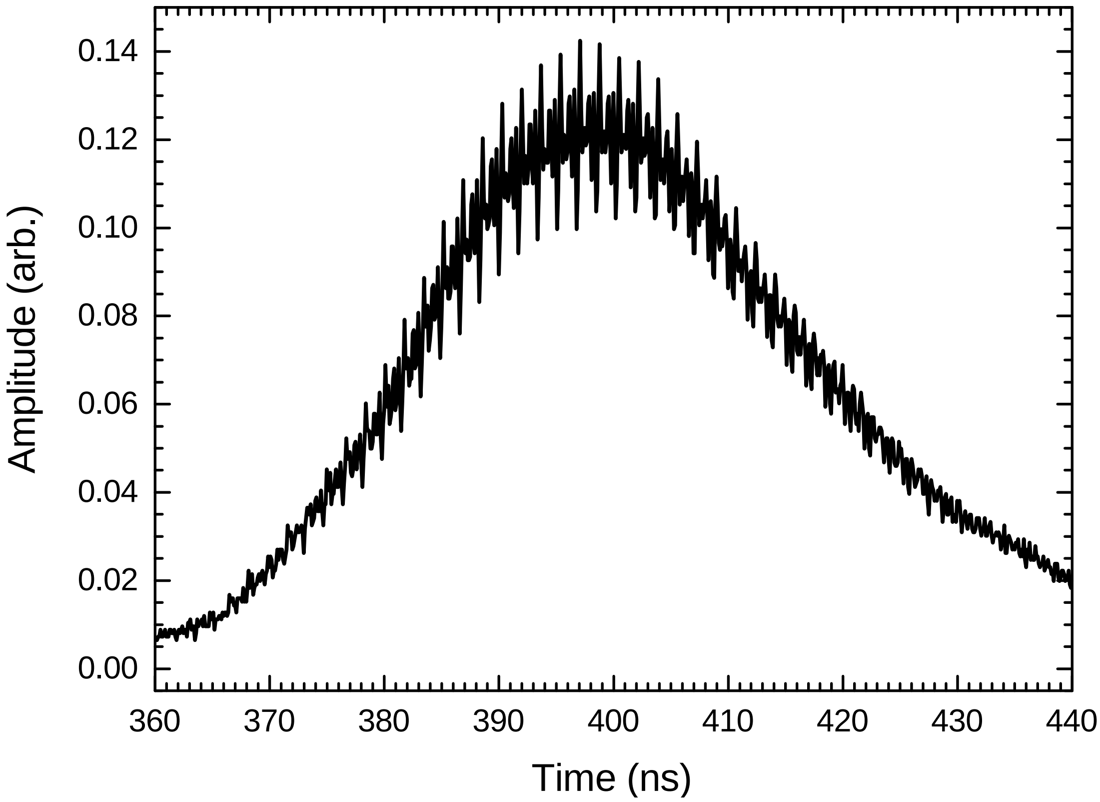

Figure 3.1: Example pulse showing mode beating at ∼590 MHz.

## 3.1 Longitudinal mode control

While recording the data for the benchmark data set, significant mode beating was observed on all pulses. An example is shown in figure 3.1. Mode beating is an amplitude modulation effect that occurs whenever a laser is operating on more than a single longitudinal mode. This spiking is known to be mode beating as it is at a frequency of ∼590 MHz which corresponds to the mode spacing of the cavity. The evidence of multi-longitudinal-mode operation from mode beating was subsequently corroborated by Fabry-Perot measurement that will be described in chapter 3.1.2.

To the author's knowledge, no explanation has been proposed for the link between mode beating (and therefore multi-longitudinal mode operation) and jitter; the author's thoughts on the matter are as follows. Different modes experience different gain and loss in the cavity (however slight) and so have slightly different build-up times. This leads to a certain build-up time (and duration, peak power and energy) for the output pulse formed from the combination of these modes. If some change occurs in the cavity before the arrival of the next pulse, a different mode (or set of modes) could dominate the build up of the next pulse; causing it to exhibit different pulse parameters compared to the previous one. Hence the competition between modes during the pulse build up phase contributes to the jitter in the system. If, however, the laser runs single-frequency, then there is no competition and the pulse should have the same build-up time all the time.

In order to investigate the effect of mode content on jitter, etalons were used to reduce the number of modes the laser can oscillate on. A number of wavelength selective elements exist [21], including Volume Bragg Gratings (VBGs), birefringent filters (and variants such as Lyot filters), Fabry-Perot etalons, prisms and acousto-optic filters. However, etalons were chosen due to their simplicity, relatively low cost and lack of polarisation dependence [19] (key to ensure minimal interference with electro-optic Q-switching). In contrast, VBGs were found to be too expensive for a proof-of-concept system, prisms introduce an unwanted beam deviation and it has been reported that the losses introduced by a Lyot filter were insufficient to overcome the high gain in a Q-switched Tm:YLF laser [19].

The rationale behind the choice of etalons is discussed in section 3.1.1, followed by a description of the methods used to investigate the effect of mode selection on the laser and jitter in section 3.1.2. Section 3.1.3 presents the results of these experiments and the conclusions drawn will be discussed in section 3.3.

### 3.1.1 Etalon choice

An interactive MATLAB script was developed to aid in choosing appropriate etalons. Figure 3.2 shows a schematic detailing the operation of an etalon. The transmission of a single etalon (neglecting absorption in the etalon) is given in equation 3.1 [16] where $R$ is the reflectivity of each face (assumed to be the same), $2\phi$ is the phase change between successive multiple reflections and is given by equation 3.2. $n$ is the refractive index of the etalon material, $L$ is the thickness, $\theta$ is the angle the ray makes to the surface normal *inside* the etalon and is related to the incidence angle by $n \sin\theta = \sin\theta'$, $\nu$ is the

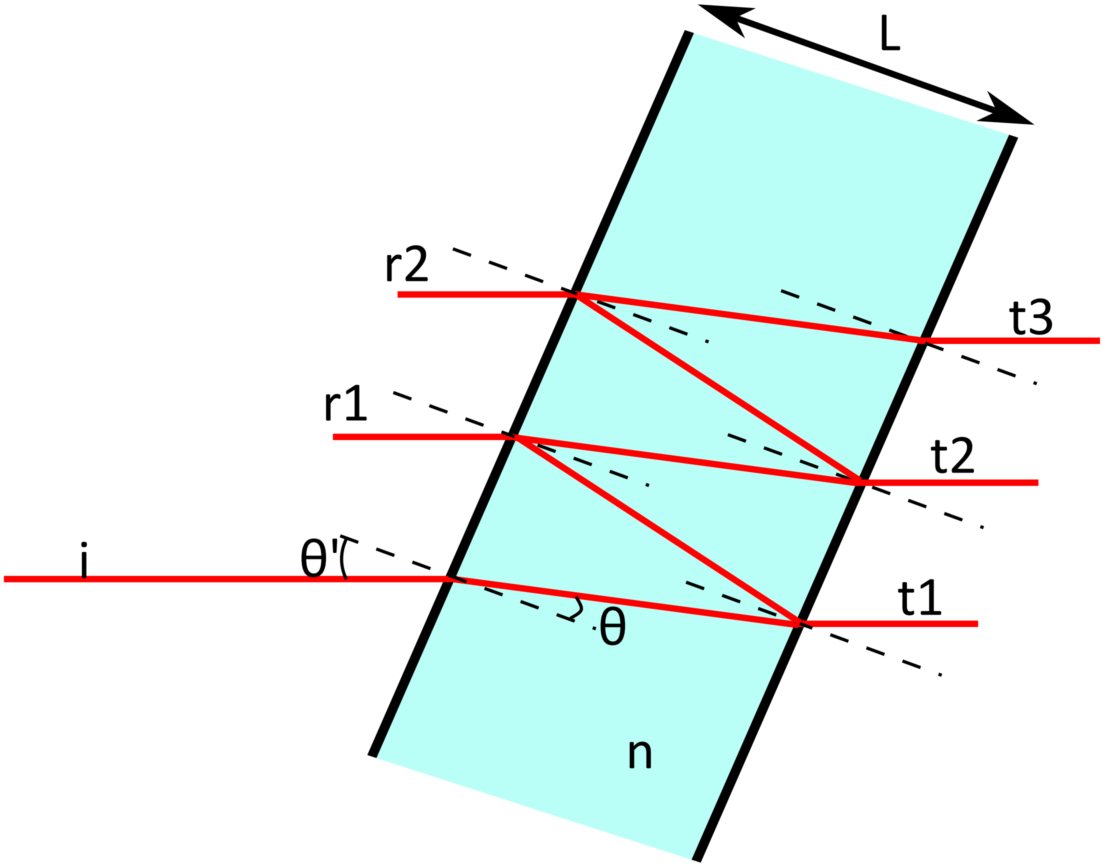

Figure 3.2: Schematic of an etalon. Rays are marked i for incident, r for reflected and t for transmitted. $\theta'$ is the incidence angle, $\theta$ is the angle of the ray (compared to the surface normal) inside the etalon, $L$ is the thickness and $n$ is the refractive index of the etalon material. Rays t1, t2, ..., tn add constructively and rays r1, ..., rn interfere destructively with ray i to give maximum transmission for a certain wavelength at the angle of incidence. Adapted from [16].

optical frequency and $c$ is the speed of light. The total transmission of multiple etalons is found by multiplying the transmission of each etalon together. Having been given the etalon material (and knowing its refractive index) and thickness, the script maximises transmission at the peak of the emission spectrum in figure 1.3a [4] by varying the angle $\theta'$ of each etalon.

$$T_{\text{etalon}} = \frac{(1-R^2)}{(1-R)^2 + 4R\sin^2\phi} \tag{3.1}$$

$$\phi = \frac{2\pi n L \nu \cos\theta}{c} \tag{3.2}$$

Etalon choices are limited to three materials: silicon, YAG and ZnSe as these are the three commercially available materials suitable for (ie. transparent at) 2 µm. ZnSe was quickly discounted due to the smaller choice on offer and toxicity concerns. Silicon etalons have a naturally high finesse due to the high refractive index (3.46 at 1.94 µm [97]) but, as will be described below, suffer from two-photon absorption at high powers. YAG does not suffer from this non-linear absorption but has a lower refractive index (1.80 at 1.94 µm [98]) than silicon and therefore YAG etalons have a lower finesse than their silicon counterparts.

Due to the high intensities inside the laser cavity during Q-switching (peak powers of the order of tens of kW were recorded through a 10 % output coupler, meaning intracavity powers of greater than 100 kW), it was decided to use only uncoated etalons to minimise the chance of optical damage to the etalon surfaces. Therefore, the reflectivities are given by the Fresnel reflection $R = (1-n)^2/(1+n)^2$ (as long as the angles considered are small). The script allows the user to specify thicknesses of up to three etalons and calculates the optimal angles for maximum transmission at the wavelength corresponding to the peak of the stimulated emission cross-section. Once the total transmission of the etalons at the optimal angles has been calculated, it is up to the user to analyse the result and determine the best combination of etalons. The best combination gives the most discrimination between the central mode and all others as well as maximum transmission for the central mode.

Limiting the etalon thicknesses to those available "off-the-shelf" from LightMachinery, silicon etalons with thicknesses of 4.155 mm and 0.416 mm were found to offer the best simulated performance (shown in figure 3.3). This is due to the high finesse of these etalons, due to the high refractive index of silicon, defining narrow peaks in the transmission spectrum and therefore good discrimination against adjacent modes. These were tested in the laser cavity and worked well during CW operation. However, both the average and peak output powers were significantly reduced when Q-switching the laser compared to before the etalons were added as shown in figure 3.4, where the approximate peak power has been calculated according to equation 3.3 with $P_{\text{peak}}$ and $P_{\text{avg}}$ being the peak and average power respectively, $\tau_{\text{p}}$ the pulse duration and $f$ the repetition rate. This is believed to be due to 2-photon absorption in the silicon, which is known to be a problem in silicon-waveguide-based Raman lasers [99, 100]. Pump depletion (ie absorption of the $\sim 2\,\mu$m light) was said to be negligible for the Raman lasers [100] (citing an earlier work [101]). However, the etalons used in this laser are exposed to much higher powers (of the order kW as opposed to mW [101]) and, since 2-photon absorption is a non-linear process, it is reasonable to expect a greater effect in this case.

$$P_{\text{peak}} = \frac{P_{\text{avg}}}{\tau_{\text{p}} \times f} \tag{3.3}$$

Following this, the etalon material was changed from silicon to YAG (which suffers no 2-photon absorption at $2\,\mu$m). Of the YAG etalons available, the MATLAB script gave 5 mm and 0.25 mm thicknesses as offering the most discrimination between the central mode and all others. The transmission of this combination is shown in figure 3.5. The finesse (values from LightMachinery Inc. etalon designer) of these etalons ($\sim 1.0$) is worse than silicon ($\sim 2.5$) due to the lower refractive index of YAG.

### 3.1.2 Setup and method

Having decided upon the etalons to be used, they were inserted into the cavity in the position shown in figure 3.6a; however, the exact position of the etalons was not as critical as allowing sufficient space for them to rotate. The total cavity length was shortened when the etalons were present in order to keep the mode spacing the same as before ($\sim$ 600 MHz). Figure 3.6b shows the beam profile in the cavity. An optical spectrum analyser (OSA, Yokogawa AQ6375, resolution 0.05 nm or 10 GHz, operated in peak hold mode to ensure a pulse is emitted during the measurement time) was used initially to record the spectrum of the laser with and without etalons. A Thorlabs Fabry-Perot interferometer with a free-spectral range of 10 GHz (SA210-18B) in conjunction with a boxcar integrator, the operation of this will be discussed in the next section, was used later to look at the number of modes the laser was oscillating

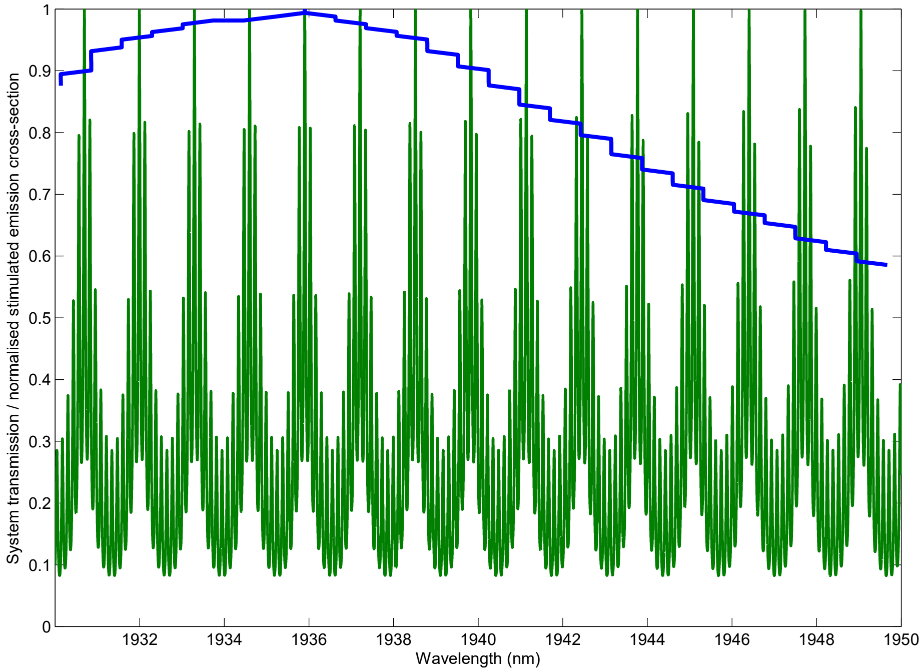

(a)

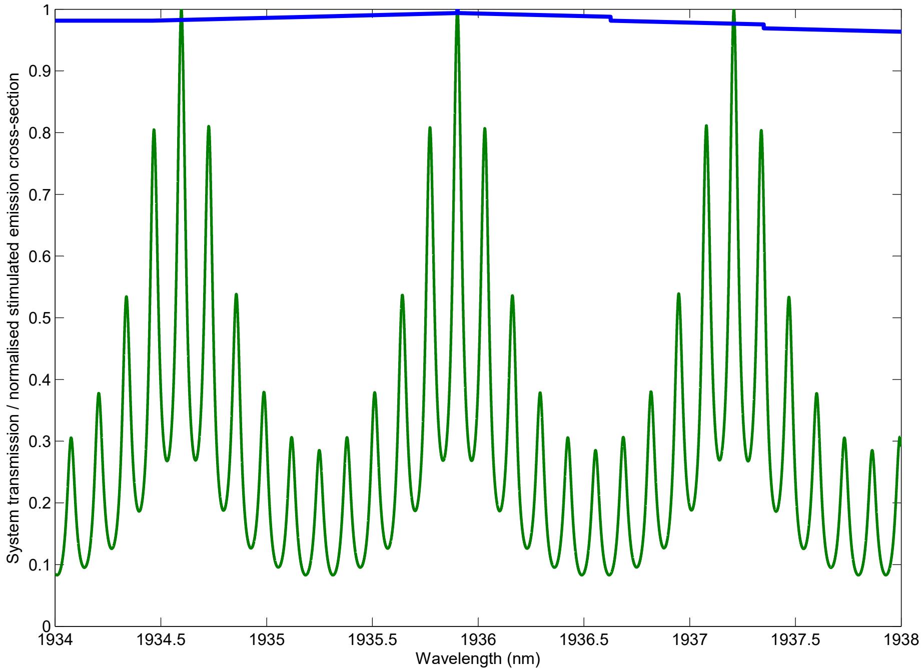

(b)

Figure 3.3: Normalised stimulated emission cross-section of a-cut Tm:YAP (blue) and transmission of the combination of 4.155 mm and 0.416 mm Silicon etalons (green). (a) full simulated range. (b) zoom in on peak of emission cross-section around 1936 nm.

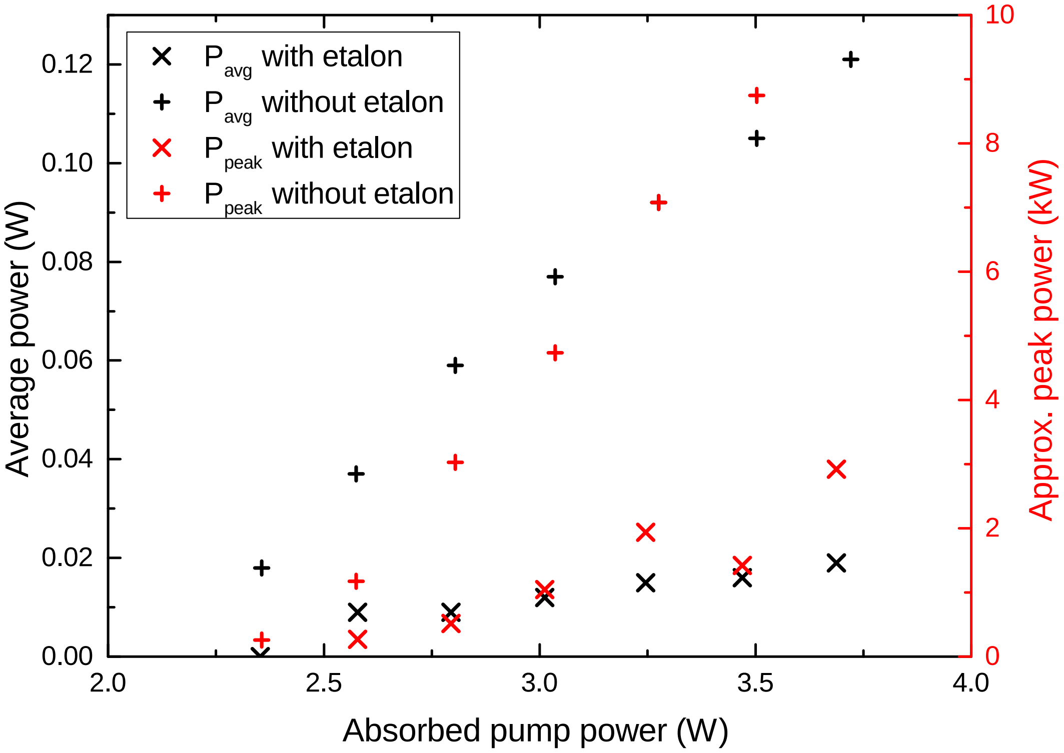

Figure 3.4: Q-switched power transfers for the measured average power and calculated peak power with and without a 0.416 mm thick silicon etalon in the cavity. Data taken at a repetition rate of 250 Hz with a 10 % output coupler.

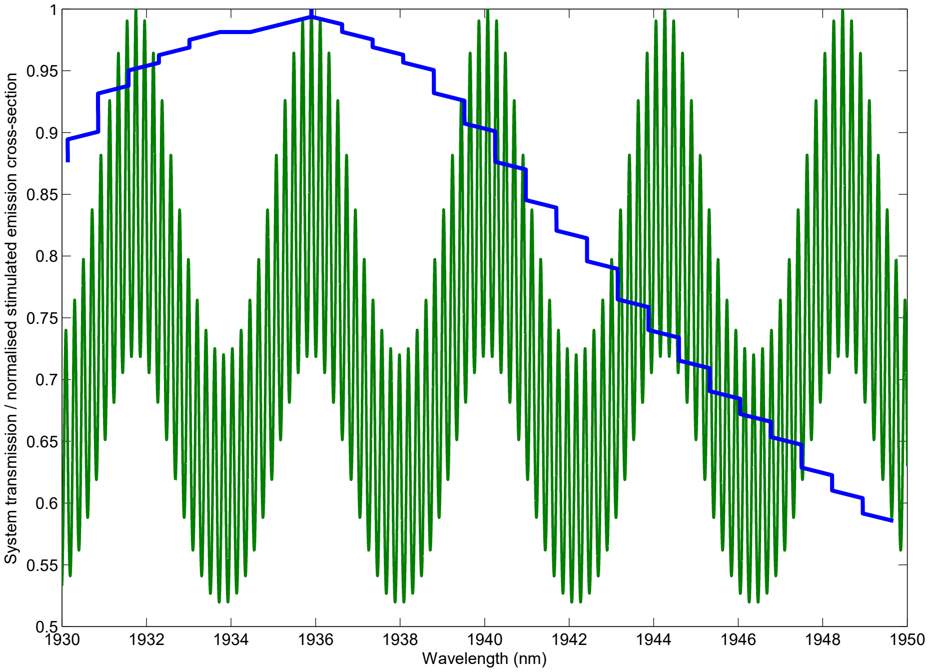

(a)

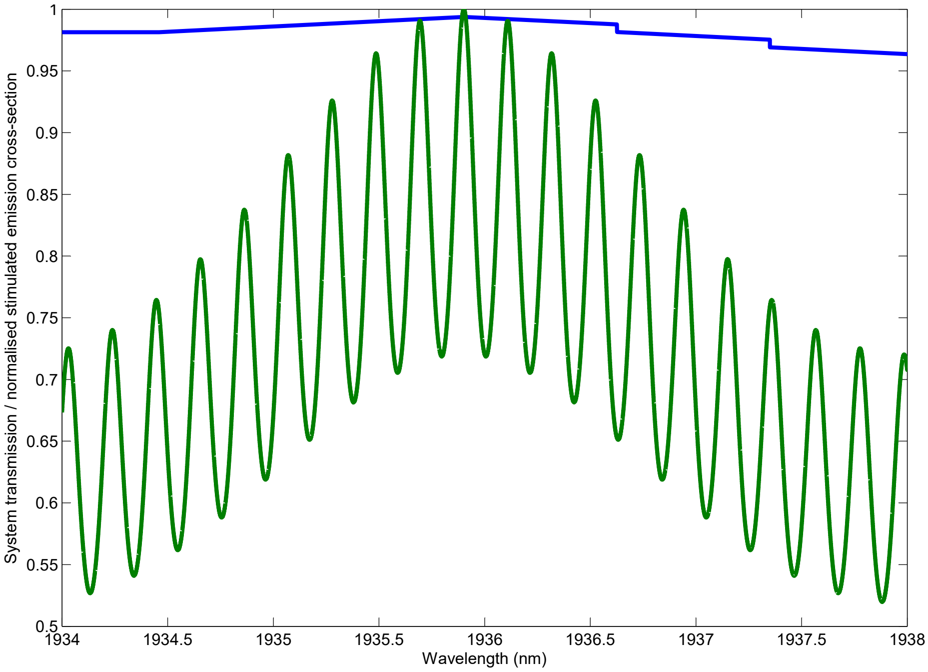

(b)

Figure 3.5: Normalised stimulated emission cross-section of a-cut Tm:YAP (blue) and transmission of the combination of 5 mm and 0.25 mm YAG etalons (green). (a) full simulated range. (b) zoom in on peak of emission cross-section around 1936 nm.

on.

The laser was run at a repetition rate of 250 Hz with an incident pump power of 4.9 W and the 5 % output coupler. The spectra in figure 3.7 were recorded using the OSA for the different possible combinations of etalons (none, 5 mm only, 0.25 mm only and both). As can be seen, only with both etalons in the cavity can the laser be forced to produce a single peak on the OSA. However, even in this case, the laser still operates multi-mode as the mode beating is still visible on the oscilloscope trace of the pulses. This is due to the large gain available when the cavity losses are switched overcoming the loss difference between modes. The $\sim 0.5\,\%$ loss difference between adjacent modes might have been enough to force single-frequency operation in a CW laser but not the Q-switched.

The effects on the jitter and further experiments to investigate the spectra are described in the next section.

### 3.1.3 Results and discussion

As etalons were added to the cavity, the jitter was measured using the method described in section 2.3. The results are shown in table 3.1. The mean values of the build-up time and pulse duration increased and the peak power and pulse energy decreased as etalons were added due to increasing the cavity losses. Jitter in all parameters is worse with both etalons than with none. Specifically, the jitter ($3\sigma$ values) in the build-up time, pulse duration, peak power and energy increased from 5.5 ns, 0.45 ns, 0.79 kW and 29 µJ to 17 ns, 1.1 ns, 1.6 kW and 59 µJ respectively with both etalons in the cavity. Curiously, the $3\sigma$ and percentage jitter values for the duration, peak power and energy are highest for the 5 mm etalon on its own. It is unknown why this is the case but could be due non-optimal alignment of the etalon.

The proposed explanation for the increased jitter is that mode competition effects are becoming worse as the mode content is restricted. When a laser operates on several longitudinal modes, the modes can vary in intensity and frequency without changing the total output power of the laser [102]. These changes in longitudinal mode spectrum can be caused by temperature and vibration. It has been observed that these

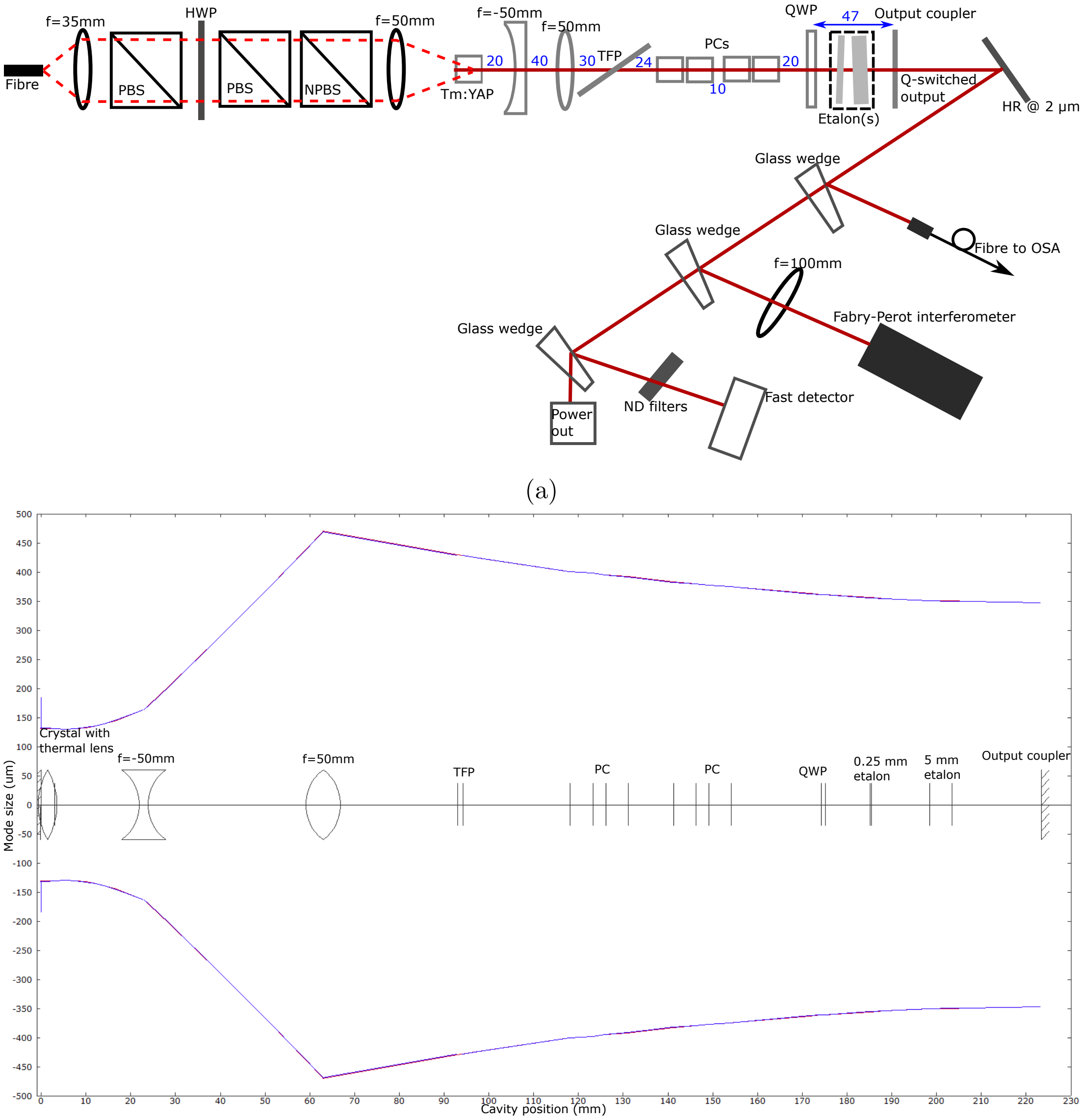

(a)

(b)

Figure 3.6: (a) Cavity diagram showing etalon position and additional diagnostics used while testing the effect of mode control on the jitter. PBS = polarising beamsplitter, NPBS = non-polarising beamsplitter, HWP = half-wave plate, TFP = thin-film polariser, PCs = Pockels cells, QWP = quarter-wave plate. Optic spacings in mm are shown in blue and there is a 3 mm gap between the crystals that make up each Pockels cell as before. (b) Mode spacing throughout the cavity when the simulated thermal lens has a focal length of 120 mm.

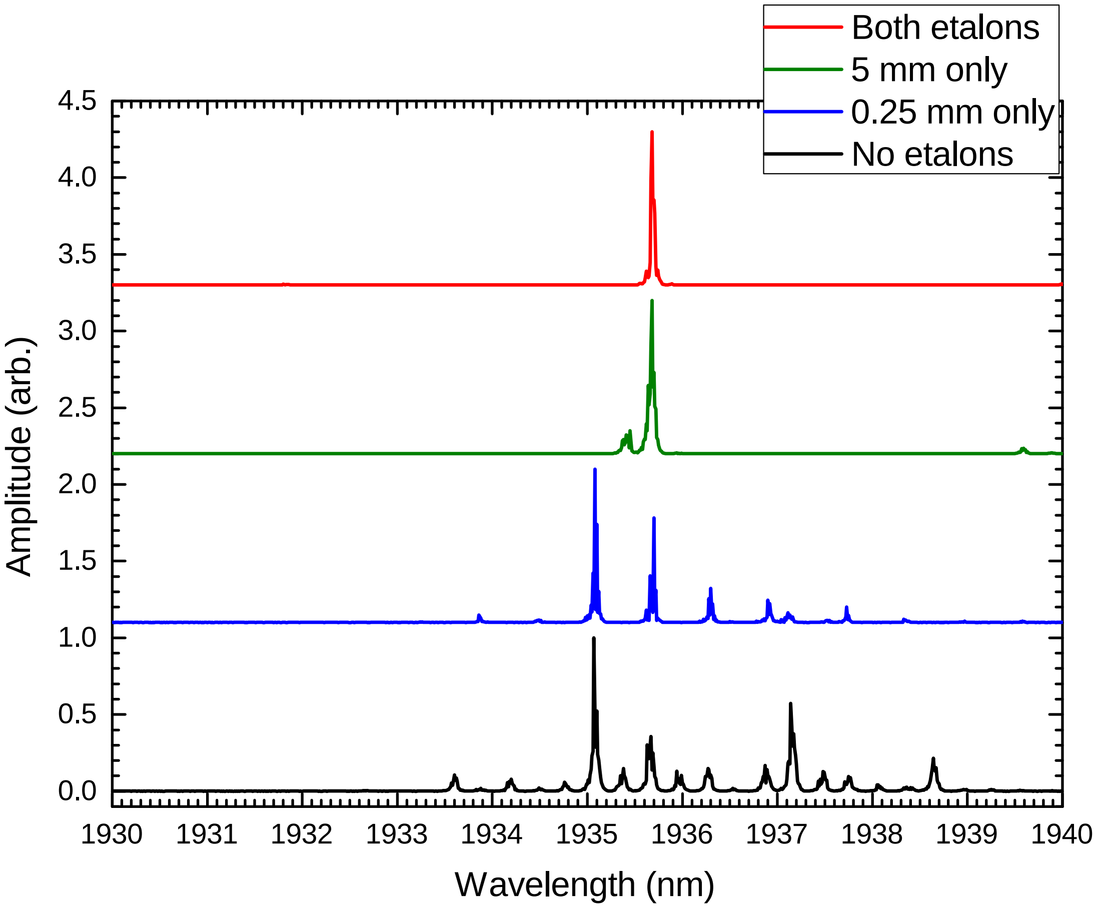

Figure 3.7: Spectra of the Q-switched laser for different etalon combinations. A single peak could only be achieved with both etalons in the cavity. The spectra have been offset for clarity.

Table 3.1: Mean, standard deviation and percentage jitter values for each pulse parameter as etalons are added to the cavity. All data taken at a repetition rate of 250 Hz and 4.9 W incident pump power with the 5 % output coupler.

| Etalon(s) | Build-up time | | | Pulse duration | | | Peak power | | | Pulse energy | | |
|---|---|---|---|---|---|---|---|---|---|---|---|---|
| | $\mu_{\tau_\mathrm{b}}$ (ns) | $3\sigma_{\tau_\mathrm{b}}$ (ns) | $\Delta\tau_\mathrm{b}$ (%) | $\mu_{\tau_\mathrm{p}}$ (ns) | $3\sigma_{\tau_\mathrm{p}}$ (ns) | $\Delta\tau_\mathrm{p}$ (%) | $\mu_{P_\mathrm{p}}$ (kW) | $3\sigma_{P_\mathrm{p}}$ (kW) | $\Delta P_\mathrm{p}$ (%) | $\mu_{E_\mathrm{p}}$ (mJ) | $3\sigma_{E_\mathrm{p}}$ (µJ) | $\Delta E_\mathrm{p}$ (%) |
| None | 220 | 5.5 | 2.5 | 34 | 0.45 | 1.3 | 24 | 0.79 | 3.2 | 1.0 | 29 | 2.8 |
| 5 mm | 240 | 11 | 4.5 | 35 | 1.8 | 5.1 | 21 | 2.4 | 11 | 0.90 | 83 | 9.3 |
| 0.25 mm | 240 | 10 | 4.2 | 35 | 1.1 | 3.1 | 19 | 1.1 | 6.0 | 0.80 | 37 | 4.6 |
| Both | 270 | 17 | 6.4 | 36 | 1.8 | 4.9 | 14 | 1.6 | 11 | 0.66 | 59 | 9.1 |

fluctuations get worse as the number of oscillating modes approaches two and the most effective method of removing this noise is by forcing the laser to oscillate on a single longitudinal and transverse mode [102]. It is thought that a similar effect is observed in the Q-switched case; with no etalons in the cavity, the laser oscillates on many modes with minimal mode beating effects (as the total power is shared between many modes, fluctuations are averaged out). With both etalons in the cavity, the laser is restricted to oscillate on less modes and therefore exhibits less averaging out of the effects of mode competition leading to increased jitter. It is believed that as the number of modes is decreased towards two, the jitter gets worse (in a similar way to CW oscillation on two modes produces the greatest fluctuations); if, however, single-frequency operation could be enforced, jitter will be reduced.

In order to investigate the link between jitter and mode competition, a Fabry-Perot interferometer (FPI) was used to observe the number of modes the laser oscillates on. The FPI has a free spectral range (FSR) of 10 GHz, corresponding to the width of the single peak seen on the OSA when using both etalons (figure 3.7), and was driven by a sawtooth ramp signal with amplitude 30V and frequency 100 mHz by a Thorlabs control box (SA201). The pulsed nature of the laser is problematic for the FPI as the interefogram is not acquired instantaneously but as a function of scanned mirror position. Therefore, additional instrumentation must be used to yield a 'dc' type output from the FPI.

The pulsed nature of the laser (and therefore the electrical signal from the detector in the FPI) needed to be accounted for in order to obtain continuous fringes from the FPI. This was achieved using a bespoke, ultra-high bandwidth boxcar integrator. This device, triggered by a TTL phase-locked to the pulse train, integrated the signal generated by the detector within a certain temporal window around the pulse, then fed this analogue signal into a sample-and-hold circuit in order to produce an indefinite dc voltage proportional to the energy of the pulse incident on the detector. The boxcar was triggered by a mono-stable oscillator itself triggered by the master signal generator controlling the repetition rate of the laser. The electronic signals within the boxcar are shown in figure 3.8a.

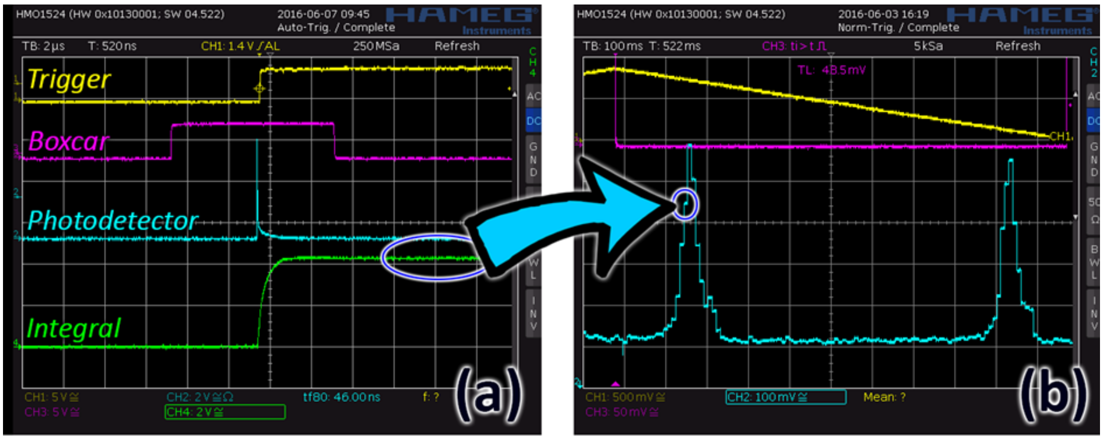

Figure 3.8: Boxcar instrumentation signals and the acquisition of the interferogram. Each pulse of the laser results in a sequence as shown in (a). The fringes shown in (b) are made up of many such pulses

The quasi-dc signal from the boxcar integrator was then measured as a function of interferometer ramp voltage in order to acquire the interferogram, as shown in figure 3.8b (where the measurement has deliberately been done to show the discrete levels within the fringe). Note that this is acquired completely asynchronously to the laser repetition rate, and so as the difference between the laser repetition rate and the ramp frequency increases, more measurement points per fringe are obtained – and so a smoother curve. Therefore, there is no multi-pulse averaging in the system but each fringe is built up from many individual pulses. In figure 3.8b, the interferogram has been acquired from a commercial laser operating at a repetition rate of 100 Hz and ramp frequency of 400 mHz. The fringe width is approximately 1 oscilloscope division wide and, as the timebase is 100 ms, the fringe is composed of 10 visible discreet measurements – each one corresponding to an integrated optical pulse. In the experiments presented in this chapter, the laser was operated at a repetition rate of 250 Hz and the ramp frequency was 100 mHz; giving much smoother fringes than those shown in figure 3.8b.

By rotating the etalons, it was possible to observe the laser oscillating on different numbers of modes (see figure 3.9) while maintaining a single peak on the OSA. It is important that only one peak is observable on the OSA or the modes seen on the Fabry-Perot trace may not be from adjacent modes, even if they appear to be, due to overlapping of the FSR. As can be seen in figure 3.9, the laser could be made to oscillate on 2, 3 and 4 adjacent modes. Adjacency was confirmed by comparing the mode spacing inferred from the traces (550 MHz, 530 MHz and 540 MHz on average for 4, 3 and 2 modes respectively) to the FSR of the cavity (calculated to be $\sim 600$ MHz), the discrepancy is due to inaccuracies in measuring the cavity length. Sustained oscillation on a single mode or on more than 4 adjacent modes was not observed. It is important to remember that the Fabry-Perot traces are built up over many pulses, and therefore when, for example, three modes are detected, it is not possible to distinguish the cases of every single pulse containing these three modes, or of each pulse being single mode but hopping between modes on a pulse-to-pulse basis. It is not currently possible to measure the spectrum or mode content of a single pulse.

For each case in figure 3.9, the jitter was measured twice (non-consecutively) with the laser again operating at a repetition rate of 250 Hz, incident pump power of 4.9 W and the 5 % output coupler. The results are shown in table 3.2. The results show some evidence for jitter getting worse as the number of modes decreases but it is not conclusive; more data points are needed to confirm the trend. There is an increase in build-up time jitter (averaging over the runs) of $\sim 2.5$ ns going from 4 to 3 modes, but this jitter then decreases when operating on 2 modes. The percentage jitter in the energy does increase overall when going from 4 (6.3 % and 3.8 %) to 2 modes (7.6 % and 2.4 %). It should be noted that the difference in jitter values (both $3\sigma$ and percentage) vary more between runs than between different numbers of modes. This could indicate an environmental contribution to the jitter as the different runs were taken non-consecutively over several days.

It is thought that, if better mode selectivity could be attained, single-frequency operation would improve the jitter. In order to better judge how to attain better selectivity, it is useful to analyse what parameters can affect the power in each mode. From this, the values of these parameters required to achieve a level of mode suppression that is consistent with single-mode operation will be found. Equation 3.4 gives an expression for the expected relative strengths of two modes [63] where, $P_{\mathrm{a}}$ is the power in mode a, $\sigma_{\mathrm{a}}$ is the stimulated emission cross-section at the wavelength of mode a and

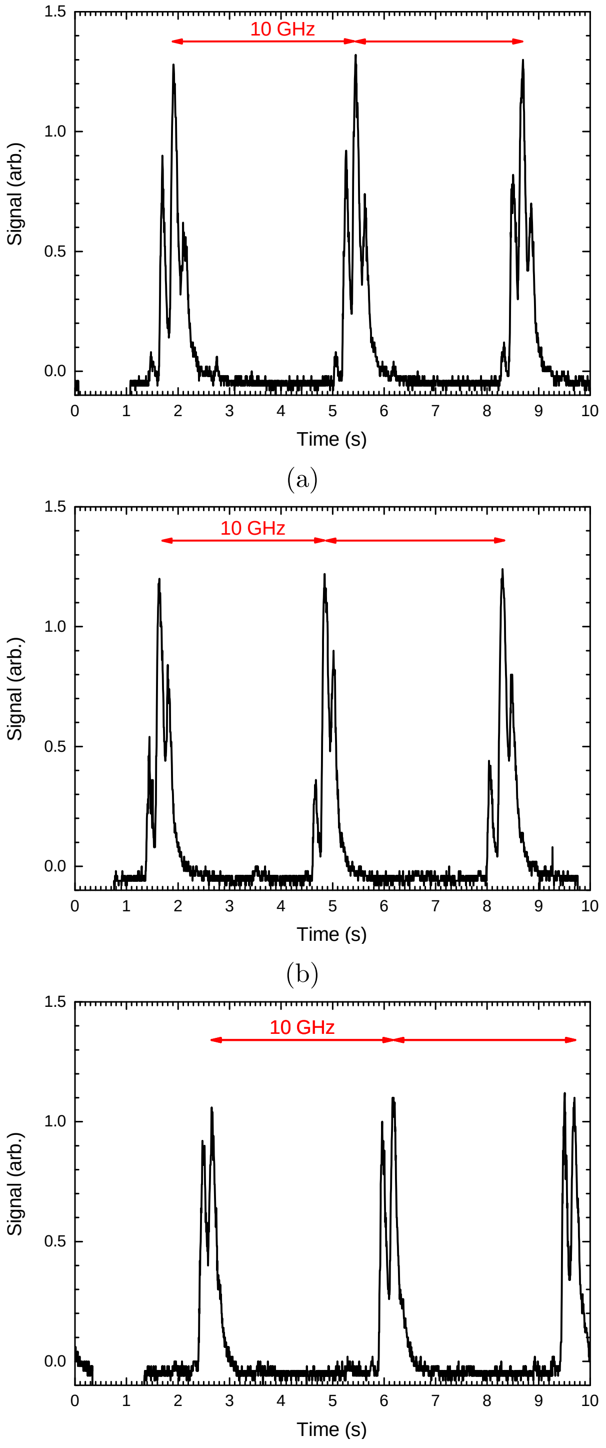

(a)

(b)

(c)

Figure 3.9: Outputs from Fabry-Perot interferometer and boxcar integrator showing laser action on (a) 4 modes (average mode spacing 550 MHz), (b) 3 modes (average mode spacing 530 MHz) and (c) 2 modes (average mode spacing 540 MHz).

Table 3.2: Mean, standard deviation and percentage jitter in each pulse parameter when the laser oscillates on a different number of adjacent modes. All data taken at a repetition rate of 250 Hz and 4.9 W incident pump power with the 5 % output coupler.

| Number of modes | Build-up time | | | Pulse duration | | | Peak power | | | Pulse energy | | |
|---|---|---|---|---|---|---|---|---|---|---|---|---|
| | $\mu_{\tau_\mathrm{b}}$ (ns) | $3\sigma_{\tau_\mathrm{b}}$ (ns) | $\Delta\tau_\mathrm{b}$ (%) | $\mu_{\tau_\mathrm{p}}$ (ns) | $3\sigma_{\tau_\mathrm{p}}$ (ns) | $\Delta\tau_\mathrm{p}$ (%) | $\mu_{P_\mathrm{p}}$ (kW) | $3\sigma_{P_\mathrm{p}}$ (kW) | $\Delta P_\mathrm{p}$ (%) | $\mu_{E_\mathrm{p}}$ (mJ) | $3\sigma_{E_\mathrm{p}}$ (µJ) | $\Delta E_\mathrm{p}$ (%) |
| 4 | 260 | 16 | 6.2 | 44 | 1.1 | 2.5 | 12 | 1.1 | 9.1 | 0.74 | 47 | 6.3 |
| | 270 | 18 | 6.6 | 46 | 1.4 | 3.1 | 10 | 0.66 | 6.7 | 0.76 | 29 | 3.8 |
| 3 | 260 | 19 | 7.0 | 45 | 1.1 | 2.4 | 11 | 0.44 | 4.0 | 0.77 | 17 | 2.2 |
| | 270 | 20 | 7.4 | 45 | 1.4 | 3.2 | 12 | 0.93 | 7.8 | 0.77 | 37 | 4.8 |
| 2 | 230 | 17 | 7.2 | 42 | 1.0 | 2.5 | 19 | 1.2 | 6.5 | 0.86 | 66 | 7.6 |
| | 250 | 18 | 7.2 | 45 | 0.84 | 1.9 | 12 | 0.43 | 3.5 | 0.84 | 20 | 2.4 |

$N_0$ is the population inversion at the time of switching. $l$ is the crystal length, $R_\mathrm{a}$ is the output coupler reflectivity at the wavelength of mode a, $L_\mathrm{a}$ is the loss term for mode a and $q$ is the number of round-trips. Due to the small mode spacing (around 590 MHz) in the Tm:YAP laser, it is assumed that the stimulated emission cross-section and output coupling are the same for adjacent modes. Therefore, the only terms that will affect the relative strengths of the two modes are the losses (with the difference provided by the etalons) and the number of round-trips.

$$\frac{P_\mathrm{n}}{P_\mathrm{m}} = \left(\frac{\mathrm{e}^{2\sigma_\mathrm{n}N_0 l}R_\mathrm{n}L_\mathrm{n}}{\mathrm{e}^{2\sigma_\mathrm{m}N_0 l}R_\mathrm{m}L_\mathrm{m}}\right)^q \tag{3.4}$$

For a factor of 10 suppression (factor chosen due to its use in [63]) of mode m relative to mode n, the number of round trips required for a given loss differentiation is given by equation 3.5. From the MATLAB script described in section 3.1.1, it was found that the loss ratio between adjacent modes is $L_\mathrm{n}/L_\mathrm{m} \sim 1.005$. This means that around 462 round-trips are required during the build-up of the pulse which would take approximately 1 µs; however, the actual build-up time of the pulses is 270 ns (average for 4 mode data presented above). Therefore, two options are available: increase the loss ratio or increase the build-up time. Since the loss ratio cannot be increased as coatings cannot be risked on the etalons (for reasons discussed in section 3.1.1), a method of increasing the build-up time is needed to allow the mode selection to happen. One caveat to increasing the build-up time is that the method used should not change parameters such as the cavity length, output coupling and gain due to the knock-on effect on the pulse properties.

$$q = \frac{\log(10)}{\log(\frac{L_{\mathrm{n}}}{L_{\mathrm{m}}})} \tag{3.5}$$

The pre-lase technique discussed in section 1.4.4.2 is a modification of the standard Q-switching technique used so far that allows a long build-up time without changing the cavity. This is achieved by decreasing the cavity losses to a point that allows only very-high-threshold laser oscillation on a single mode. The build-up time of this high-loss mode will be long compared to build-up times presented so far. Once this single-mode has built up, the cavity is switched to the low-loss state and the single-mode out-competes all others to produce a single-frequency pulse. The results of using pre-lase will be discussed in chapter 5.

## 3.2 Transverse mode control

Having looked at the effect of longitudinal mode control on the jitter, this section will discuss the investigation into transverse mode control.

Using the model of the cavity in LaserCanvas (see section 2.1), the smallest accessible (in air) beam radius was found to be approximately 150 µm and occurred between the crystal and the diverging lens. A pinhole with diameter 400 µm was placed as shown in figure 3.10 and the output average power optimised. The pinhole diameter was chosen as it will allow the expected $\mathrm{TEM}_{00}$ mode size to pass but present a large loss to higher order modes.

2500 consecutive pulses were recorded with and without the pinhole twice (non-consecutively). The jitter results are shown in table 3.3. As can be seen from the table, the standard deviations of the parameters are similar with and without the pinhole. Averaging over the two runs, the build-up time standard deviation ($3\sigma$ value) is 2.5 ns and 2.8 ns with and without the pinhole respectively. This indicates that the transverse

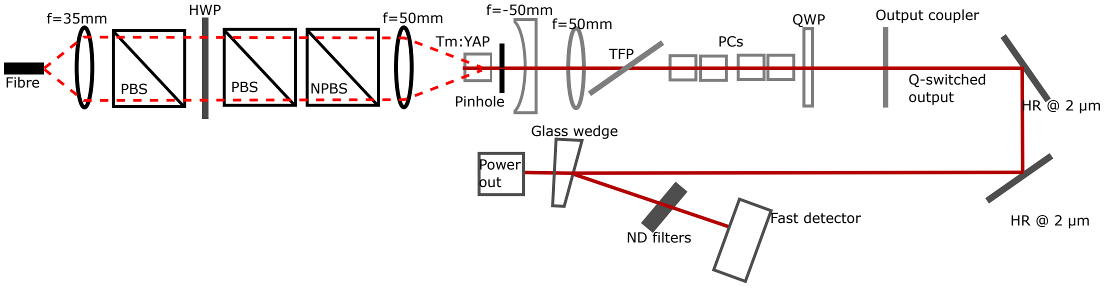

Figure 3.10: Cavity diagram showing pinhole position used while testing the effect of transverse mode control on the jitter.

Table 3.3: Mean, standard deviation and percentage jitter in each pulse parameter with and without the pinhole in the cavity. All data taken at a repetition rate of 250 Hz and 4.9 W incident pump power with the 5 % output coupler.

| Pinhole | Build-up time | | | Pulse duration | | | Peak power | | | Pulse energy | | |
|---|---|---|---|---|---|---|---|---|---|---|---|---|
| | $\mu_{\tau_\mathrm{b}}$ (ns) | $3\sigma_{\tau_\mathrm{b}}$ (ns) | $\Delta\tau_\mathrm{b}$ (%) | $\mu_{\tau_\mathrm{p}}$ (ns) | $3\sigma_{\tau_\mathrm{p}}$ (ns) | $\Delta\tau_\mathrm{p}$ (%) | $\mu_{P_\mathrm{p}}$ (kW) | $3\sigma_{P_\mathrm{p}}$ (kW) | $\Delta P_\mathrm{p}$ (%) | $\mu_{E_\mathrm{p}}$ (mJ) | $3\sigma_{E_\mathrm{p}}$ (µJ) | $\Delta E_\mathrm{p}$ (%) |
| 400 µm | 150 | 2.3 | 1.5 | 38 | 0.27 | 0.72 | 7.1 | 0.14 | 2.0 | 0.43 | 6.3 | 1.5 |
| | 150 | 2.7 | 1.8 | 38 | 0.29 | 0.77 | 7.7 | 0.24 | 3.1 | 0.47 | 9.4 | 2.0 |
| none | 130 | 2.2 | 1.7 | 39 | 0.31 | 0.8 | 9.0 | 0.24 | 2.7 | 0.54 | 10 | 1.9 |
| | 140 | 3.3 | 2.4 | 39 | 0.41 | 1.1 | 8.2 | 0.30 | 3.7 | 0.51 | 12 | 2.4 |

mode control has had a minimal effect; indeed, the laser may have been operating solely on the TEM$_{00}$ mode without the pinhole. Recall that the target level of build-up time jitter is $3\sigma < 1$ ns and so some other method must provide an improvement to this level. The main effect of the pinhole was to increase the mean build-up time (135 ns – 150 ns) and reduce the mean peak power (8.6 kW – 7.4 kW) and pulse energy (0.53 mJ – 0.45 mJ), this is expected as the pinhole introduces more loss to the cavity which will adversely affect these parameters. However, it is interesting to note that the jitter in the pulse energy is below the target of 3 % for all case presented in table 3.3; it is unknown why this occurred, although it is probable that the lab conditions were just particularly favourable during these measurements. The effect of controlling the laboratory environment will be investigated in chapter 4.

## 3.3 Conclusions

In summary, etalons were used to limit the mode content of the laser. An increase in jitter was observed when two etalons were included in the cavity compared to the free-running laser. This is thought to be due to increased mode competition affecting the pulse. In an attempt to explore this further, a Fabry-Perot interferometer and boxcar integrator were used to monitor the number of modes the laser was oscillating on. The jitter was measured with the laser oscillating on 2, 3 and 4 adjacent modes. A $\sim 2.5\,\mathrm{ns}$ increase in build-up time jitter was observed between 4 and 3 mode operation, the pulse energy percentage jitter also increased from 6.3 % and 3.8 % for 4 modes to 7.6 % and 2.4 % for 2 mode operation. This constitutes some evidence that reducing the mode content increases the jitter; however, it was not possible to force the laser to oscillate on more than four adjacent modes which would have helped confirm this hypothesis.

The main effect of including a pinhole in the cavity to control the transverse mode content was to increase the mean build-up time (from $\sim 140\,\mathrm{ns}$ to 150 ns) and decrease the output power (from $\sim 8.6\,\mathrm{kW}$ to $\sim 7.4\,\mathrm{kW}$) and pulse energy (from $\sim 0.53\,\mathrm{mJ}$ to $\sim 0.45\,\mathrm{mJ}$). These effects are expected as the pinhole presents an additional loss to the beam. There was minimal effect on the jitter; build-up time jitter decreased by $< 0.3\,\mathrm{ns}$ which is below the resolution used to record the data and the jitter was above the target level of $3\sigma < 1\,\mathrm{ns}$ in both cases. Jitter in the pulse energy was below the target of 3 % both with and without the pinhole (1.8 % and 2.2 % respectively).

The key conclusion of this chapter is that mode control, both longitudinal and transverse, does not significantly improve the jitter (at least for longitudinal mode numbers of two or more). The implications of this are two-fold: techniques to enforce single frequency operation need to be investigated; and that other potential means of reducing jitter, such as improving the mechanical stability and reducing atmospheric absorption, need to be considered.

Chapter 4 will describe attempts to reduce the jitter by improving the mechanical stability of the system and reducing atmospheric water absorption.

# Chapter 4

# Ruggedised System

After completing the benchmark data set, it was decided to reduce the effect of mechanical vibrations by moving from the breadboard system to a more rugged housing. It was believed that, as a vibration affecting cavity alignment constitutes a time-varying loss, increasing the mechanical stability of the laser would improve the jitter. The design evolved to allow the desiccation of the air inside the cavity to reduce the strong atmospheric water absorption at wavelengths around 1.94 µm; figure 4.1 shows the difference in transmission over one cavity round-trip ($\sim 450$ mm) between atmospheres at 33 % and 5 % relative humidity. It was thought that reducing the water content of the air in the cavity would lead to increased output power and energy (due to lower losses); as well as a reduction in jitter due to reduced random absorption of laser photons during the build-up phase. Searches suggest there is very little in the literature on the effect of mechanical stability or atmospheric absorption on laser stability. Based on the above thinking, the objectives of the ruggedised system were to:

1. Improve the mechanical stability by removing degrees of freedom in the optomechanical components.
2. Remove the effect of atmospheric water absorption by desiccating the air inside the cavity.

Section 4.1 details the design of the ruggedised system and section 4.2 presents the results of implementing the system. Specifically, section 4.2.1 describes the effects

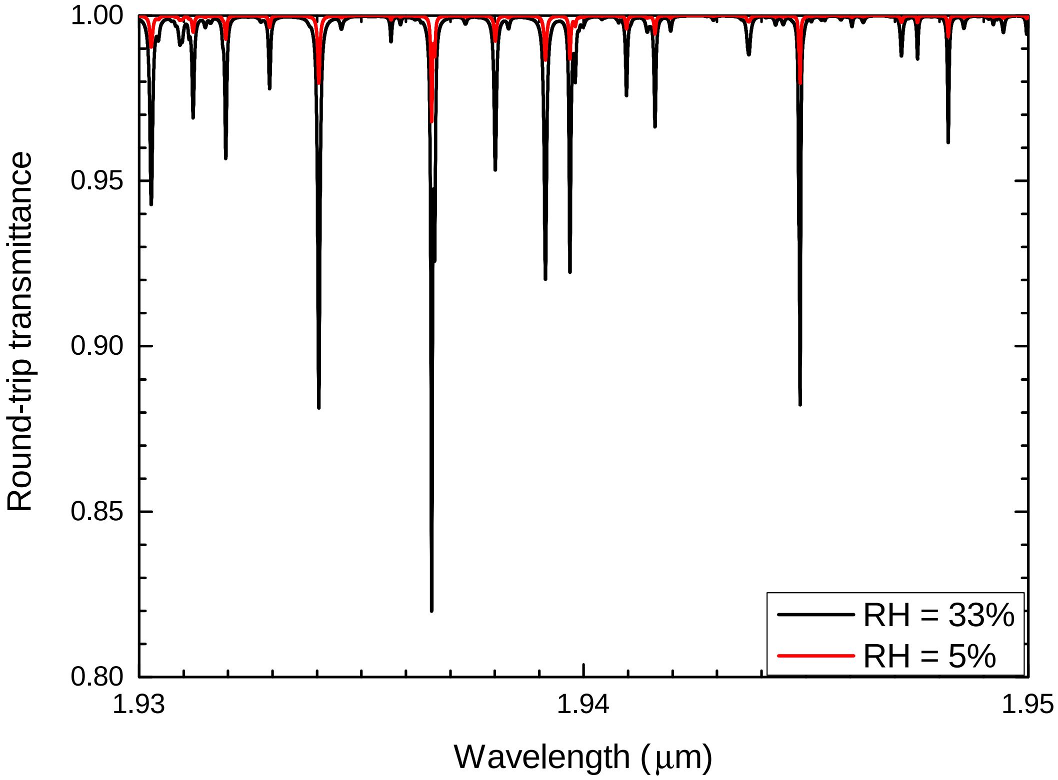

Figure 4.1: Atmospheric transmission about the laser wavelength over a distance of one cavity round trip at relative humidity values of 33 % and 5 %. Data from [103]

on the jitter of the increased mechanical stability, section 4.2.2 presents the results of desiccating the ruggedised cavity and section 4.2.3 details the results of purging the cavity with dry compressed air. Section 4.2.4 describes the effect of the combination of the ruggedised system, purged cavity and etalons for mode control. Section 4.3 summarises the conclusions drawn from this work.

## 4.1 Design

The full ruggedised system is shown in figure 4.2. In order to be able to remove water from the cavity, it is necessary to isolate the cavity from the laboratory environment as best as possible. To that end, the cavity section was milled out from a single block with the lid sealing on top with an o-ring. O-rings are also used to improve sealing around the windows at either end (one AR coated for the pump light and two AR coated at the laser wavelength - one for Q-switched output and one for cavity-dumped output). Electrical power for the Pockels cells, crystal cooling and humidity sensor (see section 4.2.2) is routed through panel-mounted connections on the box wall which are sealed with o-rings. In this way, pathways for air exchange between the cavity and the laboratory should be minimised.

In order to minimise the effects of mechanical vibrations, all optics are mounted with the minimum degrees of freedom for alignment. The key adjustments that were kept include rotation of the thin-film polariser to align it at Brewster's angle to the cavity mode. It is also necessary to be able to align the cavity mode for best overlap with the pump beam in the crystal. Therefore, the end mirrors (one of which is coated on the crystal) need to be manipulable. However, translational degrees of freedom perpendicular to the beam axis can be removed by designing mounts to fix all optics centred on the beam. The output coupler was held in a Thorlabs Polaris mount which is designed for long-term alignment stability. Water cooling of the crystal was abandoned in favour of TEC cooling due to circulating water introducing vibrations to the system. In order to get the heat out while keeping the rotational degree of freedom of the crystal mount, a heat pipe is used to transfer heat from the hot side of the TEC to an aluminium block that is bolted to the base. A heat pipe is a small tube (made of copper in this case) containing a wick structure and a small amount of fluid (water here) at the saturated state [104]. The pipe is comprised of three sections: the evaporator section at one end, where heat is absorbed and the fluid vaporises; a condenser section at the opposite end, where the fluid condenses and heat is extracted; and an adiabatic section in between that allows the gas and liquid phases to flow in opposite directions to complete the cycle [104]. For a more complete description of heat pipes, see reference [104]; and [105] for a mathematical description of the heat transfer process. The heat pipe terminates in an aluminium block clamped to the cavity box base, forming a large heat sink. All interfaces between the crystal and the base are coated liberally with heat sink grease apart from the crystal itself which is wrapped in indium foil. Other than these changes to the mounting of optics, the cavity remained the same as those shown in figure 3.6a when the etalons were included and figure 2.2a when they were not.

As the design was made to allow desiccation (and later purging) of the cavity, the pump attenuator was placed on a separate base block outside the cavity. This allows manipulation of the pump power without having to constantly remove the lid and re-desiccate the cavity. The inlet and outlet for the air flow associated with the desiccation/purging are located on opposite ends of the cavity (one at the pump end and one at the output) and at different heights.

## 4.2 Testing results

This section will present the results of experiments investigating the effect of the ruggedised system on the jitter. In section 4.2.1, the effect of the new optomechanical components on its own is detailed. Section 4.2.2 looks at the combined effect of the ruggedised system and desiccating the cavity. Section 4.2.3 investigates the effect of combining the ruggedised system with purging the cavity with compressed air. Finally, section 4.2.4 details the effect of combining the ruggedised system, purging the cavity and using etalons to control the mode content of the laser (as in chapter 3). This order of testing was chosen to allow evaluation of the effect of each improvement individually on the jitter.

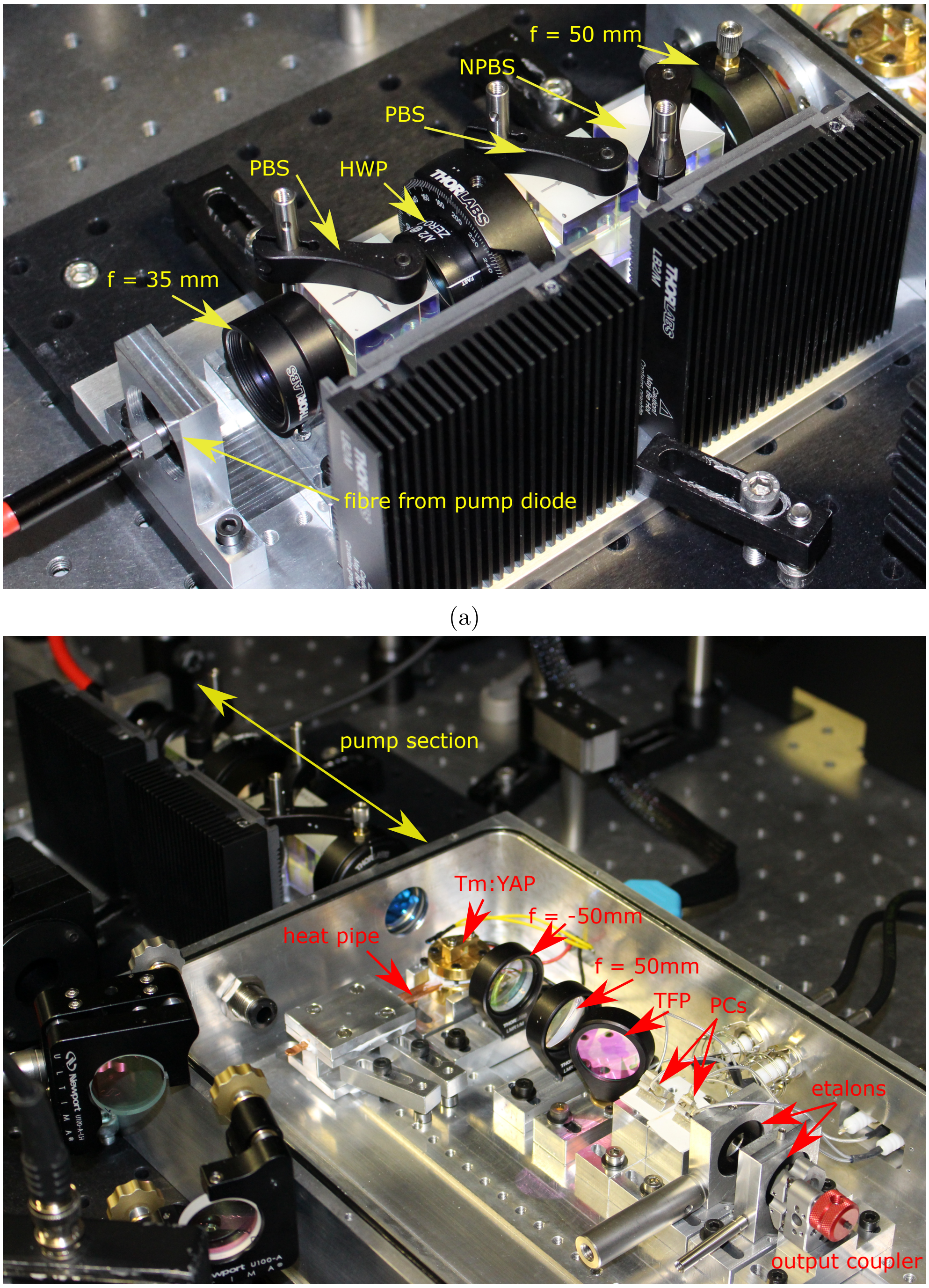

(a)

(b)

Figure 4.2: Photos of the ruggedised system. (a) pump section, PBS = polarising beam-splitter, NPBS = non-polarising beam-splitter, HWP = half-wave plate. (b) cavity section, TFP = thin-film polariser, PCs = Pockels cells. Optic spacings are the same as given in figure 3.6a with the etalons in the cavity and figure 2.2a without.

### 4.2.1 Effect of ruggedisation

As previously mentioned, the improved ruggedness of the cavity should reduce the effects of vibrations on components, thereby reducing the time-dependent loss due to optics passing in to and out of alignment which should reduce the jitter. In order to evaluate the effect of the ruggedisation on the jitter, data was taken and analysed as detailed in section 2.3 and the results of this analysis will be directly compared to those obtained in that section from the less rugged breadboard system. The system was evaluated with the 5 % output coupler and operated at a repetition rate of 250 Hz with an incident pump power of 4.9 W as in previous chapters and explained in chapter 2.6. Although the CW threshold pump power was not measured, it can be assumed to be similar to or less than that for the breadboard system (1.9 W) and a rough estimate of the over-pumping ratio would be 2.6 as before (see section 1.4.4.1 for an explanation of why this is only rough). Table 4.1 shows the average (rounded to two significant figures) of the two measurements taken during chapter 2 (on the breadboard system) as well as the results from testing the ruggedised system. As can be seen, there is a significant reduction in jitter for all parameters – build-up time jitter ($3\sigma$ value) has been reduced from 5.6 ns to 1.8 ns. This is a significant improvement; however, recall that the target for this parameter is $3\sigma_{\tau_\mathrm{b}} < 1\,\mathrm{ns}$, so further improvement is necessary. The jitter in the pulse energy has been improved from 6.9 % to 2.6 %, below the target level of $\Delta E_\mathrm{p} < 3\,\%$. There has also been a reduction in the jitter in duration and peak power; 4.0 ns to 0.75 ns and 3.9 kW to 0.43 kW respectively.

Having made improvements in controlling the loss due to mechanical ruggedness, the next step was to control any time-varying losses due to the laboratory environment. The most obvious source of loss is atmospheric water absorption (as explained above and in figure 4.1); the first attempt to address this was through the desiccation of the cavity.

### 4.2.2 Effect of desiccation

To test the performance of desiccation, a humidity sensor (Honeywell HIH-5031) was inserted in to the cavity and the system was connected to a Thorlabs Pure Air Circulator

Table 4.1: Mean, standard deviation and percentage jitter in each pulse parameter for the breadboard system as recorded in table 3.1 and the ruggedised system described here. All data taken at a repetition rate of 250 Hz and 4.9 W incident pump power with the 5 % output coupler.

| Case | Build-up time | | | Pulse duration | | | Peak power | | | Pulse energy | | |
|---|---|---|---|---|---|---|---|---|---|---|---|---|
| | $\mu_{\tau_\mathrm{b}}$ (ns) | $3\sigma_{\tau_\mathrm{b}}$ (ns) | $\Delta\tau_\mathrm{b}$ (%) | $\mu_{\tau_\mathrm{p}}$ (ns) | $3\sigma_{\tau_\mathrm{p}}$ (ns) | $\Delta\tau_\mathrm{p}$ (%) | $\mu_{P_\mathrm{p}}$ (kW) | $3\sigma_{P_\mathrm{p}}$ (kW) | $\Delta P_\mathrm{p}$ (%) | $\mu_{E_\mathrm{p}}$ (mJ) | $3\sigma_{E_\mathrm{p}}$ (µJ) | $\Delta E_\mathrm{p}$ (%) |
| Breadboard | 210 | 5.6 | 2.8 | 32 | 4.0 | 13 | 20 | 3.9 | 20 | 0.70 | 48 | 6.9 |
| Ruggedised | 170 | 1.8 | 1.1 | 38 | 0.75 | 2.0 | 11 | 0.43 | 3.8 | 0.65 | 17 | 2.6 |

Unit (PACU). The PACU pumps the air through a desiccant, particulate filters and a molecular sieve allowing it to remove moisture, particulates and volatile organic compounds (although only the first of these is of particular interest here). The PACU is designed to work in a closed loop and so the ruggedised system was sealed as best as possible with a silicone adhesive sealant after discovering that the o-rings were not enough. The lack of a seal around the o-rings was discovered by feeling the air flow on a hand near it while the PACU was operating. According to the website, the PACU is capable of desiccating a 3 L volume to $\sim 2\,\%$ relative humidity; the volume of the ruggedised cavity is $\sim 4.5$ L, therefore the target humidity level will initially be 5 %. The ambient humidity in the laboratory was typically $> 20\,\%$ and was not constant day-to-day (relative humidity values of 20 % – 60 % were observed).

Running the PACU, monitoring the relative humidity and recording jitter data every 2 minutes as the humidity decreased produced the data seen in figure 4.3. Data collection took 10 seconds and it was assumed that the humidity was constant over the measurement time based on observations of the rate of change of voltage output from the humidity sensor. As can be seen, reducing the humidity to around 13 % (from $\sim 20\,\%$) had little effect on the jitter; the percentage jitter in pulse duration, peak power and pulse energy are reduced by ~1 %, 0.8 % and 0.4 % respectively over the first 1.8 % drop in humidity but then stayed constant with reducing humidity. The build-up time jitter is unaffected by the changing humidity. The energy jitter is better than the target ($\Delta E_\mathrm{p} < 3\,\%$) across the humidity range observed.

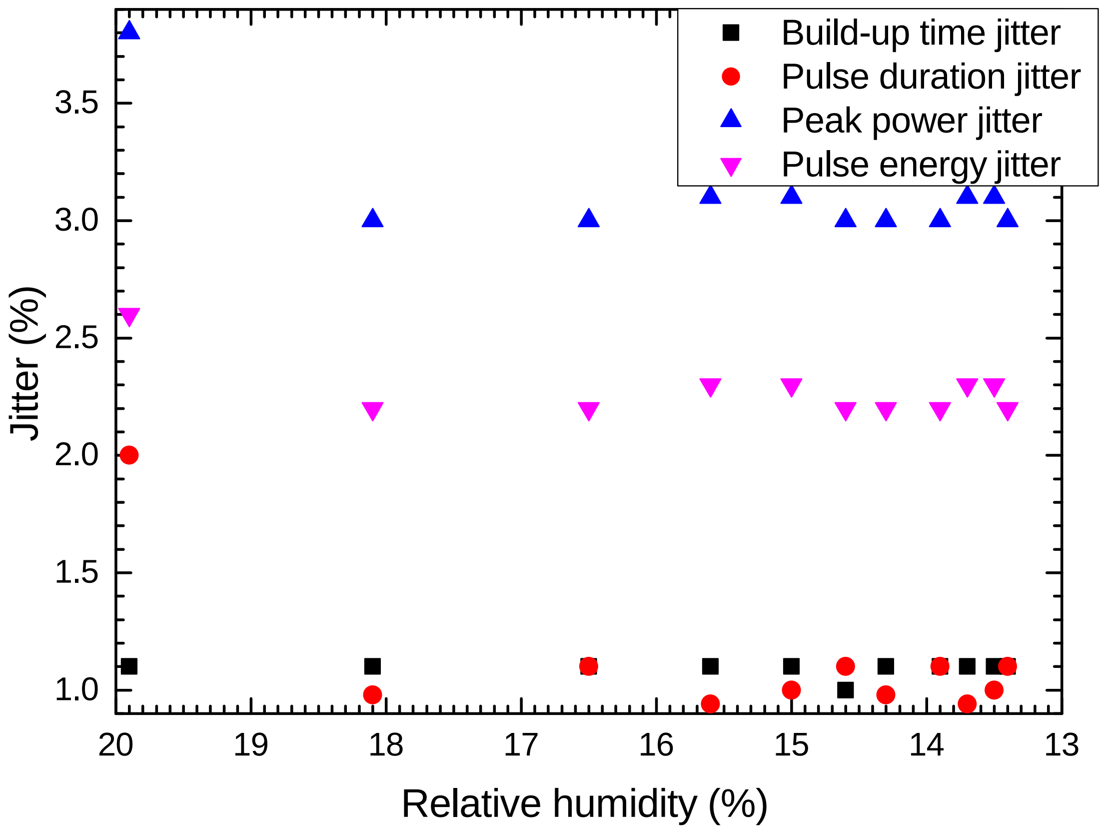

Figure 4.3: Percentage jitter in each parameter as the cavity is desiccated over 20 minutes.

Looking at the mean values and standard deviations of each parameter, shown in figure 4.4, more information can be gleaned. First, the reduced humidity led to an increase in the mean peak power and pulse energy of roughly 0.4 kW and 22 µJ respectively; this is expected as lower humidity means less loss due to absorption. Also the mean build-up time decreases by around 6 ns, further implying that the losses have indeed decreased. The mean pulse duration also decreases; however a difference of <0.1 ns is under the resolution of the measurements taken (0.5 ns). The standard deviation ($3\sigma$ value) of the build-up time follows no clear pattern with respect to the relative humidity; however, the standard deviation of the duration decreases from $\sim$ 1.5 times the measurement resolution to sub-resolution (decreasing from 0.75 ns to $\sim$ 0.38 ns). The standard deviation of the peak power decreases from 0.43 kW to around 0.35 kW and that of the pulse energy decreases from 17 µJ to $\sim$ 15 µJ. It is possible that if the relative humidity could be reduced further, a greater reduction in jitter may be seen; however, the desiccator was not able to do this. The poor performance of the desiccator is probably due to the leakiness of the housing as it is designed to work in a closed loop.

### 4.2.3 Effect of purging

As the desiccator struggled to reduce the humidity down to the target level of 5 %, it was decided to switch to purging the cavity using a positive pressure of dry air or nitrogen. A quick test showed that either gas could reduce the humidity to the target levels as shown in figure 4.5. It was decided to start with dry air from the supply in the lab in order to avoid the use of compressed gas cylinders.

Similarly to section 4.2.2, jitter data and the relative humidity were recorded every 5 minutes. The increased time between measurements is to allow the system to reach a steadier state; it can be seen in figure 4.5 that it is certainly unreasonable to assume a constant humidity over the measurement time within the first 5 minutes. Figure 4.6 shows that there is an initial improvement in jitter but after the second data point, there is little effect. Specifically, the build-up time jitter is indifferent to the humidity and remains around 1.2 %, the duration jitter drops from 2.9 % to hover about 0.82 %,

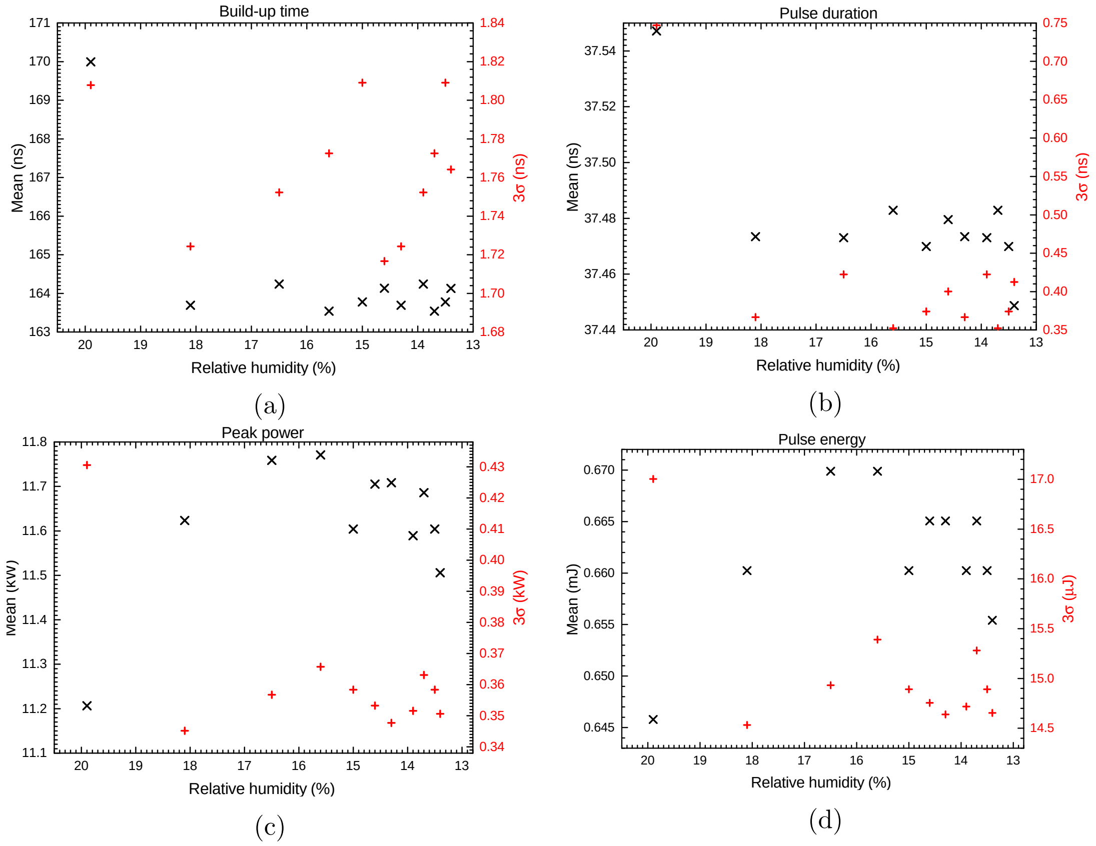

(a) (b) (c) (d)

Figure 4.4: Mean (black X) and standard deviation (red +) in (a) build-up time, (b) pulse duration, (c) peak power and (d) pulse energy against relative humidity as the cavity is desiccated over 20 minutes.

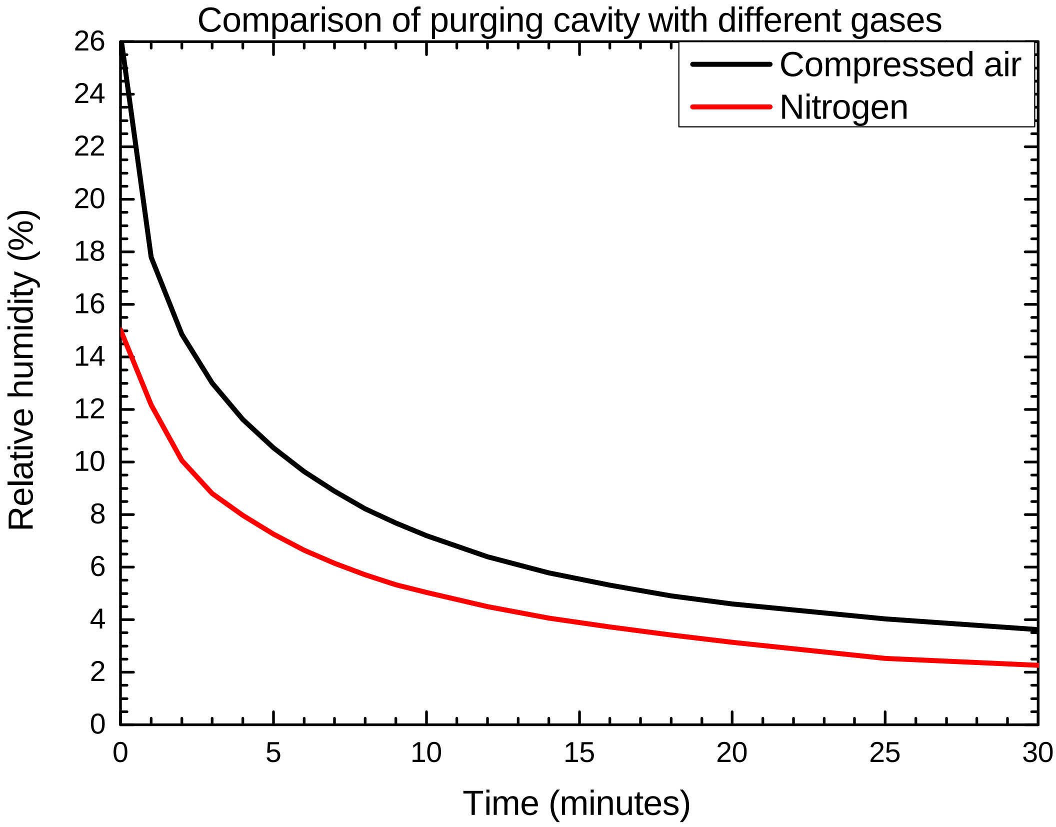

Figure 4.5: Comparison of humidity reduction by purging cavity with different gases.

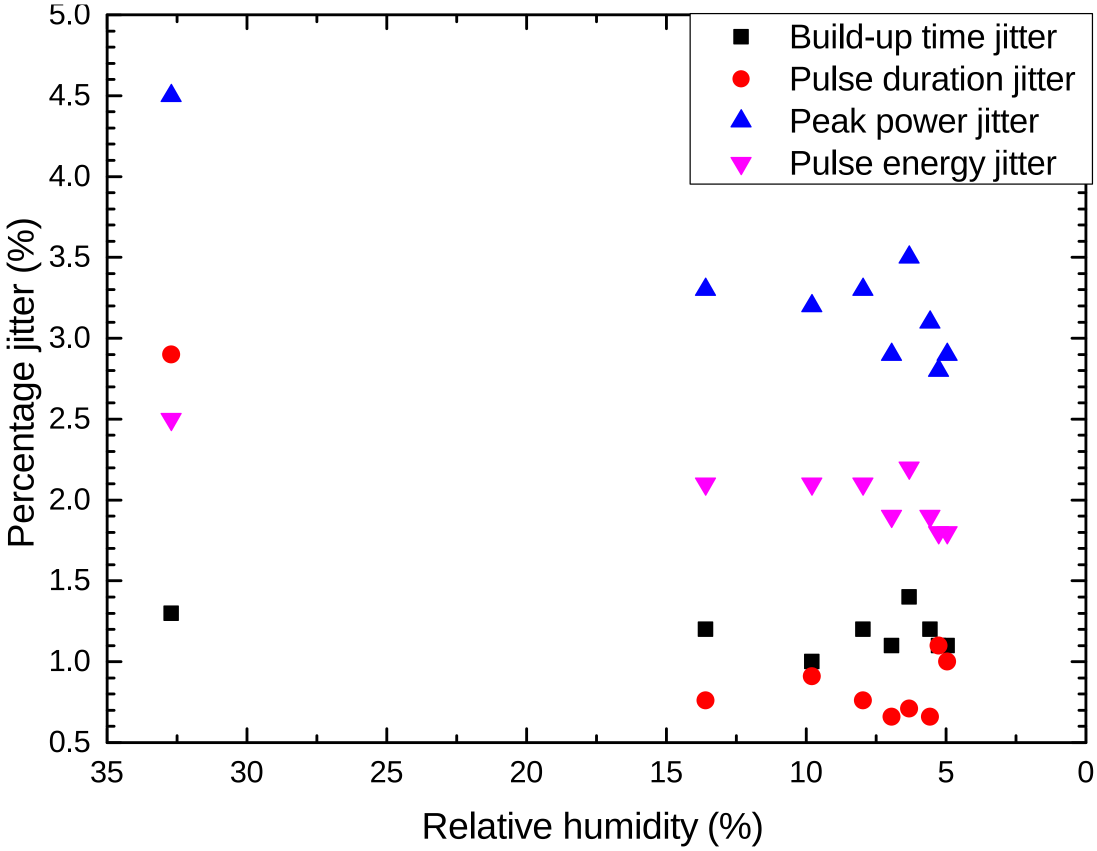

Figure 4.6: Percentage jitter in each parameter as the cavity is purged with compressed air over 40 minutes.

peak power jitter is reduced from 4.5 % to around 3.1 % and pulse energy jitter goes from 2.5 % to ∼ 2.0 % (where the final value quoted is an average of all data points after the first). This lack of continuing jitter reduction as humidity is decreased could be due to other causes of jitter becoming dominant when the humidity is reduced below 15 %.

Looking at the values of the mean and standard deviation for each parameter as the humidity is reduced (figure 4.7) shows similar results as in section 4.2.2. The mean build-up time is reduced by around 10 ns and the peak power and pulse energy are increased by ∼ 2 kW and ∼ 0.1 mJ respectively with reduced humidity (below 15 %). The increase (reduction) in mean build-up time and pulse duration (peak power and energy) starting around 7 % relative humidity is due to the onset of thermal effects after running the laser for around 40 minutes. It was observed that the crystal temper-

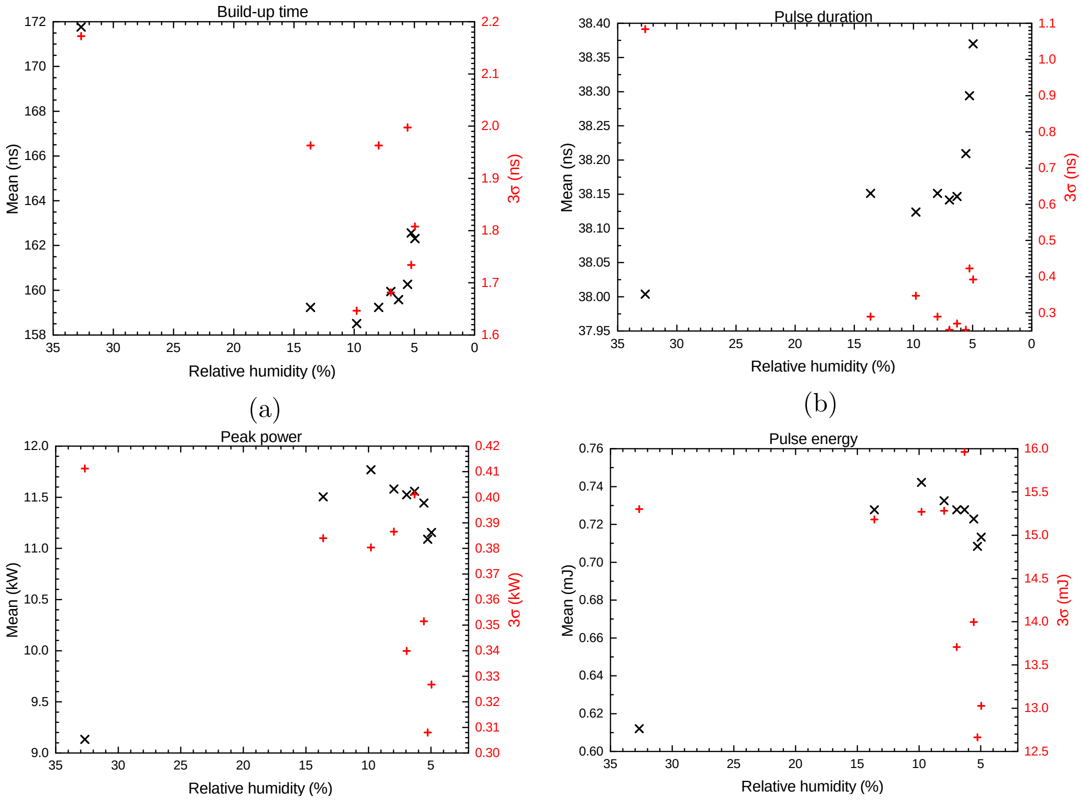

(a) (b)

(c) (d)

Figure 4.7: Mean (black X) and standard deviation (red +) in (a) build-up time, (b) pulse duration, (c) peak power and (d) pulse energy against relative humidity as the cavity is purged with compressed air over 40 minutes.

ature was increasing while the TEC controller was operating at its peak current; upon observing this, the experiment was discontinued. The standard deviations of the pulse duration, energy and peak power appear to be constant (at around 0.31 ns, 0.39 kW and 15 µJ respectively) as the humidity decreases until these thermal effects set in. The standard deviation of the build-up time does not appear to be correlated to the relative humidity. Taking these together implies that the reducing humidity is not affecting the jitter.

### 4.2.4 Combined effect of ruggedisation, etalons and purging

Finally, the combined effect of the ruggedised system, purged cavity and mode control was tested. The etalons were placed at the same point in the cavity as in chapter 3 and are shown in position in figure 4.2. The diagnostics used were the same as those in the aforementioned chapter; the OSA has a resolution of 0.05 nm (or 10 GHz), the Fabry-Perot has a 10 GHz FSR and is used in conjunction with the boxcar integrator. The etalons were rotated until the OSA measured a single peak (as shown in the spectrum in figure 4.8b) with the mode content shown in figure 4.8a. As discussed in chapter 3, not achieving single-frequency operation leads to the expectation of minimal reduction in jitter compared to multi-longitudinal mode operation. The jitter was measured at this point and then the cavity was purged using dry air as before. After 20 minutes, the jitter, spectrum and Fabry-Perot interferometer output were recorded. As can be seen from comparing figure 4.8d to the pre-purge spectrum, the OSA still recorded a single peak. However, the appearance of the low power group of modes was evident in the Fabry-Perot trace shown in figure 4.8c. From this, it can be deduced that the water absorption (as a wavelength-dependent loss) was aiding the mode selectivity of the etalons.

Table 4.2 compares the percentage jitter values pre- and post-purging as well as with the breadboard system with the etalons discussed in chapter 3. A number of effects need explaining here, first the reduction in mean build-up time and jitter in build-up time, peak power and energy from the breadboard to 32 % relative humidity case is believed to be due to the ruggedisation. Second, the increase in mean duration and reduction in mean peak power and energy could all be due to the etalons not being aligned as optimally in the ruggedised system (alignment was made harder by the lack of commercial rotation mounts with scales due to size constraints). Third, differences between the 'ruggedised' and 'purged' cases are due solely to the reduction in humidity and are listed below.

1. The mean build-up time is reduced from 190 ns to 160 ns due to the lower loss when the water absorption is reduced as expected.
2. The mean peak power and pulse energy increased (from 5.9 kW to 7.8 kW and 0.25 mJ to 0.34 mJ respectively) for the same reason.
3. The standard deviations ($3\sigma$ values) of the build-up time and duration are reduced

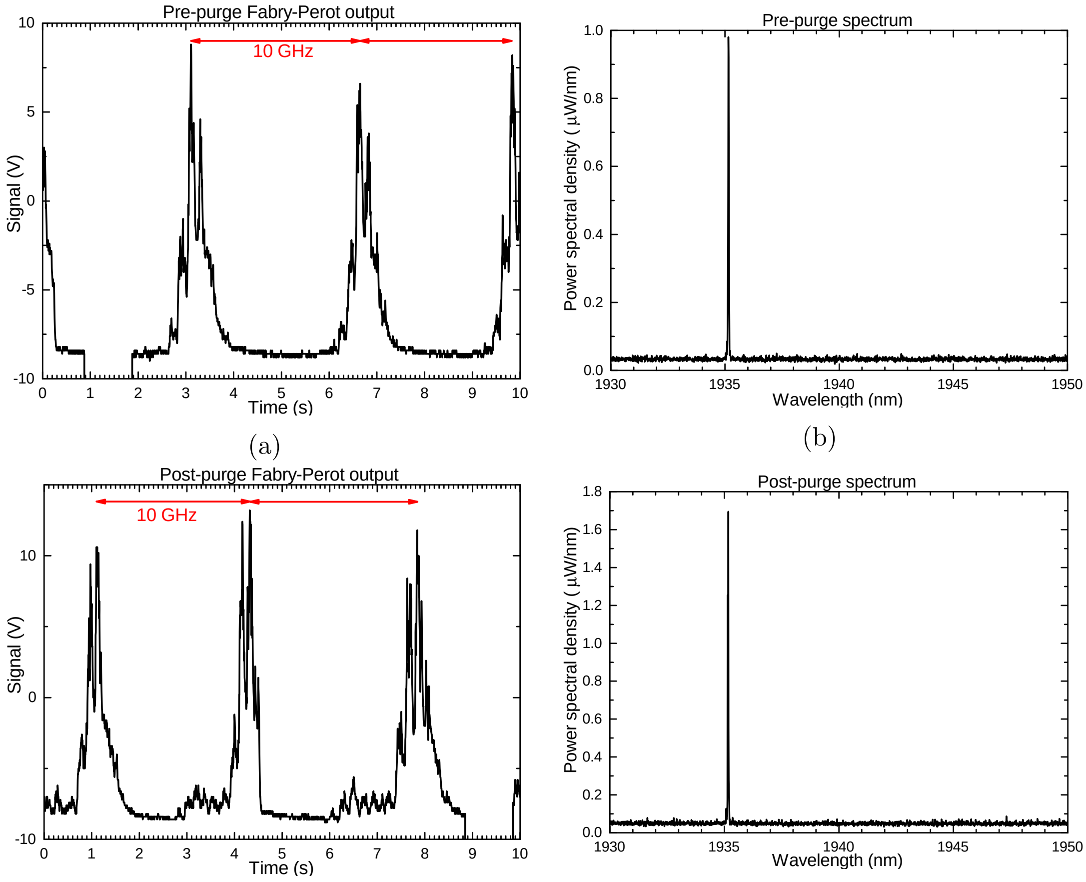

(a) (b)

(c) (d)

Figure 4.8: Pre- and post-purge spectra (taken using the OSA) and Fabry-Perot interferometer outputs showing the additional modes appearing after purging the cavity.

Table 4.2: Mean, standard deviation and percentage jitter in each pulse parameter for the ruggedised system with two etalons in the cavity before and after purging. All data taken at a repetition rate of 250 Hz and 4.9 W incident pump power with the 5 % output coupler. RH = relative humidity.

| Case | Build-up time | | | Pulse duration | | | Peak power | | | Pulse energy | | |
|---|---|---|---|---|---|---|---|---|---|---|---|---|
| | $\mu_{\tau_\mathrm{b}}$ (ns) | $3\sigma_{\tau_\mathrm{b}}$ (ns) | $\Delta\tau_\mathrm{b}$ (%) | $\mu_{\tau_\mathrm{p}}$ (ns) | $3\sigma_{\tau_\mathrm{p}}$ (ns) | $\Delta\tau_\mathrm{p}$ (%) | $\mu_{P_\mathrm{p}}$ (kW) | $3\sigma_{P_\mathrm{p}}$ (kW) | $\Delta P_\mathrm{p}$ (%) | $\mu_{E_\mathrm{p}}$ (mJ) | $3\sigma_{E_\mathrm{p}}$ (µJ) | $\Delta E_\mathrm{p}$ (%) |
| Breadboard (RH unknown) | 270 | 17 | 6.4 | 36 | 1.8 | 4.9 | 14 | 1.6 | 11 | 0.66 | 59 | 9.1 |
| Ruggedised (32 % RH) | 190 | 14 | 7.3 | 39 | 3.4 | 8.5 | 5.9 | 0.48 | 8.3 | 0.25 | 13 | 5.4 |
| Purged (7.0 % RH) | 160 | 12 | 7.5 | 39 | 1.1 | 2.8 | 7.8 | 0.64 | 8.1 | 0.34 | 23 | 7.0 |

from 14 ns and 3.4 ns to 12 ns and 1.1 ns respectively (although $\Delta\tau_\mathrm{b}$ is increased due to the reduction in the mean value).

4. The jitter in the peak power increased (0.48 kW to 0.64 kW) but proportionally to the mean value and so $\Delta P_\mathrm{p}$ stayed similar to the ruggedised value around 8 %.
5. The jitter in the pulse energy increased from 13 µJ (5.4 %) to 23 µJ (7.0 %). This is unexpected as the mean value has increased and the jitter in other parameters has decreased. Further investigation is required to explain this.

The small changes in the jitter in each parameter leads to the conclusion that the addition of purging to mode control has minimal effect.

## 4.3 Conclusions

Table 4.3 summarises the results presented in this chapter. There are three main conclusions to be drawn from the results. First, moving from the breadboard to the ruggedised system led to an improvement in the jitter (build-up time jitter reduced from 5.6 ns to 1.8 ns) but not to the target level of $3\sigma < 1$ ns. The jitter in the pulse energy also improved from 6.9 % to 2.6 %, beating the target of 3 %. This is thought

Table 4.3: Jitter in each pulse parameter compared across cavity conditions discussed in this chapter and with targets. All data taken at a repetition rate of 250 Hz and 4.9 W incident pump power with the 5 % output coupler.

| Case (relative humidity) | $3\sigma_{\tau_\mathrm{b}}$ (ns) | $3\sigma_{\tau_\mathrm{p}}$ (ns) | $3\sigma_{P_\mathrm{p}}$ (kW) | $\Delta E_\mathrm{p}$ (%) |
|---|---|---|---|---|
| Target | 1.0 | – | – | 3.0 |
| Breadboard (unknown) | 5.6 | 4.0 | 0.79 | 6.9 |
| Ruggedised (20 %) | 1.8 | 0.75 | 0.43 | 2.6 |
| Desiccated (13 %) | 1.8 | 0.38 | 0.35 | 2.2 |
| Purged (5.0 %) | 1.9 | 0.31 | 0.39 | 1.8 |
| Breadboard & etalons (unknown) | 17 | 1.8 | 1.6 | 9.1 |
| Ruggedised & etalons (32 %) | 14 | 3.4 | 0.48 | 5.4 |
| Ruggedised, etalons & purged (7.0 %) | 12 | 1.1 | 0.64 | 7.0 |

to be due to reduced vibrations disturbing the cavity alignment. Second, reducing the humidity within the cavity from $> 30\,\%$ to $\sim 15\,\%$ reduced the jitter in the pulse duration, peak power and energy (from around 0.75 ns, 0.36 kW and 2.6 % to about 0.38 ns, 0.29 kW and 2 % respectively) but had no effect on the build-up time jitter. Further humidity reduction to $\sim 5\,\%$ did not have any further effect on the jitter. This is believed to be due to other effects becoming the dominant causes of jitter when the humidity is reduced below 15 %. Third, combining the ruggedised cavity and mode control reduced the jitter in the build-up time (17 ns to 14 ns), peak power (1.6 kW to 0.48 kW) and energy (9.1 % to 5.4 %) compared to the breadboard and etalons case presented in chapter 3.1. Purging the cavity with the mode control improved the build-up time jitter further to 12 ns and brought the duration jitter down to 1.1 ns but made the jitter in the peak power and energy worse compared to pre-purging. In all cases involving the mode control, the jitter is considerably worse than the target levels. As explained in chapter 3.1, this is believed to be due to reducing the mode content increasing mode competition effects (such as beating) and this causing increased jitter.

As mentioned in chapter 3, it is thought that single-frequency operation will reduce the jitter and should combine with the reduction that has been achieved with the improved mechanical rigidity. Therefore, chapter 5 will describe the use of the pre-lase technique discussed in chapter 1.4.4.2 to enforce single-frequency operation.

# Chapter 5

# Pre-lase

Having made some improvement to the jitter with the ruggedised system (and succeeded in reaching the target energy jitter of 3 %), single-frequency operation will be investigated as a route to further reducing the jitter to the target levels. As mentioned in chapter 3.1, it is thought that mode competition effects are a major cause of jitter and the best way to remove these are to enforce single-frequency operation. Efforts to reduce the mode content were unable to reach single-mode due to the short build-up time and high gain associated with electro-optic Q-switching. Following the analysis in reference [63], equation 3.5 was used to estimate that 462 round-trips (taking approximately 1 µs) would be required for single-frequency operation with the etalons used in chapter 3; thus far, the laser has exhibited build-up times around 200 ns. Clearly a new technique is required to extend the build-up time if single-mode operation is to be achieved (the mode discrimination cannot be increased sufficiently due to the limiting of the etalon choice to stock components with no coatings due to damage concerns).

The pre-lase technique is a two-step switching process that allows increased build-up time without changing the cavity and is shown schematically in figure 5.1. This increased build-up time is achieved by decreasing the cavity losses to a point that allows only very-high-threshold laser oscillation on a single mode (point (a) in the figure) in the form of a series of relaxation oscillations. The build-up time to the first oscillation (marked (b) in figure 5.1) for this single-mode will be very long due to the high losses. Once this mode has built up to a pre-defined level, the cavity is switched to the low-loss

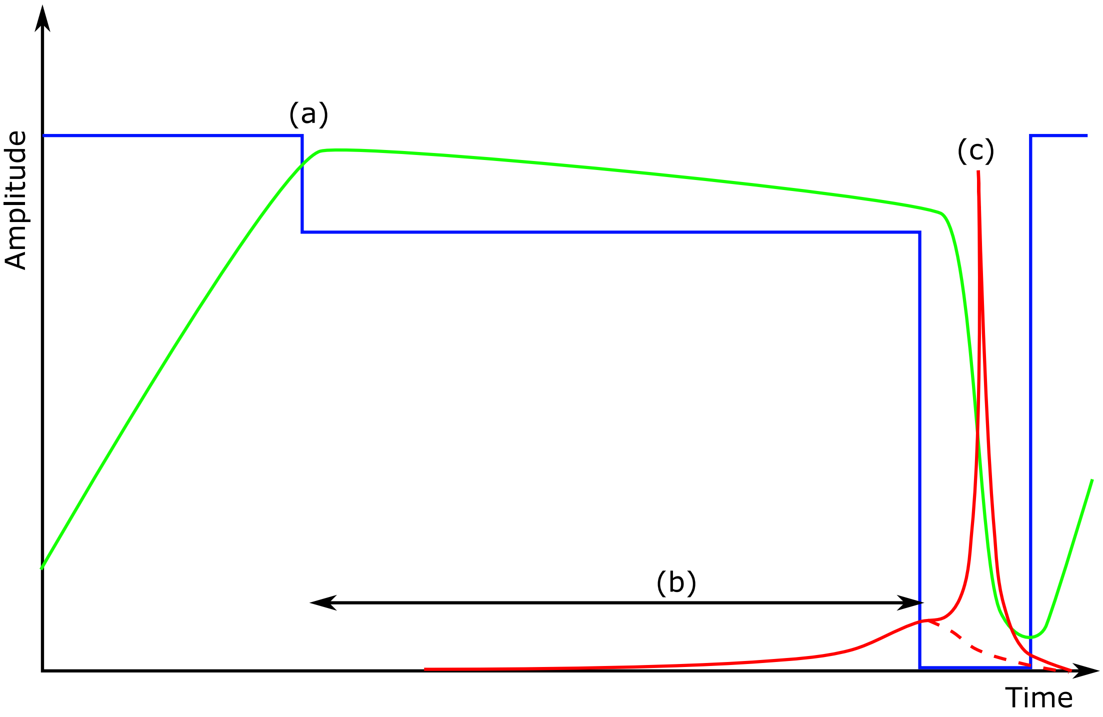

Figure 5.1: Schematic (not-to-scale) representation of the pre-lase process. The marked points correspond to: (a) the first loss change to allow high-threshold oscillation, (b) the single-frequency pre-lase pulse builds up from noise with a long build-up time, (c) the losses are switched to a low value and the single-mode sweeps out all the gain to produce a single-frequency pulse. Blue = loss, green = population inversion, red = pulse output. The red dashed line shows the tail of the pre-lase pulse that would be emitted if the second switch was not implemented.

state and the single mode out-competes all others to produce a single-frequency pulse (point (c)). For further information on the development of this technique, the reader is directed to references [89–92].

This chapter will detail the circuit design for implementing pre-lase in section 5.1 and the testing of the effect of pre-lase on the jitter in section 5.2. It will be shown that, even with pre-lase, single-frequency operation was difficult to attain with the etalon combination used in chapter 3.1; therefore, a thicker etalon was used and the cavity was made shorter. This necessitated the measurement of the jitter during standard Q-switching with the new cavity configuration in order to ascertain the effects of the pre-lase. These measurements will be discussed in section 5.2.3.

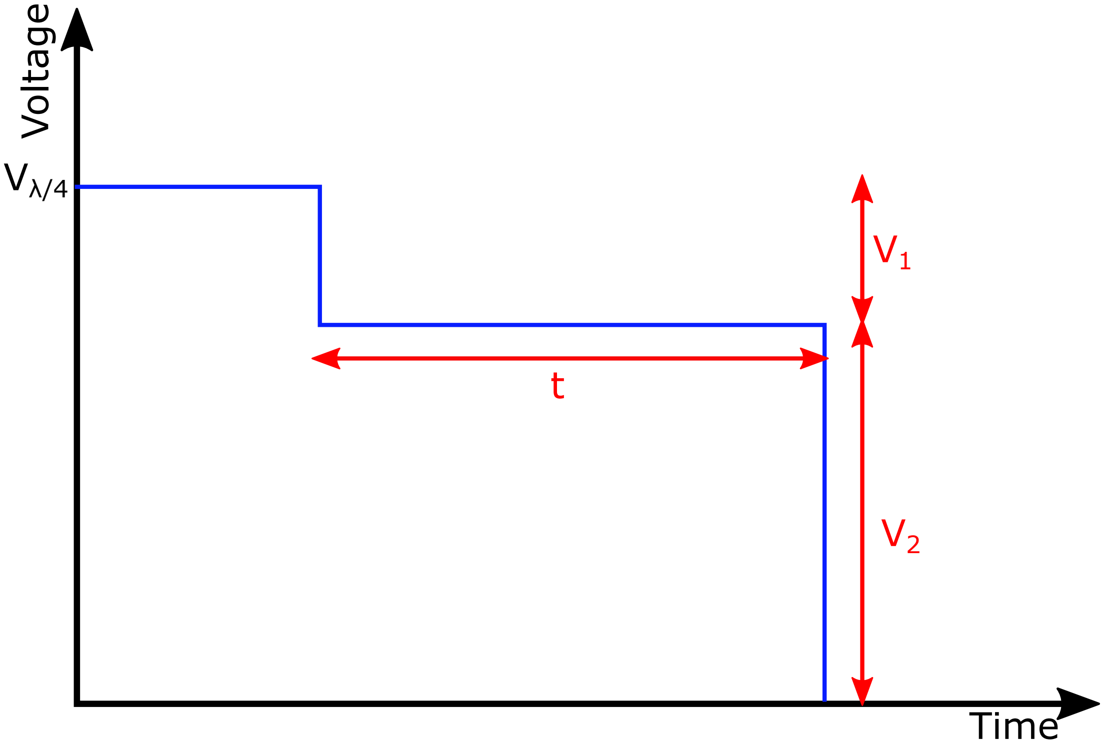

Figure 5.2: Schematic of the voltages applied during pre-lase. $V_1$ and $V_2$ are variable but should sum to $V_{\lambda/4}$ for optimal output. Time $t$ defines the build-up time.

## 5.1 Circuit design

A new switching circuit was needed to implement the two voltage steps required by pre-lase. The circuit was required to switch the applied voltages in $\sim 2\,\mathrm{ns}$ (as the previous switch was able to) and hold the first step for up to $10\,\mu\mathrm{s}$. This latter specification was to ensure a significant margin on the expected $\sim \mu\mathrm{s}$ build-up time required for single-frequency operation. Further requirements included the ability to alter the voltages and times (shown in figure 5.2) in real-time as well as minimal drift on the applied voltages.

The circuit design was contracted out to an expert (David Jones, Pulsed Power Consultancy) in such high-voltage-high-speed devices. He advised switching voltages down (as opposed to up as in the previous driver) to facilitate the “switch” between the high-loss and high-threshold states. As the speed of the switch is critical, the driver needs a very low resistance in order to minimise the RC time constant of the circuit (the Pockels cell is a capacitive load). By switching down the voltage, the switch can effectively be a short-circuit to ground implemented using a transistor. This has minimal components to add resistance and so the switching time is kept as short as possible. If voltages were to be switched up, a complex output stage would be necessary to charge the Pockels cell in the required short switching time. This can be achieved by using a suitable capacitance to act as a charge reservoir that would be dumped into the Q-switch. However, there are safety concerns with having a bank of capacitors storing high voltages. Due to this, the driver was designed to switch voltages down to ground.

The voltage steps were controlled with potentiometers. The first step is triggered by the "master" signal generator that is setting the repetition rate, this signal is also used to trigger the oscilloscope and another signal generator. The second signal generator is operated in delayed pulse mode – upon receiving the trigger, it waits an adjustable period of time before outputting a TTL signal itself to trigger the second step of the pre-lase. In order to facilitate the voltage switching, voltages are now applied to both terminals of the Pockels cell; the first voltage is negative and is applied to one side of the Pockels cell, the second is positive and is applied to the opposite terminal. In this way the potential difference across the Pockels cell is still equal to the quarter-wave voltage. This necessitated electrically isolating the Pockels cell from the ruggedised system (mounts were made of aluminium) as the lower electrode forms the mounting point. While doing this, it was critical that the Pockels cell remained in thermal contact with the base plate as previous work had discovered a serious degradation in laser performance as the Pockels cells are heated by the intracavity field. This requirement of an electrically insulating but thermally conductive interface between the Pockels cell and the base was met by using Sil-Pad, a fibreglass-reinforced, silicone-based insulator.

## 5.2 Testing results

Figure 5.3 shows a schematic of the setup used throughout these experiments. All pre-lase experiments were undertaken with the ruggedised housing described in chapter 4; data was also taken with the cavity purged as explained in the same chapter. The

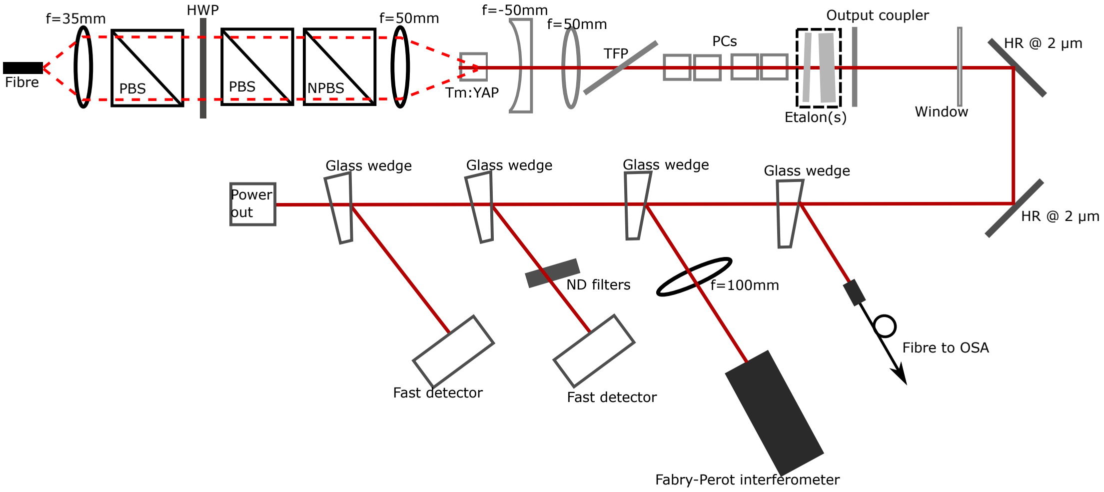

Figure 5.3: Schematic cavity diagram used while testing the effect of pre-lase on the jitter. All components between and including the crystal and window are contained within the purgeable ruggedised box. PBS = polarising beamsplitter, NPBS = non-polarising beamsplitter, HWP = half-wave plate, TFP = thin-film polariser, PCs = Pockels cells.

main difference between this cavity and those shown in previous chapters is the lack of a quarter-wave plate as now the laser is in the high-loss phase when voltage is applied. The second fast detector (a biased InGaAs photodiode from Hamamatsu without any ND filters) was used to observe the build-up of the pre-lase pulse and the trigger for the second step was set to coincide with the peak of the pre-lase pulse. The optimal voltages were found by setting a long delay for the second step to separate the pre-lase and Q-switched pulses then, starting with maximum voltage on the second step and zero on the first, the voltage of the first step was increased until a weak but sufficiently stable pre-lase pulse was observed (the voltage of the second step was decreased as necessary during this to avoid air breakdown around the Pockels cell).

### 5.2.1 Pre-lase results

Even with pre-lase extending the build-up time, single-frequency operation could not be consistently achieved. Therefore, the cavity was shortened in order to increase the mode spacing of the cavity from $\sim$ 600 MHz (cavity physical length $\sim$230 mm) to $\sim$ 800 MHz (cavity length $\sim$170 mm). This also reduced the mode size in the crystal

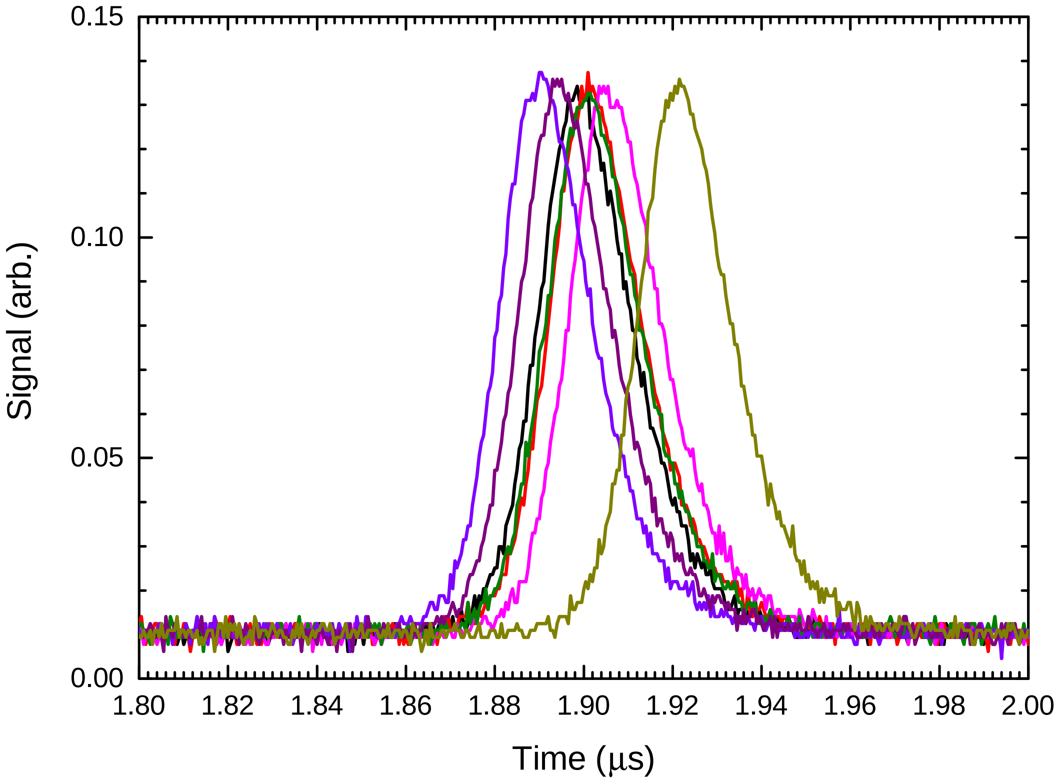

Figure 5.4: Example pre-lase pulses with a build-up time around 1.9 µs with no mode-beating; indicating single-frequency operation.

to between $\sim 110\,\mu\text{m} - 130\,\mu\text{m}$ across the simulated range of thermal lens focal lengths where the laser was stable. While the shortened cavity did lead to an improvement, reliable single-frequency operation still proved elusive and so the 5 mm YAG etalon was switched for one with a thickness of 12 mm. Consistent single-frequency operation was attained with the 12 mm etalon (and the shorter cavity), as evidenced by the lack of mode-beating on the pulses (as shown in figure 5.4) and corroborated by the spectra and Fabry-Perot interferometer output, recorded with the OSA and boxcar integrator and sample-and-hold circuit, respectively, as described in chapter 3.1, shown in figure 5.5.

As in previous chapters, 2500 consecutive pulses were recorded per data set and analysed to find the build-up time, pulse duration, peak power and energy of each pulse. The mean, standard deviation ($\sigma$) and percentage jitter (according to equations 2.2 and

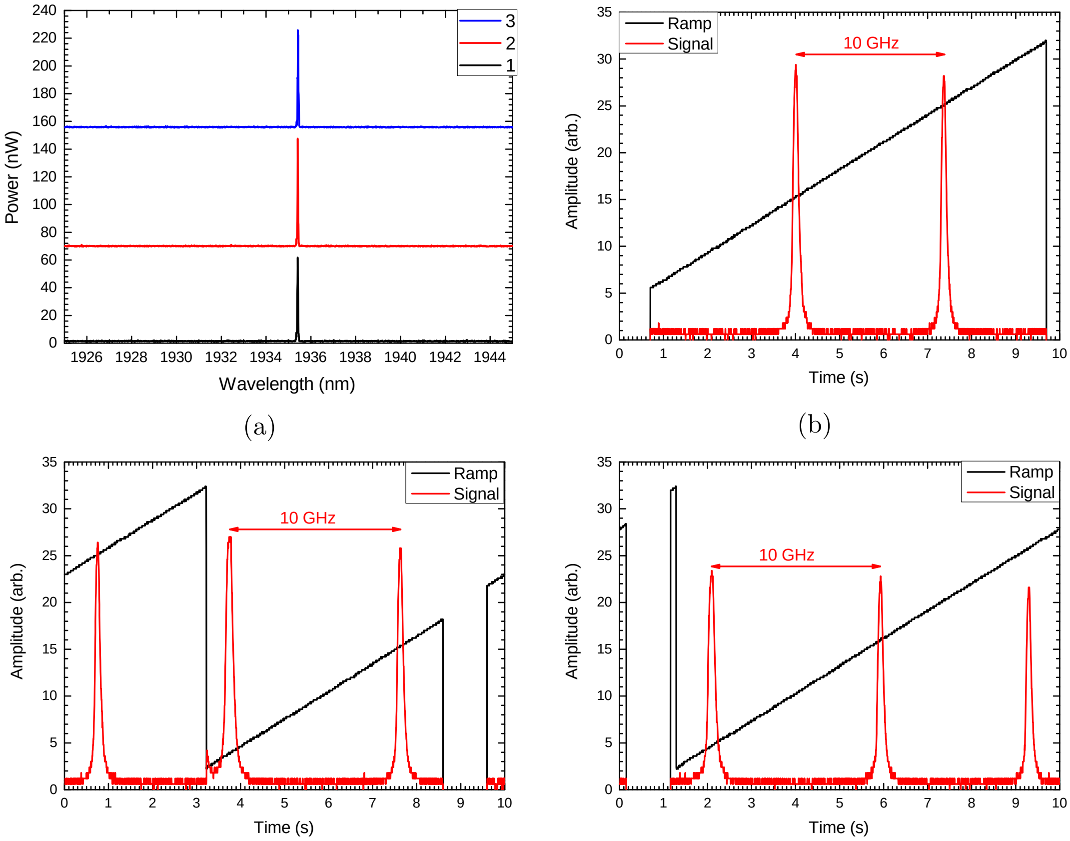

(a)

(b)

(c)

(d)

Figure 5.5: (a) Spectra measured by the OSA during pre-lase, the 3 measurements have been offset for clarity. (b) – (d) Fabry-Perot interferometer outputs confirming single-frequency operation during the 3 measurement runs. The laser mode spacing is ∼800 MHz.

2.3) were then calculated for each parameter. The jitter is taken as the percentage jitter for the pulse energy and the $3\sigma$ value for the other parameters. Three pre-lase data sets were recorded and the results of applying this analysis are shown in table 5.1 with the current best jitter result from the ruggedised system in chapter 4 for comparison. The first thing to notice is that the build-up time was successfully extended from 170 ns to around 2.0 µs by using the pre-lase (and as previously mentioned, this allowed reliable single-frequency operation). There was also a decrease in the mean pulse energy and peak power; this is to be expected as the laser is being forced to operate on a single mode and so will not extract all the energy pumped in to the system as it cannot access the gain at its nodes. The pulse duration also decreased which is likely to be mainly due to the shortened cavity length. However, the jitter in all parameters is worse when using the pre-lase:

- Averaging over the data sets, the build-up time jitter is $3\sigma_{T_b} \sim 19$ ns, compared to 1.8 ns for the ruggedised system and the target of 1 ns.
- The pulse duration jitter has increased from 0.75 ns to an average of $\sim 1.5$ ns.
- The peak power jitter has decreased from 0.43 kW to 0.41 kW and 0.26 kW for the first and third pre-lase data sets and increased to 1.2 kW for the second. While the decreases are welcome, clearly the variability is not as the aim with reducing the jitter is to improve the reproducibility.
- The pulse energy jitter is 16 %, compared to 2.6 % for the ruggedised system and the target level of 3.0 %.

It is believed that the jitter is worse as the pre-lase technique, as it has been implemented, deliberately enforces a low over-pumping ratio (as close to 1 as possible) during the build-up of the high-threshold pulse. As explained in chapter 1.4.4.1, large jitter is to be expected at low over-pumping ratios. The jitter is set by the over-pumping ratio during the time when the field builds up from noise. In the standard Q-switching case, the over-pumping ratio is around 10; in the pre-lase case, it is close to 1 and so the jitter is worse in this case.

Table 5.1: Mean, standard deviation and percentage jitter values for each pulse parameter during pre-lase experiments compared with standard Q-switching in the ruggedised system. All data taken at a repetition rate of 250 Hz and 4.9 W incident pump power with the 5 % output coupler. RH = relative humidity, $\mu_x$ = mean of $x$, $3\sigma_x$ = 3 times the standard deviation of $x$, $\Delta x = 3\sigma_x/\mu_x$ is the percentage jitter in $x$. $\tau_\mathrm{b}, \tau_\mathrm{p}, P_\mathrm{p}, E_\mathrm{p}$ are the build-up time, pulse duration, peak power and pulse energy.

| Case | RH (%) | Build-up time | | | Pulse duration | | | Peak power | | | Pulse energy | | |
|---|---|---|---|---|---|---|---|---|---|---|---|---|---|
| | | $\mu_{\tau_\mathrm{b}}$ (µs) | $3\sigma_{\tau_\mathrm{b}}$ (ns) | $\Delta\tau_\mathrm{b}$ (%) | $\mu_{\tau_\mathrm{p}}$ (ns) | $3\sigma_{\tau_\mathrm{p}}$ (ns) | $\Delta\tau_\mathrm{p}$ (%) | $\mu_{P_\mathrm{p}}$ (kW) | $3\sigma_{P_\mathrm{p}}$ (kW) | $\Delta P_\mathrm{p}$ (%) | $\mu_{E_\mathrm{p}}$ (mJ) | $3\sigma_{E_\mathrm{p}}$ (µJ) | $\Delta E_\mathrm{p}$ (%) |
| Ruggedised | 20 | 0.17 | 1.8 | 1.1 | 38 | 0.75 | 2.0 | 11 | 0.43 | 3.8 | 0.65 | 17 | 2.6 |
| Pre-lase | 45 | 1.9 | 22 | 1.2 | 24 | 1.0 | 4.3 | 8.5 | 0.41 | 4.8 | 0.23 | 37 | 16 |
| | 44 | 2.0 | 16 | 0.82 | 24 | 2.3 | 9.4 | 8.2 | 1.2 | 14 | 0.23 | 36 | 16 |
| | 44 | 2.0 | 20 | 0.99 | 23 | 1.1 | 4.6 | 8.2 | 0.26 | 3.2 | 0.22 | 35 | 16 |

### 5.2.2 Purged pre-lase

Having confirmed single-frequency operation (and not seen any jitter improvement), the next step was to investigate whether purging the cavity has any effect on the jitter. The cavity was purged with dry air to relative humidities < 4 %. This was found to stabilise the pre-lase pulse somewhat and so data was taken with the second step set to occur at different points on the pre-lase pulse to investigate if this affected the jitter. As shown in figure 5.6, the points chosen were fixed times defined empirically to coincide with the start, peak and end of the pre-lase pulse. The build-up time is still defined from the first loss step.

Data was taken twice and non-consecutively at each trigger point. Once again, single-frequency operation was confirmed by the lack of mode beating on the pulses as well as the spectra and Fabry-Perot interferometer traces shown in figure 5.7.

The results of applying the jitter analysis to the purged pre-lase for the three trigger positions are given in table 5.2. It is evident that reducing the humidity has not improved the jitter to the target levels ($3\sigma_{\tau_\mathrm{b}} < 1\,\mathrm{ns}$ and $\Delta E_\mathrm{p} < 3\,\%$), or even back to the levels attained in chapter 4 with the ruggedised system. Also, triggering at different points on the pre-lase pulse does not appear to have had any effect on the jitter or indeed the mean values of the parameters; this implies that, as long as the

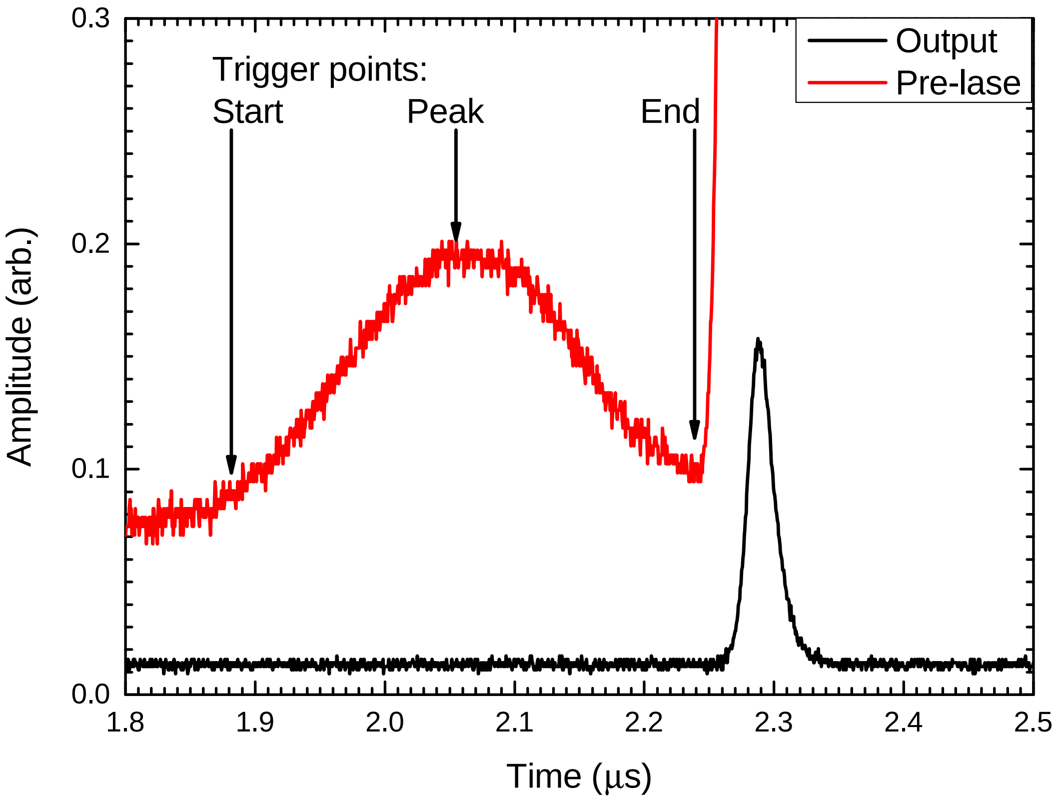

Figure 5.6: The three trigger points marked at their approximate locations on the pre-lase pulse. The output pulse is also shown for triggering at the end of the pulse, note the lack of mode beating due to single-frequency operation.

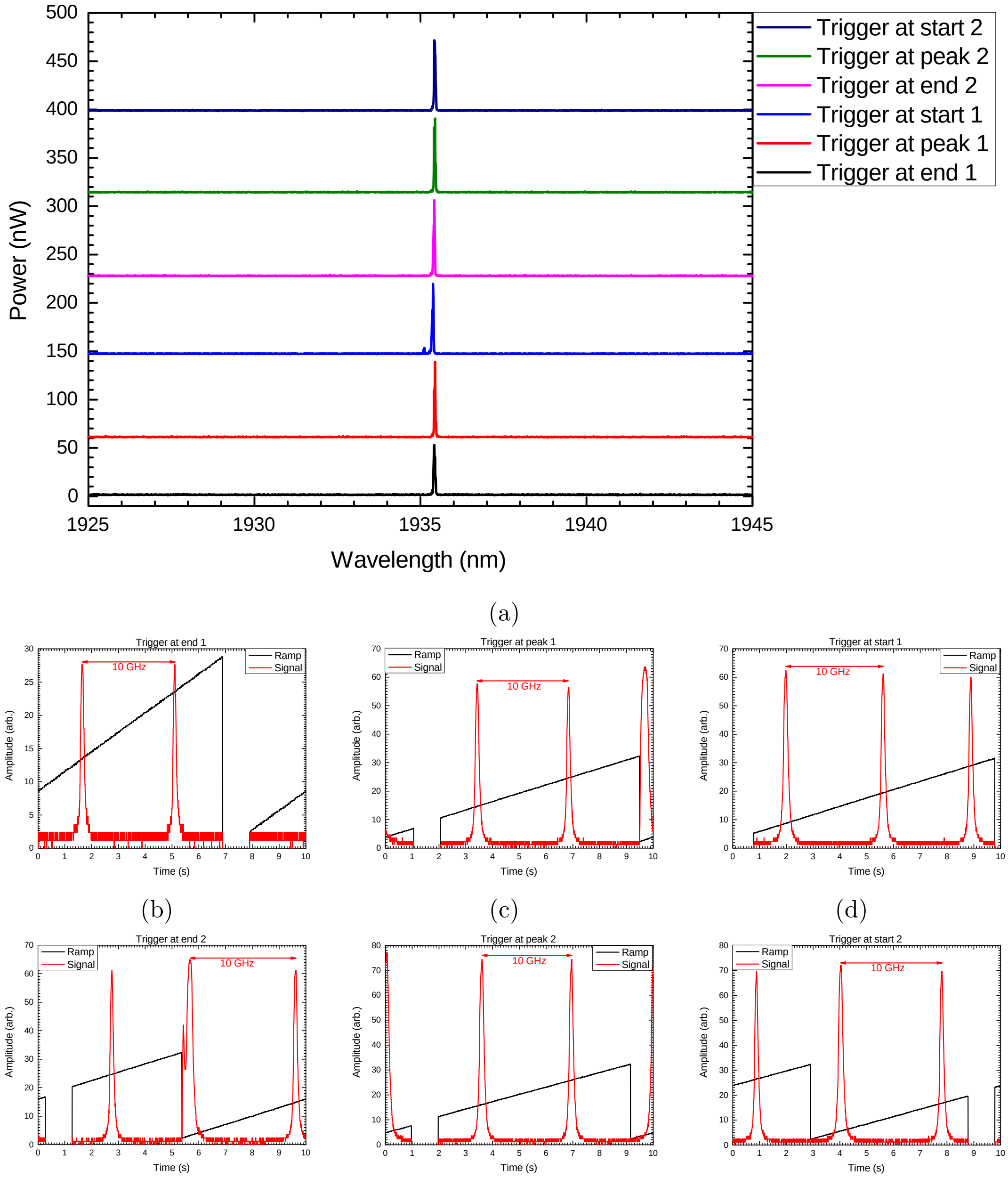

(a)

(b) (c) (d)

(e) (f) (g)

Figure 5.7: (a) Spectra measured by the OSA during purged pre-lase, the measurements have been offset for clarity. (b) – (g) Fabry-Perot interferometer outputs confirming single-frequency operation during the measurement runs (left to right: trigger at end, peak and start of pre-lase pulse; run 1 on top, run 2 below). As there is no evidence in the corresponding Fabry-Perot trace (d) of multi-mode oscillation, it is assumed that the small secondary peak in the blue spectrum is noise.

Table 5.2: Mean, standard deviation and percentage jitter values for each pulse parameter during purged pre-lase experiments. All data taken at a repetition rate of 250 Hz and 4.9 W incident pump power with the 5 % output coupler.

| Trigger point | RH (%) | Build-up time | | | Pulse duration | | | Peak power | | | Pulse energy | | |
|---|---|---|---|---|---|---|---|---|---|---|---|---|---|
| | | $\mu_{\tau_\mathrm{b}}$ (µs) | $3\sigma_{\tau_\mathrm{b}}$ (ns) | $\Delta\tau_\mathrm{b}$ (%) | $\mu_{\tau_\mathrm{p}}$ (ns) | $3\sigma_{\tau_\mathrm{p}}$ (ns) | $\Delta\tau_\mathrm{p}$ (%) | $\mu_{P_\mathrm{p}}$ (kW) | $3\sigma_{P_\mathrm{p}}$ (kW) | $\Delta P_\mathrm{p}$ (%) | $\mu_{E_\mathrm{p}}$ (mJ) | $3\sigma_{E_\mathrm{p}}$ (µJ) | $\Delta E_\mathrm{p}$ (%) |
| End | 3.0 | 2.3 | 12 | 0.53 | 23 | 1.0 | 4.4 | 10 | 0.45 | 4.4 | 0.26 | 41 | 16 |
| | 3.6 | 2.2 | 17 | 0.77 | 23 | 0.83 | 3.6 | 10 | 0.24 | 2.3 | 0.27 | 34 | 13 |
| Peak | 2.6 | 2.1 | 16 | 0.76 | 22 | 0.93 | 4.1 | 10 | 0.32 | 3.2 | 0.26 | 40 | 16 |
| | 3.1 | 2.1 | 16 | 0.79 | 23 | 0.87 | 3.8 | 10 | 0.28 | 2.7 | 0.26 | 36 | 14 |
| Start | 2.5 | 2.0 | 17 | 0.84 | 23 | 1.1 | 4.6 | 11 | 0.9 | 8.0 | 0.30 | 50 | 16 |
| | 2.8 | 1.9 | 18 | 0.92 | 23 | 0.89 | 3.9 | 9.5 | 0.24 | 2.5 | 0.25 | 35 | 14 |

pre-lase is single-frequency, the power of the seed is unimportant. Due to this, further comments on this data set will be made on averages over the six measurements. The mean build-up time was similar to the non-purged case at around 2 µs. This is expected as this is being set by the voltages applied with the slight variation due to the choice of trigger point. The mean peak power and pulse energy have increased to ∼ 10 kW and ∼ 0.27 mJ respectively from around 8.3 kW and 0.23 mJ for the non-purged case, this is understandable due to the decreased absorption due to atmospheric water vapour for the purged data. The average build-up time jitter was around 16 ns which is slightly lower than the average for the non-purged case (∼ 19 ns) but still significantly greater than the ruggedised system (1.8 ns). The mean pulse duration jitter was 0.94 ns which is also less than the non-purged case (1.5 ns) and higher than the ruggedised system (0.75 ns). Peak power jitter decreased from an average of ∼ 0.62 kW to ∼ 0.41 kW when purged, even including the anomalous-looking 0.9 kW jitter for one run. The pulse energy jitter has slightly decreased from 16 % to 15 %, although this is still well above the target level of 3 % or ruggedised system performance of 2.6 %.

It is apparent based on these comparisons that purging the cavity has had a small effect but not enough to counter the large jitter originating in the pre-lase pulse due to its low over-pumping ratio.

Table 5.3: Mean, standard deviation and percentage jitter values for each pulse parameter during Q-switching in the cavity configuration used for pre-lase. All data taken at a repetition rate of 250 Hz and 4.9 W incident pump power with the 5 % output coupler.

| Case | RH (%) | Build-up time | | | Pulse duration | | | Peak power | | | Pulse energy | | |
|---|---|---|---|---|---|---|---|---|---|---|---|---|---|
| | | $\mu_{\tau_\mathrm{b}}$ (ns) | $3\sigma_{\tau_\mathrm{b}}$ (ns) | $\Delta\tau_\mathrm{b}$ (%) | $\mu_{\tau_\mathrm{p}}$ (ns) | $3\sigma_{\tau_\mathrm{p}}$ (ns) | $\Delta\tau_\mathrm{p}$ (%) | $\mu_{P_\mathrm{p}}$ (kW) | $3\sigma_{P_\mathrm{p}}$ (kW) | $\Delta P_\mathrm{p}$ (%) | $\mu_{E_\mathrm{p}}$ (mJ) | $3\sigma_{E_\mathrm{p}}$ (µJ) | $\Delta E_\mathrm{p}$ (%) |
| Ruggedised | 20 | 170 | 1.8 | 1.1 | 38 | 0.75 | 2.0 | 11 | 0.43 | 3.8 | 0.65 | 17 | 2.6 |
| No etalons, old driver | 31 | 220 | 3.6 | 1.6 | 20 | 3.0 | 15 | 48 | 17 | 35 | 0.87 | 57 | 6.5 |
| | 32 | 220 | 3.3 | 1.5 | 22 | 2.8 | 13 | 44 | 10 | 24 | 0.95 | 59 | 6.2 |
| No etalons | 31 | 210 | 3.9 | 1.8 | 22 | 2.8 | 13 | 54 | 14 | 25 | 1.1 | 59 | 5.1 |
| | 31 | 210 | 3.6 | 1.7 | 22 | 2.8 | 13 | 56 | 14 | 25 | 1.2 | 57 | 4.8 |
| | 31 | 220 | 3.6 | 1.7 | 22 | 2.8 | 13 | 53 | 13 | 24 | 1.1 | 56 | 4.8 |
| No etalons, purged | 2.9 | 210 | 3.7 | 1.8 | 22 | 2.8 | 12 | 63 | 16 | 25 | 1.4 | 67 | 4.8 |
| | 2.7 | 210 | 3.4 | 1.6 | 22 | 2.8 | 12 | 63 | 15 | 24 | 1.4 | 56 | 4.0 |
| | 2.5 | 210 | 5.6 | 2.7 | 23 | 2.8 | 12 | 61 | 14 | 24 | 1.4 | 77 | 5.6 |
| 2 modes | 62 | 330 | 17 | 5.1 | 29 | 3.8 | 13 | 6.2 | 2.0 | 33 | 0.13 | 19 | 15 |
| | 60 | 280 | 13 | 4.7 | 23 | 3.0 | 13 | 15 | 5.0 | 34 | 0.26 | 31 | 12 |
| | 58 | 260 | 14 | 5.5 | 22 | 2.1 | 9.4 | 14 | 5.9 | 43 | 0.26 | 23 | 8.9 |
| Etalons, purged | 4.8 | 260 | 15 | 6.0 | 22 | 2.3 | 10 | 14 | 4.2 | 29 | 0.34 | 35 | 10 |
| | 2.3 | 270 | 13 | 4.7 | 23 | 3.0 | 14 | 15 | 5.4 | 35 | 0.26 | 29 | 11 |
| | 4.0 | 310 | 18 | 6.0 | 28 | 4.5 | 16 | 9.4 | 3.7 | 39 | 0.23 | 35 | 15 |
| | 3.5 | 280 | 10 | 3.6 | 26 | 4.3 | 16 | 16 | 6.3 | 39 | 0.42 | 43 | 10 |
| | 2.8 | 300 | 18 | 6.1 | 28 | 6.0 | 21 | 11 | 6.0 | 56 | 0.30 | 36 | 12 |

### 5.2.3 A fairer comparison

In previous sections, the jitter in the pre-lase and purged pre-lase cases has been compared to that in the ruggedised system. This was done in order to compare to the best jitter performance attained throughout this work. However, it is more informative to make a like-for-like comparison as the cavity length has been changed and a new etalon thickness used. Therefore, small data sets were taken under various conditions with the new cavity length. The results are summarised in table 5.3 and discussed below case-by-case, as well as compared to the pre-lase results detailed above. All cases use the ruggedised housing.

**No etalons, old driver** The first case presented used the old driver (and therefore replaced the quarter-wave plate in the cavity). This should produce results similar to those presented in chapter 4 and is shown at the top of table 5.3 for comparison. The mean build-up time is longer at 220 ns compared to 170 ns for the longer cavity, although it is unknown why. Possible explanations include worse alignment or mode overlap with the pump, although both of these are contradicted by the increase in pulse energy. Another possibility is the increased humidity from 20 % to 31 %, further investigation would be required to confirm this. The average pulse duration is shorter at $\sim$ 21 ns compared to 38 ns, this is probably caused by the combination of shorter round-trip time due to the shorter cavity (this could contribute roughly half of this discrepancy as the cavity optical length, proportional to the pulse duration according to equation 1.5, was reduced by almost 25 %) and increased losses due to the higher humidity. The mean pulse energy has increased to $\sim$ 0.91 mJ (compared to 0.65 mJ), this could be due to better alignment of the system. The knock-on effect of increased energy and shorter pulse duration is that the peak power is $\sim$ 4× higher at around 46 kW. The jitter in all parameters is higher compared to the previous work – the build-up time jitter has increased from 1.8 ns to around 3.5 ns and from 2.6 % to $\sim$ 6.4 % for the energy. Jitter has also increased in the duration (0.75 ns to around 2.9 ns) and peak power (0.43 kW to about 14 kW).

**No etalons** For this case, the pre-lase driver was connected such that both steps occurred at the same time (ie. standard Q-switching) and the voltages were adjusted in order to minimise the build-up time and maximise the peak power of the output pulses. In this way, the performance of the circuit can be compared to the old driver. For similar relative humidity values to the old driver case described above (three measurements at 31 % as opposed to one at 31 % and one at 32 %), the new driver produced pulses with very similar build-up times (around 220 ns) and pulse durations (around 22 ns) as the old driver. However, the pulses produced using the pre-lase driver were found to have greater average peak powers (54 kW compared to 46 kW) and pulse energies (1.1 mJ compared to 0.91 mJ); it is unknown why this is but could be partly attributed to the decreased cavity losses due to the removal of the quarter-wave plate. The magnitude of this loss change is not just due to losses at the surfaces of the wave plate, but also due to the interplay between the residual birefringence of the Pockels cells and the polariser which may have been reduced by the phase shift caused by the wave plate. $3\sigma$ jitter values are similar in all parameters: 3.7 ns, 2.8 ns, 14 kW and 57 µJ compared to 3.5 ns, 2.9 ns, 14 kW and 58 µJ for the build-up time, pulse duration, peak power and energy respectively. The increased mean peak power and energy led to the percentage jitter being slightly lower in these parameters with the pre-lase driver. Compared to the data presented in chapter 4, the jitter is still higher in all parameters (as with the previous case) but with shorter pulses on average and increased mean peak power and energy.

**No etalons, purged** While using the pre-lase driver, the cavity was purged with dry air and the usual jitter data taken. This had no effect on the pulse duration compared to pre-purging; the mean value, standard deviation and (therefore) percentage jitter remained constant at 22 ns, 2.8 ns and 12 % respectively. As expected with removing the loss due to water absorption, the average peak power and energy have increased to ∼ 61 kW and 1.4 mJ (from 46 kW and 1.1 mJ) respectively. The percentage jitter in the peak power and energy remained constant at ∼24 % and 4.8 % respectively. The jitter in the build-up time was similar to the pre-purge values for two of the three measurements (values of 3.7 ns, 3.4 ns and 5.6 ns compared to 3.9 ns, 3.6 ns and 3.6 ns) with the third exhibiting significantly more variation for an unknown reason. Once again, all jitter values are higher than those recorded in chapter 4.

**2 modes** The next case to be considered involved re-inserting the etalons in to the cavity. The idea was to record the jitter while the laser oscillated on 2, 3 and 4 adjacent modes as in chapter 3.1 (single-frequency operation was not possible without pre-lase even in the shorter cavity with the 12 mm etalon). However, using the 12 mm etalon as opposed to the 5 mm used in that chapter, only 2-adjacent-mode or multi-non-adjacent-mode operation could be achieved. The increase in cavity losses due to the etalons increased the mean build-up time and pulse duration from 210 ns and 22 ns to ∼290 ns and ∼25 ns respectively, with a decrease in peak power and energy from 54 kW and 1.1 mJ to 12 kW and 0.22 mJ respectively (all averaged over the three runs). Just as in chapter 3.1, restricting the mode content of the laser led to an increase in jitter compared to the free-running case above. The build-up time jitter increased from 3.7 ns to around 15 ns, percentage jitter in the peak power and pulse energy also increased to ~37 % and ~12 % from 25 % and 4.9 % respectively. Curiously, the pulse duration jitter remained relatively constant around 3.0 ns or 12 %. These jitter values are generally higher (with the exception of the build-up time) than those reported in chapter 3.1, where the jitter values were 18 ns, 0.92 ns, 5.0 % and 5.0 % for the build-up time, pulse duration, peak power and energy respectively. It is unknown why this is but could be due to a combination of the following; different humidity during the two experiments, different mode overlap in the crystal due to the differing mode spacing or indeed other effects due to the new cavity design.

**Etalons, purged** As in chapter 4, the cavity was purged once the etalons were set such that the laser oscillated on two adjacent modes. As before, the reduced water absorption after purging allowed new modes to oscillate. In this case there is a slight reduction in the average build-up time compared to the 2 modes case above to ~280 ns as well as an increase in the mean peak power and energy to ~13 kW and 0.31 mJ respectively. The average pulse duration remained similar at around 25 ns. The build-up time jitter stayed around 15 ns, the pulse duration jitter increased from 3.0 ns to ~4.0 ns, the peak power percentage jitter increased from ~37 % to ~40 % and the pulse energy jitter remained around 12 %. The conclusions to be drawn here are that, as seen previously, reducing the humidity (and therefore losses) allows greater power and energy to be emitted on average but with increased jitter. The increased jitter is thought to be due to more modes oscillating, whether these modes are present for every pulse or if the jitter is due to changes in pulse mode content cannot be discovered at this time.

**Comparison to pre-lase** Here the results of the pre-lase will be compared to the relevant cases above. First comparing the un-purged pre-lase from section 5.2.1 to the “no etalons” and “2 modes” cases. Obviously the mean build-up time is much greater in the pre-lase case by design (>1.9 µs compared to ∼210 ns – 290 ns). The pulse durations are comparable at 22 ns, ∼25 ns and 24 ns for the "no etalons", "2 modes" and pre-lase respectively. The average peak power is lower for the pre-lase case at ∼8.3 kW compared to 54 kW and 12 kW for the other cases. The pulse energy of the pre-lase is similar to the "2 mode" case (0.23 mJ compared to 0.22 mJ) and both are lower than the "no etalon" case (1.1 mJ), as should be expected due to the increased losses and deliberate mode selectivity. In terms of jitter, the build-up time jitter is higher in the pre-lase case at ∼19 ns compared to 3.7 ns and ∼15 ns for the "no etalons" and "2 modes" cases respectively. Likewise, the pulse energy jitter has increased to 16 % from 4.9 % and 12 %. Curiously, the jitter in the pulse duration and peak power has decreased to 6.1 % and 7.3 % respectively, compared to 13 % and 25 % for the "no etalons" case and 12 % and 37 % for the "2 modes" case.

Comparing the purged pre-lase to the "no etalons, purged" and "etalons, purged" cases, the same pattern plays out. Pulse durations are similar across the three cases (23 ns, 22 ns and 25 ns in the order specified) with reducing peak power from 54 kW for "no etalons, purged" to 13 kW for "etalons, purged" to 10 kW for purged pre-lase. Average pulse energy follows the same pattern as the peak power from 1.4 mJ to 0.31 mJ to 0.27 mJ. In terms of jitter, the purged pre-lase case has higher build-up time jitter at 16 ns compared to 4.2 ns and 15 ns for the "no etalons, purged" and "etalons, purged" cases respectively. Similarly, the pulse energy jitter has increased from 4.8 % and 12 % to 15 %. As with the non-purged case above, the jitter in the pulse duration and peak power have decreased to 4.1 % and 3.9 % respectively from 12 % and 24 % for the "no etalons, purged" case and 15 % and 40 % for the "etalons, purged".

From these comparisons, it is clear that the pre-lase is reducing the jitter in the pulse duration and peak power while increasing the jitter in build-up time and energy as well as reducing the average peak power and energy.

## 5.3 Conclusions

In summary, the pre-lase technique has been successfully implemented and increased the build-up time to ~2 µs; coupled with a shorter cavity and a 12 mm etalon in place of the 5 mm one used previously, this enabled single-frequency operation. Compared to the ruggedised system as presented in chapter 4, the jitter in all parameters has increased (from 1.8 ns, 0.75 ns, 0.43 kW and 2.6 % to >16 ns, >1 ns, ~0.62 kW and 16 % for the build-up time, pulse duration, peak power and energy respectively) and the average peak power and pulse energy decreased. Combining the pre-lase with purging the cavity reduced the jitter but not to the target levels or the ruggedised system performance.

Due to the change in cavity length and etalon thickness, data was taken under various conditions while employing standard Q-switching. It was found that the pre-lase driver (when configured for standard Q-switching) performed slightly better than the old driver used in previous chapters; $3\sigma$ jitter values were similar across all parameters (3.7 ns, 2.8 ns, 14 kW and 57 µJ compared to 3.5 ns, 2.9 ns, 14 kW and 58 µJ) and the average peak power and pulse energy increased due to the lack of a quarter-wave plate in the cavity.

Comparing the pre-lase to standard Q-switching with and without etalons, it was found that the pre-lase technique reduces the jitter in the pulse duration (to 6.1 % from 13 % without etalons and 12 % with) and peak power (to 7.3 % from 24 % and 40 %) while increasing the jitter in build-up time (to 19 ns from 3.7 ns and 15 ns) and energy (to 16 % from 4.9 % and 12 %), as well as reducing the average peak power and energy.

The higher jitter compared to the ruggedised system presented in chapter 4 is due to the pre-lase pulse (that subsequently seeds the main output) is deliberately generated with a low over-pumping ratio. This was shown in chapter 1.4.4.1 to lead to high jitter. There are three possible methods of progressing to reduced jitter, as described below. Due to time constraints, none of these could be tested but they will be expanded upon in chapter 6.3.

1. Alter the pre-lase driver to incorporate a PID control on the cavity losses during

the pre-lase build-up as described in [89]. By using this technique, it would be possible to force the pre-lase to become a stable CW level which would then, the author believes, seed a Q-switched output with reduced jitter.

2. Through careful design, it should be possible to create a cavity that will naturally oscillate on a single-longitudinal mode when Q-switched, without the need for pre-lase. Options for this could include a ring cavity or cavity short enough to have such a large mode spacing that enforcing single-frequency is trivial. The author is of the opinion that this would exhibit reduced jitter compared to a multi-mode cavity.
3. Another possibility would be to optically trigger the second step in the pre-lase and then gate any subsequent measurements from the optical trigger. Optical triggering tends to translate amplitude variations into time jitter so this would further stabilise the peak power. Gating subsequent measurements in this way would remove the build-up time jitter (which would have increased) from the measurements. The suitability of this would be application dependent.

# Chapter 6

# Conclusion

Having presented the results of the experiments done throughout this doctorate, this chapter will begin in section 6.1 with a summary of the work done for this thesis, define the current optimal method of reducing the jitter in section 6.2 and discuss some ideas for future improvements in section 6.3.

## 6.1 Summary

This thesis began with defining jitter as the pulse-to-pulse fluctuations in the pulse parameters (build-up time, pulse duration, peak power and pulse energy). These variations are due to changes in the over-pumping ratio, defined as the ratio of the population inversion before the pulse to the threshold value, which can be due to changes in the pump and/or losses in the cavity. Targets for the jitter were specified based on the datasheets of various commercial Q-switched neodymium lasers as $<1\,\mathrm{ns}$ for the build-up time jitter and $<3\,\%$ for the pulse energy.

The jitter was quantified for various combinations of pump power, repetition rates and output couplers in a benchmark data set in chapter 2. Here, the method for quantifying jitter was as follows; many consecutive pulses were recorded and the pulse parameters for each were calculated. From this, the mean ($\mu$) and standard deviation ($\sigma$) of each parameter were found. The jitter was defined to be the $3\sigma$ value and the percentage jitter $300\sigma/\mu$. The $3\sigma$ definition was chosen as the values of each parameter

Table 6.1: Summary of results with the best jitter performance highlighted. All for the standard combination used throughout this work: a repetition rate of 250 Hz and 4.9 W incident pump power with the 5 % output coupler.

| Case | Build-up time jitter $3\sigma_{\tau_b}$ (ns) | Pulse energy jitter $\Delta E_p$ (%) |
|---|---|---|
| Target | 1.0 | 3.0 |
| Benchmark | 5.6 | 6.9 |
| 4 adjacent modes | 17 | 5.1 |
| 3 adjacent modes | 20 | 3.5 |
| 2 adjacent modes | 18 | 5.0 |
| Ruggedised | 1.8 | 2.6 |
| Purged | 1.9 | 1.8 |
| Pre-lase | 19 | 16 |
| Purged pre-lase | 16 | 15 |

were found to be approximately normally distributed and so the region between $\mu - 3\sigma$ and $\mu + 3\sigma$ contains 99.7 % of events. The jitter in the benchmark system was found to be 5.6 ns and 6.9 % for the build-up time and pulse energy respectively for the combination of 4.9 W incident pump power, 250 Hz repetition rate and 5 % output coupler. All results as well as the target are summarised in table 6.1.

As mode beating was observed on the pulses recorded in the benchmark data set, the first improvement tested was longitudinal mode control using YAG etalons. Etalon thicknesses of 0.25 mm and 5 mm were used to force laser oscillation on 2, 3 and 4 adjacent modes. The mode content of the laser was observed using a scanning Fabry-Perot interferometer with a custom boxcar integrator and sample-and-hold circuit. It was found that reducing the mode content *increased* the build-up time jitter to 17 ns, 20 ns and 18 ns for 4, 3 and 2 modes respectively. This is believed to be due to increased mode competition effects as the number of modes decreases in a similar way to in a CW laser where reduced mode content (towards 2 mode oscillation) increases amplitude instabilities.

Next, improvements to the mechanical stability were tested. The aim was to reduce any variation of cavity losses due to vibration by reducing the number of degrees of freedom on all optics to the minimum required for alignment. This was quite successful:

pulse energy jitter was reduced to 2.6 %, below the target level of 3 %. The build-up time jitter remained above target at 1.8 ns but represents a factor of three improvement over the benchmark data set. The ruggedised system was also designed to allow purging of the cavity to reduce the atmospheric absorption of wavelengths around 2 µm. Purging with dry air further reduced the pulse energy jitter to 1.8 % with similar jitter in the build-up time as the pre-purged case. Purging also increased the mean peak power and pulse energy, as expected due to reduced losses.

The final improvement attempted was to use a modified Q-switching technique known as pre-lase to enforce single-frequency operation. The pre-lase technique is a two-step switching method that allows the build-up of a high-threshold single-frequency pulse in the first step. This goes on to seed the main pulse in the second step. Using this technique with a shortened cavity and a 12 mm etalon in place of the previously used 5 mm one, single-frequency operation was attained. However, the high-threshold nature of the seed pulse causes it to exhibit large jitter due to the low over-pumping ratio and this jitter is transferred to the main pulse. This caused the Q-switched pulses from the pre-lase system to exhibit jitter levels (19 ns and 16 % respectively) similar to those observed when the laser oscillated on 2, 3 and 4 modes. Combining the pre-lase with purging produced an improvement in the jitter to 16 ns and 15 %; however, this is still above the target levels of 1 ns and 3 %.

## 6.2 Current optimal method of reducing jitter

The current best jitter performance in the presented thulium laser is highlighted in table 6.1 and was achieved upon changing from the breadboard to the ruggedised system. The non-purged case gave slightly better build-up time jitter at 1.8 ns while the purged case gave lower pulse energy jitter at 1.8 %. However, the pulse energy jitter is below the target of 3 % in both cases. It should also be remembered that purging generally allows greater average peak powers and pulse energies due to the reduced water absorption in the cavity.

## 6.3 Future work

As mentioned above, the build-up time jitter is still above the target of 1 ns. Therefore, in this section, ideas for further improvements will be presented. The first possibility involves modifying the pre-lase method employed. The current version uses the original pre-lase technique from [90] where high-threshold oscillation allows a weak seed pulse to form. As previously identified, the high-threshold oscillation is, by definition and design, operating at a low over-pumping ratio and it was identified in chapter 1.4.4.1 that a low over-pumping ratio leads to high jitter. Therefore, the proposed modification would follow the work presented in [89] to change the pre-lase pulse to a stable CW level. This would be done, as described in [89], by using a PID control to manipulate the voltage applied to the Pockels cell in the first step to keep a constant CW output (monitored on a photodiode). A PID control is required as waiting for a CW level to establish itself naturally would take a time comparable to the upper laser level lifetime of 4 ms. Using this technique, a jitter improvement of a factor of four was reported in [89]: amplitude jitter was reduced from 8 % with the standard pre-lase technique to <2 % when stabilised and timing jitter from 4 ns to 1 ns. Using a single-frequency CW seed in place of the weak pulse will allow a single-frequency pulsed output (as demonstrated with injection seeding from a CW source in, for example, [106–108]) with no jitter transferred from the first pre-lase voltage step.

The second possibility for future work would employ standard Q-switching in a cavity designed to oscillate on a single frequency naturally. Such a design would need to have a large mode spacing and sufficient mode selectivity to suppress adjacent modes. Figure 6.1 shows one such cavity design with a mode spacing of >1.8 GHz. In order to shrink the cavity as much as possible, it is proposed that the inner surface of the laser crystal be cut at Brewster's angle and coated to act as a polariser at the laser wavelength to increase the proportion of vertically-polarised power coupled out of the cavity. A Volume Bragg Reflector (VBR) is used in place of the output coupler to combine end mirror and a wavelength selective element in one (see, for example, reference [109] for a full description of VBRs). A 5 mm thick VBR available from OptiGrate would have

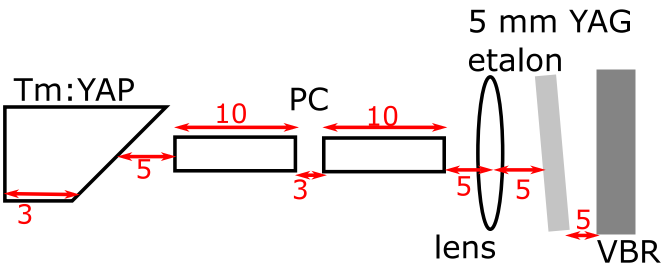

Figure 6.1: Proposed short cavity for single-frequency operation with standard Q-switching. The outer face of the Tm:YAP crystal would be coated HR at the laser wavelength and AR at the pump wavelength, the inner face would be cut at Brewster's angle and coated to act as a polariser. The lens is for cavity stability, initial modelling suggests a focal length of 50 mm would be suitable. PC = Pockel cell, VBR = Volume Bragg Reflector. All red numbers are lengths in mm.

a bandwidth of 0.3 nm (~24 GHz) at 1940 nm; combined with a 5 mm YAG etalon and the short cavity, this should enable single-frequency operation. Throughout this work, there have been two Pockels cells in the cavity to allow cavity dumping as the crystals forming the cells used are too short for the quarter-wave voltage (inversely proportional to the cell length) to be applied to each crystal without air breakdown. Using longer crystals in the Pockels cell allows each crystal to be driven independently, reducing the overall cavity length and the number of surfaces in the cavity.

Another route to explore would be to refine the ruggedised system presented in chapter 4. Removing more degrees of freedom and better mounting of optics, for example by using adhesive, may reduce vibrations further. Mounting the entire system on either rubber feet or floating the optical table may also assist in this. The ruggedisation as presented in this work has demonstrated a reduction of a factor of three in build-up time jitter and a factor of two in pulse energy jitter. While this is still a factor of two short of the target on the build up time jitter, the improvements outlined in this chapter should enable reaching this target.

In conclusion, Q-switched 2 µm lasers are attractive for various applications. However, practical implementations can be limited by jitter; the severity of which is attributed to the quasi-three-level nature of the gain materials that emit at this wavelength. This thesis has evaluated several approaches to reducing the jitter, including longitudinal- and transverse-mode control, ruggedisation and purging. Some progress has been made; the pulse energy jitter was reduced below the target of 3 % using the ruggedised system. However, further work is required to match the stability readily available from commercial 1 µm lasers.

# Appendix A

# Benchmark data set - complete results

The following tables show the mean, standard deviation and percentage jitter values of each parameter for each combination of operating parameters used in the benchmark data set. Each table shows the values organised by repetition rate for a given output coupler. Recall that the percentage jitter is defined as $\Delta x = 3\sigma_x/\mu_x \times 100$, where $\sigma_x$ is the standard deviation and $\mu_x$ is the mean value for parameter $x$. Blank entries are left when data corruption prevents presentation.

Table A.1: Jitter data for all repetition rates and incident pump power combinations with the 5 % output coupler from the benchmark data set.

| Rep. rate (Hz) | Pump power (W) | Build-up time | | | Pulse duration | | | Peak power | | | Pulse energy | | |
|---|---|---|---|---|---|---|---|---|---|---|---|---|---|
| | | $\mu_{\tau_\mathrm{b}}$ (ns) | $3\sigma_{\tau_\mathrm{b}}$ (ns) | $\Delta\tau_\mathrm{b}$ (%) | $\mu_{\tau_\mathrm{p}}$ (ns) | $3\sigma_{\tau_\mathrm{p}}$ (ns) | $\Delta\tau_\mathrm{p}$ (%) | $\mu_{P_\mathrm{p}}$ (kW) | $3\sigma_{P_\mathrm{p}}$ (kW) | $\Delta P_\mathrm{p}$ (%) | $\mu_{E_\mathrm{p}}$ (mJ) | $3\sigma_{E_\mathrm{p}}$ (µJ) | $\Delta E_\mathrm{p}$ (%) |
| 50 | 1.9 | 1500 | 200 | 13 | 250 | 100 | 40 | 0.084 | 0.036 | 43 | 0.026 | 5.9 | 23 |
| | | 1300 | 170 | 13 | 190 | 90 | 48 | 0.2 | 0.12 | 58 | 0.052 | 10 | 20 |
| | 2.2 | 760 | 62 | 8.2 | 97 | 21 | 22 | 0.65 | 0.27 | 42 | 0.1 | 16 | 16 |
| | | 820 | 67 | 8.1 | 93 | 43 | 47 | 1.1 | 0.97 | 85 | 0.1 | 77 | 74 |
| | 2.7 | 410 | 16 | 4.0 | 58 | 13 | 22 | 5.1 | 1.4 | 27 | 0.29 | 40 | 14 |
| | | 440 | 26 | 5.9 | 58 | 12 | 20 | 4.6 | 1.9 | 42 | 0.26 | 50 | 19 |
| | 3.5 | 270 | 11 | 4.1 | 41 | 6.0 | 15 | 11 | 4.3 | 39 | 0.44 | 110 | 26 |
| | | 280 | 7.9 | 2.9 | 40 | 6.8 | 17 | 12 | 3.3 | 28 | 0.47 | 40 | 8.6 |
| | 4.9 | 200 | 8.9 | 4.5 | 32 | 6.1 | 19 | 20 | 5.8 | 29 | 0.62 | 43 | 6.8 |
| | | 190 | 7.6 | 3.9 | 31 | 4.2 | 14 | 23 | 6.5 | 28 | 0.68 | 39 | 5.8 |
| | 6.1 | 190 | 6.5 | 3.4 | 31 | 4.3 | 14 | 25 | 5.9 | 23 | 0.78 | 47 | 6.0 |
| | | 180 | 3.9 | 2.2 | 29 | 3.0 | 10 | 28 | 5.9 | 21 | 0.83 | 62 | 7.5 |
| 125 | 1.9 | 1100 | 85 | 7.7 | 140 | 22 | 16 | 0.48 | 0.36 | 76 | 0.083 | 37 | 45 |
| | | 1700 | 190 | 11 | 180 | 47 | 26 | 0.2 | 0.12 | 59 | 0.042 | 22 | 54 |
| | 2.2 | 770 | 37 | 4.8 | 93 | 25 | 26 | 1.4 | 0.57 | 41 | 0.15 | 31 | 21 |
| | | 860 | 64 | 7.5 | 98 | 55 | 56 | 1.2 | 0.41 | 33 | 0.12 | 34 | 27 |
| | 2.7 | 420 | 16 | 3.9 | 60 | 7.1 | 12 | 5.2 | 1.5 | 28 | 0.33 | 59 | 18 |
| | | 430 | 31 | 7.2 | 59 | 7.8 | 13 | 5.0 | 1.5 | 29 | 0.3 | 47 | 16 |
| | 3.5 | 260 | 12 | 4.6 | 38 | 4.0 | 10 | 12 | 3.5 | 28 | 0.46 | 88 | 19 |
| | | 280 | 13 | 4.6 | 40 | 6.6 | 17 | 12 | 3.7 | 31 | 0.45 | 38 | 8.4 |
| | 4.9 | 180 | 4.8 | 2.6 | 30 | 3.7 | 12 | 27 | 6.1 | 23 | 0.79 | 60 | 7.6 |
| | | 190 | 7.1 | 3.7 | 30 | 3.4 | 11 | 27 | 7.7 | 29 | 0.75 | 81 | 11 |
| | 6.1 | 170 | 5.9 | 3.5 | 28 | 3.5 | 12 | 31 | 8.6 | 27 | 0.88 | 60 | 6.8 |
| | | 170 | 5.7 | 3.3 | 28 | 3.4 | 12 | 32 | 7.8 | 25 | 0.88 | 65 | 7.3 |

Table A.1: Continued.

| Rep. rate (Hz) | Pump power (W) | Build-up time | | | Pulse duration | | | Peak power | | | Pulse energy | | |
|---|---|---|---|---|---|---|---|---|---|---|---|---|---|
| | | $\mu_{\tau_\mathrm{b}}$ (ns) | $3\sigma_{\tau_\mathrm{b}}$ (ns) | $\Delta\tau_\mathrm{b}$ (%) | $\mu_{\tau_\mathrm{p}}$ (ns) | $3\sigma_{\tau_\mathrm{p}}$ (ns) | $\Delta\tau_\mathrm{p}$ (%) | $\mu_{P_\mathrm{p}}$ (kW) | $3\sigma_{P_\mathrm{p}}$ (kW) | $\Delta P_\mathrm{p}$ (%) | $\mu_{E_\mathrm{p}}$ (mJ) | $3\sigma_{E_\mathrm{p}}$ (µJ) | $\Delta E_\mathrm{p}$ (%) |
| 250 | 1.9 | 1600 | 280 | 18 | 250 | 120 | 46 | 0.14 | 0.075 | 52 | 0.057 | 6.4 | 11 |
| | | 1800 | 630 | 34 | 410 | 1600 | 390 | 0.15 | 0.22 | 150 | 0.036 | 44 | 120 |
| | 2.2 | 990 | 89 | 8.9 | 140 | 26 | 19 | 0.37 | 0.12 | 31 | 0.11 | 13 | 11 |
| | | 1100 | 110 | 9.9 | 130 | 16 | 12 | 0.74 | 0.22 | 29 | 0.1 | 24 | 23 |
| | 2.4 | 630 | 38 | 6.1 | 82 | 7.4 | 9.0 | 1.7 | 0.47 | 28 | 0.2 | 19 | 9.4 |
| | | 710 | 34 | 4.8 | 87 | 12 | 13 | 2.3 | 0.5 | 22 | 0.19 | 31 | 16 |
| | 2.7 | 480 | 25 | 5.3 | 65 | 16 | 25 | 3.7 | 0.9 | 24 | 0.3 | 42 | 14 |
| | | 540 | 17 | 3.1 | 62 | 15 | 24 | 4.6 | 1.5 | 34 | 0.26 | 54 | 20 |
| | 2.9 | 410 | 27 | 6.7 | 58 | 7.2 | 12 | 4.6 | 1.3 | 29 | 0.33 | 41 | 12 |
| | | 440 | 17 | 3.9 | 56 | 8.9 | 16 | 5.7 | 1.3 | 22 | 0.32 | 44 | 14 |
| | 3.2 | 350 | 13 | 3.8 | 50 | 6.9 | 14 | 4.7 | 1.4 | 29 | 0.39 | 24 | 6.1 |
| | | 380 | 15 | 3.9 | 51 | 6.5 | 13 | 7.7 | 1.8 | 23 | 0.37 | 48 | 13 |
| | 3.5 | 300 | 14 | 4.7 | 43 | 5.6 | 13 | 7.2 | 2.2 | 31 | 0.44 | 43 | 9.8 |
| | | 320 | 12 | 3.7 | 46 | 6.7 | 15 | 9.0 | 2.6 | 29 | 0.43 | 48 | 11 |
| | 3.8 | 270 | 13 | 5.0 | 40 | 25 | 61 | 10 | 2.3 | 23 | 0.49 | 31 | 6.2 |
| | | 280 | 11 | 3.8 | 40 | 4.8 | 12 | 13 | 4.0 | 31 | 0.48 | 70 | 15 |
| | 4.0 | 240 | 7.5 | 3.1 | 36 | 3.6 | 9.9 | 13 | 3.4 | 27 | 0.55 | 37 | 6.7 |
| | | 260 | 10 | 3.9 | 37 | 4.4 | 12 | 14 | 3.3 | 24 | 0.51 | 60 | 12 |
| | 4.3 | 230 | 6.4 | 2.8 | 34 | 3.4 | 10 | 14 | 2.7 | 19 | 0.6 | 39 | 6.5 |
| | | 240 | 7.9 | 3.3 | 35 | 3.7 | 11 | 17 | 4.2 | 25 | 0.57 | 69 | 12 |
| | 4.6 | 210 | 4.6 | 2.2 | 33 | 4.0 | 12 | 15 | 2.6 | 17 | 0.64 | 32 | 5.0 |
| | | 220 | 7.7 | 3.5 | 33 | 3.7 | 11 | 19 | 4.5 | 23 | 0.63 | 62 | 9.8 |
| | 4.9 | 200 | 5.0 | 2.6 | 31 | 3.9 | 12 | 19 | 3.9 | 21 | 0.72 | 46 | 6.4 |
| | | 210 | 6.1 | 2.9 | 32 | 4.1 | 13 | 21 | 3.9 | 19 | 0.67 | 49 | 7.3 |
| | 6.1 | 180 | 5.7 | 3.2 | 30 | 4.0 | 14 | 25 | 4.4 | 17 | 0.87 | 66 | 7.6 |
| | | 180 | 4.4 | 2.5 | 29 | 3.3 | 11 | 30 | 6.5 | 22 | 0.86 | 110 | 13 |

Table A.1: Continued.

| Rep. | Pump | Build-up time | | | Pulse duration | | | Peak power | | | Pulse energy | | |
|---|---|---|---|---|---|---|---|---|---|---|---|---|---|
| rate (Hz) | power (W) | $\mu_{\tau_\mathrm{b}}$ (ns) | $3\sigma_{\tau_\mathrm{b}}$ (ns) | $\Delta\tau_\mathrm{b}$ (%) | $\mu_{\tau_\mathrm{p}}$ (ns) | $3\sigma_{\tau_\mathrm{p}}$ (ns) | $\Delta\tau_\mathrm{p}$ (%) | $\mu_{P_\mathrm{p}}$ (kW) | $3\sigma_{P_\mathrm{p}}$ (kW) | $\Delta P_\mathrm{p}$ (%) | $\mu_{E_\mathrm{p}}$ (mJ) | $3\sigma_{E_\mathrm{p}}$ (µJ) | $\Delta E_\mathrm{p}$ (%) |
| 500 | 1.9 | 1800 | 1800 | 100 | 1300 | 4000 | 320 | 0.056 | 0.073 | 130 | 0.039 | 15 | 38 |
| | | 2000 | 1400 | 70 | 1700 | 3800 | 230 | 0.048 | 0.099 | 200 | 0.016 | 31 | 200 |
| | 2.2 | 1400 | 260 | 19 | 210 | 140 | 67 | 0.33 | 0.27 | 82 | 0.078 | 26 | 33 |
| | | 1600 | 360 | 22 | 220 | 130 | 58 | 0.21 | 0.2 | 97 | 0.06 | 24 | 40 |
| | 2.7 | 720 | 73 | 10 | 93 | 16 | 18 | 1.7 | 0.52 | 31 | 0.19 | 32 | 17 |
| | | 800 | 68 | 8.5 | 99 | 19 | 19 | 2.0 | 0.68 | 33 | 0.18 | 35 | 19 |
| | 3.5 | 440 | 24 | 5.4 | 58 | 10 | 18 | 5.8 | 1.8 | 32 | 0.34 | 60 | 18 |
| | | 490 | 27 | 5.6 | 66 | 10 | 16 | 5.3 | 1.5 | 28 | 0.31 | 36 | 12 |
| | 4.9 | 270 | 7.7 | 2.8 | 39 | 5.3 | 13 | 14 | 3.9 | 27 | 0.57 | 52 | 9.2 |
| | | 300 | 10 | 3.3 | 43 | 4.7 | 11 | 13 | 2.3 | 18 | 0.53 | 45 | 8.4 |
| | 6.1 | 230 | 7.2 | 3.1 | 36 | 5.1 | 14 | 20 | 4.4 | 21 | 0.74 | 67 | 9.1 |
| | | 250 | 8.3 | 3.4 | 35 | 4.1 | 12 | 21 | 5.0 | 24 | 0.68 | 58 | 8.5 |
| 1000 | 1.9 | 1900 | 1300 | 72 | 1700 | 4000 | 230 | 0.018 | 0.032 | 180 | 0.013 | 9.1 | 70 |
| | | 1900 | 1300 | 69 | 1800 | 3900 | 220 | 0.079 | 0.29 | 370 | 0.016 | 68 | 440 |
| | 2.2 | 1100 | 1400 | 130 | 710 | 1900 | 260 | 0.1 | 0.25 | 240 | 0.032 | 38 | 120 |
| | | 1700 | 1800 | 110 | 1500 | 4100 | 280 | 0.49 | 1.4 | 280 | 0.051 | 210 | 410 |
| | 2.7 | 1200 | 590 | 48 | 180 | 180 | 100 | 0.54 | 0.65 | 120 | 0.1 | 54 | 53 |
| | | 1300 | 320 | 25 | 160 | 83 | 52 | 0.79 | 0.65 | 82 | 0.1 | 53 | 51 |
| | 3.5 | 830 | 80 | 9.6 | 110 | 18 | 17 | 1.1 | 0.32 | 29 | 0.19 | 24 | 12 |
| | | 830 | 120 | 14 | 99 | 27 | 27 | 2.6 | 1.2 | 44 | 0.19 | 66 | 34 |
| | 4.9 | 490 | 26 | 5.4 | 67 | 12 | 18 | 4.0 | 0.98 | 25 | 0.34 | 28 | 8.3 |
| | | 510 | 25 | 4.9 | 66 | 10 | 15 | 6.5 | 1.5 | 22 | 0.37 | 32 | 8.8 |
| | 6.1 | 410 | 15 | 3.8 | 54 | 8.3 | 15 | 7.6 | 2.2 | 29 | 0.47 | 63 | 13 |
| | | 420 | 22 | 5.3 | 55 | 7.3 | 13 | 10 | 2.3 | 23 | 0.49 | 81 | 16 |

Table A.1: Continued.

| Rep. rate (Hz) | Pump power (W) | Build-up time | | | Pulse duration | | | Peak power | | | Pulse energy | | |
|---|---|---|---|---|---|---|---|---|---|---|---|---|---|
| | | $\mu_{\tau_\mathrm{b}}$ (ns) | $3\sigma_{\tau_\mathrm{b}}$ (ns) | $\Delta\tau_\mathrm{b}$ (%) | $\mu_{\tau_\mathrm{p}}$ (ns) | $3\sigma_{\tau_\mathrm{p}}$ (ns) | $\Delta\tau_\mathrm{p}$ (%) | $\mu_{P_\mathrm{p}}$ (kW) | $3\sigma_{P_\mathrm{p}}$ (kW) | $\Delta P_\mathrm{p}$ (%) | $\mu_{E_\mathrm{p}}$ (mJ) | $3\sigma_{E_\mathrm{p}}$ (µJ) | $\Delta E_\mathrm{p}$ (%) |
| 5000 | 2.2 | 1900 | 1600 | 85 | 3000 | 310 | 11 | 3.2e-4 | 1.1e-4 | 36 | 5.2e-4 | 0.039 | 7.6 |
| | | 1900 | 960 | 50 | 1800 | 3600 | 200 | 0.01 | 0.022 | 220 | 0.0023 | 7.6 | 320 |
| | 2.7 | 1900 | 1500 | 80 | 2000 | 3900 | 200 | 0.011 | 0.031 | 280 | 0.008 | 8.5 | 96 |
| | | 1900 | 1300 | 68 | 1800 | 4000 | 220 | 0.03 | 0.11 | 380 | 0.007 | 30 | 380 |
| | 3.5 | 1800 | 1600 | 90 | 1800 | 4100 | 230 | 0.057 | 0.16 | 290 | 0.026 | 38 | 150 |
| | | 1800 | 1600 | 89 | 1500 | 3900 | 260 | 0.14 | 0.45 | 320 | 0.022 | 100 | 470 |
| | 4.9 | 1200 | 1100 | 92 | 730 | 2000 | 270 | 0.27 | 0.83 | 300 | 0.058 | 100 | 180 |
| | | 1700 | 1800 | 100 | 1500 | 4100 | 280 | 0.44 | 1.5 | 350 | 0.059 | 210 | 350 |
| | 6.1 | 1300 | 1100 | 83 | 560 | 1800 | 320 | 0.4 | 1.2 | 300 | 0.079 | 140 | 180 |
| | | 1600 | 2100 | 130 | 1500 | 4100 | 280 | 1.1 | 3.2 | 310 | 0.088 | 390 | 440 |

Table A.2: Jitter data for all repetition rates and incident pump power combinations with the 10 % output coupler from the benchmark data set.

| Rep. rate (Hz) | Pump power (W) | Build-up time | | | Pulse duration | | | Peak power | | | Pulse energy | | |
|---|---|---|---|---|---|---|---|---|---|---|---|---|---|
| | | $\mu_{\tau_\mathrm{b}}$ (ns) | $3\sigma_{\tau_\mathrm{b}}$ (ns) | $\Delta\tau_\mathrm{b}$ (%) | $\mu_{\tau_\mathrm{p}}$ (ns) | $3\sigma_{\tau_\mathrm{p}}$ (ns) | $\Delta\tau_\mathrm{p}$ (%) | $\mu_{P_\mathrm{p}}$ (kW) | $3\sigma_{P_\mathrm{p}}$ (kW) | $\Delta P_\mathrm{p}$ (%) | $\mu_{E_\mathrm{p}}$ (mJ) | $3\sigma_{E_\mathrm{p}}$ (µJ) | $\Delta E_\mathrm{p}$ (%) |
| 50 | 2.2 | 1600 | 160 | 10 | 190 | 29 | 15 | 0.55 | 0.12 | 21 | 0.1 | 16 | 16 |
| | | 2300 | 390 | 17 | 410 | 140 | 35 | 0.071 | 0.042 | 59 | 0.026 | 16 | 62 |
| | 2.7 | 610 | 33 | 5.5 | 73 | 20 | 27 | 7.3 | 3.0 | 41 | 0.34 | 41 | 12 |
| | | 700 | 46 | 6.6 | 90 | 13 | 15 | 3.2 | 1.1 | 35 | 0.29 | 36 | 12 |
| | 3.5 | 340 | 16 | 4.8 | 45 | 7.5 | 17 | 21 | 4.9 | 23 | 0.78 | 94 | 12 |
| | | 330 | 18 | 5.4 | 45 | 6.1 | 14 | 17 | 5.7 | 33 | 0.73 | 83 | 11 |
| | 4.9 | 240 | 11 | 4.6 | 33 | 5.5 | 16 | 39 | 14 | 37 | 1.1 | 89 | 8.3 |
| | | 120 | 370 | 300 | 160 | 360 | 220 | 31 | 11 | 36 | 1.1 | 140 | 12 |
| | 6.1 | 240 | 7.8 | 3.3 | 33 | 3.9 | 12 | 42 | 13 | 32 | 1.2 | 81 | 6.6 |
| | | 210 | 7.4 | 3.5 | 33 | 3.7 | 11 | 40 | 7.1 | 18 | 1.3 | 86 | 6.6 |
| | 7.1 | 330 | 16 | 5.0 | 45 | 5.8 | 13 | 26 | 4.2 | 16 | 1.1 | 130 | 12 |
| | | 260 | 15 | 5.8 | 92 | 340 | 370 | 36 | 8.6 | 24 | 1.2 | 96 | 7.7 |
| 125 | 2.2 | 1800 | 110 | 6 | 170 | 54 | 32 | 0.83 | 0.33 | 40 | 0.15 | 17 | 12 |
| | | 1800 | 130 | 7.2 | 170 | 25 | 15 | 0.9 | 0.32 | 36 | 0.1 | 19 | 19 |
| | 2.7 | 650 | 50 | 7.6 | 75 | 7.3 | 9.7 | 4.1 | 0.78 | 19 | 0.33 | 29 | 8.8 |
| | | 700 | 45 | 6.5 | 80 | 14 | 17 | 44 | 17 | 38 | 3.2 | 470 | 14 |
| | 3.5 | 360 | 27 | 7.4 | 48 | 7.1 | 15 | 14 | 4.5 | 33 | 0.65 | 65 | 9.9 |
| | | 400 | 23 | 5.7 | 50 | 5.8 | 12 | 14 | 5.3 | 37 | 0.66 | 120 | 18 |
| | 4.9 | 240 | 7.7 | 3.2 | 34 | 4.6 | 14 | 36 | 10 | 29 | 1.1 | 67 | 6 |
| | | 250 | 9.4 | 3.7 | 35 | 4.3 | 12 | 32 | 7.6 | 24 | 1.0 | 110 | 10 |
| | 6.1 | 230 | 8.1 | 3.6 | 32 | 3.7 | 12 | 44 | 8.6 | 20 | 1.4 | 86 | 6.4 |
| | | 240 | 9.9 | 4.1 | 34 | 3.9 | 11 | 35 | 10 | 29 | 1.2 | 160 | 14 |
| | 7.1 | 260 | 21 | 8.1 | 36 | 3.8 | 11 | 35 | 7.7 | 22 | 1.3 | 140 | 11 |
| | | 280 | 13 | 4.6 | 39 | 3.8 | 9.9 | 31 | 7.7 | 25 | 1.1 | 100 | 9.7 |
| | 7.8 | 350 | 20 | 5.8 | 48 | 3.8 | 7.9 | 19 | 3.2 | 16 | 1.0 | 110 | 10 |
| | | 370 | 23 | 6.1 | 51 | 3.5 | 6.8 | 19 | 3.5 | 18 | 0.99 | 160 | 16 |

Table A.2: Continued.

| Rep. rate (Hz) | Pump power (W) | Build-up time | | | Pulse duration | | | Peak power | | | Pulse energy | | |
|---|---|---|---|---|---|---|---|---|---|---|---|---|---|
| | | $\mu_{\tau_\mathrm{b}}$ (ns) | $3\sigma_{\tau_\mathrm{b}}$ (ns) | $\Delta\tau_\mathrm{b}$ (%) | $\mu_{\tau_\mathrm{p}}$ (ns) | $3\sigma_{\tau_\mathrm{p}}$ (ns) | $\Delta\tau_\mathrm{p}$ (%) | $\mu_{P_\mathrm{p}}$ (kW) | $3\sigma_{P_\mathrm{p}}$ (kW) | $\Delta P_\mathrm{p}$ (%) | $\mu_{E_\mathrm{p}}$ (mJ) | $3\sigma_{E_\mathrm{p}}$ (µJ) | $\Delta E_\mathrm{p}$ (%) |
| 250 | 2.1 | 1900 | 550 | 29 | 770 | 3000 | 390 | 0.075 | 0.16 | 210 | 0.031 | 31 | 100 |
| | | 2000 | 380 | 19 | 300 | 220 | 71 | 0.29 | 0.22 | 77 | 0.062 | 30 | 48 |
| | 2.7 | | | | | | | | | | | | |
| | | 730 | 46 | 6.3 | 89 | 19 | 21 | 4.2 | 1.4 | 34 | 0.31 | 36 | 12 |
| | 3.5 | 410 | 25 | 6.0 | 52 | 6.4 | 12 | 13 | 3.6 | 29 | 0.62 | 71 | 11 |
| | | 430 | 31 | 7.2 | 54 | 7.6 | 14 | 13 | 3.5 | 26 | 0.64 | 49 | 7.7 |
| | 4.9 | 250 | 6.8 | 2.7 | 35 | 3.7 | 10 | 30 | 6.5 | 22 | 1.0 | 130 | 13 |
| | | 270 | 10 | 3.7 | 37 | 17 | 45 | 28 | 6.1 | 22 | 1.1 | 120 | 11 |
| | 6.1 | 230 | 7.7 | 3.4 | 33 | 3.7 | 11 | 39 | 11 | 27 | 1.3 | 180 | 14 |
| | | 250 | 9.3 | 3.8 | 35 | 3.7 | 10 | 33 | 6.3 | 19 | 1.2 | 140 | 12 |
| | 7.1 | 250 | 10 | 4.1 | 36 | 2.8 | 7.8 | 33 | 4.6 | 14 | 1.3 | 96 | 7.4 |
| | | 290 | 8.5 | 2.9 | 38 | 4.1 | 11 | 31 | 3.5 | 11 | 1.2 | 79 | 6.6 |
| | 7.8 | 310 | 15 | 4.9 | 44 | 7.1 | 16 | 26 | 4.9 | 19 | 1.1 | 200 | 18 |
| | | 390 | 20 | 5.1 | 55 | 6.4 | 12 | 16 | 3.5 | 22 | 0.98 | 130 | 13 |
| 500 | 2.2 | 1700 | 1500 | 86 | 1400 | 4100 | 280 | 0.059 | 0.12 | 200 | 0.039 | 28 | 72 |
| | | 2000 | 1100 | 53 | 1300 | 3700 | 280 | 0.049 | 0.13 | 270 | 0.016 | 34 | 220 |
| | 2.7 | 1100 | 140 | 13 | 140 | 26 | 18 | 0.85 | 0.35 | 41 | 0.2 | 40 | 20 |
| | | 1400 | 220 | 16 | 190 | 35 | 19 | 0.56 | 0.12 | 21 | 0.12 | 12 | 10 |
| | 3.5 | 550 | 46 | 8.4 | 70 | 14 | 20 | 4.7 | 1.4 | 31 | 0.43 | 27 | 6.2 |
| | | 650 | 38 | 6.0 | 81 | 13 | 17 | 4.8 | 1.3 | 27 | 0.4 | 45 | 11 |
| | 4.9 | 320 | 13 | 4.1 | 45 | 7.5 | 17 | 18 | 5.4 | 30 | 0.86 | 42 | 4.9 |
| | | 360 | 17 | 4.7 | 47 | 7.2 | 15 | 17 | 4.1 | 24 | 0.78 | 64 | 8.2 |
| | 6.1 | 280 | 8.4 | 3 | 39 | 6.1 | 16 | 29 | 6.1 | 21 | 1.1 | 46 | 4.2 |
| | | 300 | 11 | 3.6 | 41 | 5.6 | 13 | 27 | 7.5 | 28 | 1.0 | 86 | 8.6 |
| | 7.1 | 300 | 9.9 | 3.3 | 42 | 6.4 | 15 | 27 | 5.7 | 21 | 1.2 | 54 | 4.4 |
| | | 320 | 27 | 8.3 | 43 | 6.1 | 14 | 24 | 5.4 | 23 | 0.99 | 67 | 6.8 |
| | 7.8 | 340 | 17 | 5.1 | 47 | 6.9 | 15 | 23 | 5.6 | 24 | 1.1 | 100 | 9.0 |
| | | 410 | 29 | 7.0 | 54 | 4.5 | 8.3 | 17 | 4.1 | 24 | 0.94 | 120 | 13 |

Table A.2: Continued.

| Rep. rate (Hz) | Pump power (W) | Build-up time | | | Pulse duration | | | Peak power | | | Pulse energy | | |
|---|---|---|---|---|---|---|---|---|---|---|---|---|---|
| | | $\mu_{\tau_\mathrm{b}}$ (ns) | $3\sigma_{\tau_\mathrm{b}}$ (ns) | $\Delta\tau_\mathrm{b}$ (%) | $\mu_{\tau_\mathrm{p}}$ (ns) | $3\sigma_{\tau_\mathrm{p}}$ (ns) | $\Delta\tau_\mathrm{p}$ (%) | $\mu_{P_\mathrm{p}}$ (kW) | $3\sigma_{P_\mathrm{p}}$ (kW) | $\Delta P_\mathrm{p}$ (%) | $\mu_{E_\mathrm{p}}$ (mJ) | $3\sigma_{E_\mathrm{p}}$ (µJ) | $\Delta E_\mathrm{p}$ (%) |
| 1000 | 2.1 | 2100 | 1300 | 64 | 1500 | 3900 | 260 | 0.049 | 0.13 | 260 | 0.026 | 28 | 110 |
| | 2.7 | 950 | 680 | 71 | 790 | 2100 | 260 | 0.81 | 2.3 | 280 | 0.099 | 260 | 260 |
| | | 1400 | 1600 | 110 | 870 | 3700 | 430 | 0.22 | 0.35 | 160 | 0.069 | 57 | 83 |
| | 3.5 | 1000 | 230 | 23 | 120 | 32 | 26 | 1.5 | 0.94 | 63 | 0.24 | 79 | 33 |
| | | 1200 | 210 | 18 | 150 | 48 | 33 | 1.2 | 0.69 | 57 | 0.2 | 52 | 26 |
| | 4.9 | 550 | 48 | 8.8 | 73 | 11 | 16 | 6.1 | 2.2 | 36 | 0.48 | 69 | 14 |
| | | 630 | 63 | 10 | 89 | 18 | 21 | 3.2 | 1.4 | 43 | 0.43 | 52 | 12 |
| | 6.1 | 460 | 30 | 6.5 | 60 | 14 | 23 | 12 | 3.7 | 31 | 0.7 | 48 | 6.9 |
| | | 480 | 46 | 9.6 | 64 | 12 | 19 | 6.7 | 3.0 | 44 | 0.61 | 110 | 17 |
| | 7.1 | 470 | 23 | 5.0 | 63 | 11 | 18 | 12 | 2.6 | 21 | 0.74 | 43 | 5.8 |
| | | 480 | 42 | 8.7 | 66 | 12 | 19 | 7.7 | 2.9 | 37 | 0.72 | 84 | 12 |
| | 7.8 | 590 | 44 | 7.4 | 79 | 14 | 18 | 6.4 | 1.3 | 20 | 0.65 | 46 | 7.0 |
| | | 460 | 32 | 6.9 | 60 | 12 | 20 | 9.0 | 3.1 | 34 | 0.74 | 63 | 8.5 |
| 5000 | 2.7 | 2000 | 1600 | 76 | 2300 | 3200 | 140 | 0.011 | 0.019 | 170 | 0.012 | 6.6 | 55 |
| | | 2000 | 960 | 48 | 2100 | 3400 | 160 | 0.009 | 0.023 | 250 | 0.006 | 9 | 140 |
| | 3.2 | 2000 | 1700 | 85 | 1600 | 4100 | 250 | 0.078 | 0.22 | 280 | 0.036 | 47 | 130 |
| | | 1900 | 1500 | 79 | 1900 | 4000 | 210 | 0.083 | 0.32 | 390 | 0.029 | 84 | 290 |
| | 3.5 | 1900 | 1800 | 93 | 1700 | 4100 | 250 | 0.1 | 0.28 | 280 | 0.042 | 60 | 140 |
| | | 1900 | 1700 | 89 | 2000 | 4000 | 200 | 0.12 | 0.43 | 360 | 0.039 | 110 | 270 |
| | 4.9 | 1700 | 1900 | 110 | 1600 | 4200 | 270 | 0.44 | 1.2 | 280 | 0.1 | 200 | 200 |
| | | 1500 | 1300 | 91 | 1500 | 4200 | 270 | 0.17 | 0.39 | 230 | 0.092 | 61 | 66 |
| | 6.1 | 1700 | 2200 | 130 | 1500 | 4200 | 290 | 0.99 | 2.6 | 260 | 0.15 | 360 | 250 |
| | | 1600 | 1800 | 110 | 1200 | 4000 | 330 | 0.89 | 2.8 | 320 | 0.13 | 290 | 220 |
| | 7.1 | 1600 | 2200 | 140 | 1500 | 4200 | 290 | 1.2 | 3.3 | 270 | 0.17 | 430 | 260 |
| | | 1700 | 1800 | 110 | 1200 | 4000 | 320 | 0.89 | 2.7 | 300 | 0.15 | 330 | 230 |
| | 7.8 | 1600 | 1900 | 110 | 1300 | 4000 | 300 | 2.1 | 5.9 | 290 | 0.16 | 880 | 570 |
| | | 1700 | 1900 | 110 | 1500 | 4200 | 280 | 0.68 | 1.9 | 290 | 0.15 | 240 | 160 |

Table A.3: Jitter data for all repetition rates and incident pump power combinations with the 20 % output coupler from the benchmark data set.

| Rep. rate (Hz) | Pump power (W) | Build-up time | | | Pulse duration | | | Peak power | | | Pulse energy | | |
|---|---|---|---|---|---|---|---|---|---|---|---|---|---|
| | | $\mu_{\tau_\mathrm{b}}$ (ns) | $3\sigma_{\tau_\mathrm{b}}$ (ns) | $\Delta\tau_\mathrm{b}$ (%) | $\mu_{\tau_\mathrm{p}}$ (ns) | $3\sigma_{\tau_\mathrm{p}}$ (ns) | $\Delta\tau_\mathrm{p}$ (%) | $\mu_{P_\mathrm{p}}$ (kW) | $3\sigma_{P_\mathrm{p}}$ (kW) | $\Delta P_\mathrm{p}$ (%) | $\mu_{E_\mathrm{p}}$ (mJ) | $3\sigma_{E_\mathrm{p}}$ (µJ) | $\Delta E_\mathrm{p}$ (%) |
| 50 | 3.2 | 1200 | 140 | 11 | 150 | 63 | 42 | 1.4 | 0.76 | 56 | 0.18 | 43 | 24 |
| | | 1600 | 260 | 16 | 210 | 280 | 130 | 0.37 | 0.17 | 47 | 0.1 | 25 | 24 |
| | 3.5 | 830 | 71 | 8.6 | 100 | 25 | 24 | 3.2 | 0.9 | 28 | 0.34 | 57 | 17 |
| | | 1100 | 97 | 8.9 | 130 | 26 | 20 | 1.7 | 0.62 | 37 | 0.26 | 25 | 9.5 |
| | 4.9 | 410 | 30 | 7.2 | 50 | 12 | 24 | 19 | 8.0 | 42 | 0.83 | 260 | 31 |
| | | 450 | 27 | 5.9 | 54 | 10 | 19 | 14 | 6.4 | 44 | 0.81 | 280 | 35 |
| | 6.1 | 370 | 19 | 5.0 | 46 | 5.3 | 12 | 28 | 10 | 36 | 1.1 | 190 | 17 |
| | | 390 | 32 | 8.2 | 48 | 6.9 | 14 | 19 | 6.0 | 31 | 1.0 | 170 | 16 |
| | 7.1 | 490 | 35 | 7.3 | 61 | 10 | 16 | 15 | 4.0 | 26 | 0.88 | 200 | 22 |
| | | 420 | 29 | 7.0 | 50 | 8.3 | 17 | 20 | 10 | 50 | 0.96 | 190 | 20 |
| 125 | 3.2 | 1800 | 360 | 20 | 200 | 280 | 140 | 0.51 | 0.34 | 66 | 0.11 | 50 | 44 |
| | | 1800 | 260 | 15 | 190 | 94 | 50 | 1.2 | 0.94 | 79 | 0.15 | 120 | 83 |
| | 3.5 | 840 | 120 | 15 | 98 | 27 | 28 | 3.8 | 1.4 | 37 | 0.33 | 48 | 15 |
| | | 1200 | 100 | 9.1 | 130 | 22 | 17 | 2.4 | 0.91 | 37 | 0.3 | 47 | 16 |
| | 4.9 | 480 | 28 | 5.8 | 56 | 8.7 | 15 | 18 | 4.3 | 25 | 0.86 | 75 | 8.7 |
| | | 450 | 22 | 4.9 | 54 | 5.2 | 9.7 | 17 | 3.2 | 19 | 0.89 | 190 | 22 |
| | 6.1 | 380 | 21 | 5.5 | 47 | 3 | 6.4 | 25 | 7.8 | 31 | 1.2 | 180 | 16 |
| | | 400 | 23 | 5.7 | 48 | 3.5 | 7.4 | 27 | 11 | 41 | 1.1 | 200 | 18 |
| | 7.1 | 440 | 40 | 9.2 | 51 | 7.0 | 14 | 20 | 5.5 | 27 | 1.0 | 79 | 7.8 |
| | | 480 | 37 | 7.9 | 55 | 7.1 | 13 | 20 | 6.7 | 33 | 1.0 | 120 | 12 |

Table A.3: Continued.

| Rep. rate (Hz) | Pump power (W) | Build-up time | | | Pulse duration | | | Peak power | | | Pulse energy | | |
|---|---|---|---|---|---|---|---|---|---|---|---|---|---|
| | | $\mu_{\tau_\mathrm{b}}$ (ns) | $3\sigma_{\tau_\mathrm{b}}$ (ns) | $\Delta\tau_\mathrm{b}$ (%) | $\mu_{\tau_\mathrm{p}}$ (ns) | $3\sigma_{\tau_\mathrm{p}}$ (ns) | $\Delta\tau_\mathrm{p}$ (%) | $\mu_{P_\mathrm{p}}$ (kW) | $3\sigma_{P_\mathrm{p}}$ (kW) | $\Delta P_\mathrm{p}$ (%) | $\mu_{E_\mathrm{p}}$ (mJ) | $3\sigma_{E_\mathrm{p}}$ (µJ) | $\Delta E_\mathrm{p}$ (%) |
| 250 | 3.2 | 2100 | 510 | 25 | 210 | 97 | 46 | 0.83 | 0.68 | 82 | 0.15 | 49 | 33 |
| | | 1500 | 420 | 27 | 200 | 360 | 180 | 0.86 | 0.7 | 82 | 0.16 | 74 | 48 |
| | 3.5 | 1200 | 80 | 6.7 | 130 | 17 | 13 | 3.0 | 1.1 | 36 | 0.32 | 41 | 13 |
| | | 1000 | 130 | 13 | 120 | 11 | 9.0 | 1.8 | 0.4 | 22 | 0.29 | 36 | 12 |
| | 4.9 | 460 | 31 | 6.7 | 54 | 5.2 | 9.6 | 17 | 4.6 | 27 | 0.86 | 150 | 18 |
| | | 440 | 28 | 6.4 | 52 | 13 | 25 | 20 | 7.4 | 37 | 0.85 | 65 | 7.7 |
| | 6.1 | 410 | 16 | 4.0 | 48 | 4.3 | 8.9 | 27 | 6.8 | 25 | 1.1 | 150 | 13 |
| | | 380 | 26 | 6.8 | 45 | 5.0 | 11 | 28 | 9.6 | 34 | 1.1 | 130 | 12 |
| | 7.1 | 450 | 30 | 6.8 | 53 | 6.8 | 13 | 22 | 8.7 | 40 | 1.1 | 310 | 29 |
| | | 460 | 41 | 8.9 | 54 | 6.6 | 12 | 19 | 6.6 | 35 | 0.97 | 290 | 30 |
| 500 | 3.2 | 1600 | 490 | 31 | 220 | 570 | 250 | 0.65 | 0.65 | 100 | 0.12 | 120 | 100 |
| | | 2300 | 1100 | 46 | 1100 | 3200 | 300 | 0.16 | 0.35 | 210 | 0.047 | 120 | 260 |
| | 3.5 | 1500 | 410 | 28 | 170 | 42 | 25 | 1.4 | 0.59 | 41 | 0.22 | 75 | 34 |
| | | 1400 | 440 | 32 | 270 | 340 | 130 | 0.92 | 1.2 | 130 | 0.19 | 130 | 69 |
| | 4.9 | 550 | 45 | 8.2 | 81 | 250 | 310 | 12 | 5.7 | 48 | 0.68 | 110 | 17 |
| | | 620 | 45 | 7.3 | 71 | 17 | 23 | 11 | 3.9 | 35 | 0.63 | 190 | 30 |
| | 6.1 | 430 | 28 | 6.5 | 53 | 8.1 | 15 | 18 | 7.9 | 43 | 0.96 | 260 | 27 |
| | | | | | | | | | | | | | |
| | 7.1 | 440 | 27 | 6.2 | 53 | 6.4 | 12 | 20 | 6.8 | 33 | 1.1 | 290 | 27 |
| | | 530 | 38 | 7.1 | 65 | 11 | 16 | 15 | 6.1 | 40 | 0.84 | 170 | 20 |

Table A.3: Continued.

| Rep. rate (Hz) | Pump power (W) | Build-up time | | | Pulse duration | | | Peak power | | | Pulse energy | | |
|---|---|---|---|---|---|---|---|---|---|---|---|---|---|
| | | $\mu_{\tau_\mathrm{b}}$ (ns) | $3\sigma_{\tau_\mathrm{b}}$ (ns) | $\Delta\tau_\mathrm{b}$ (%) | $\mu_{\tau_\mathrm{p}}$ (ns) | $3\sigma_{\tau_\mathrm{p}}$ (ns) | $\Delta\tau_\mathrm{p}$ (%) | $\mu_{P_\mathrm{p}}$ (kW) | $3\sigma_{P_\mathrm{p}}$ (kW) | $\Delta P_\mathrm{p}$ (%) | $\mu_{E_\mathrm{p}}$ (mJ) | $3\sigma_{E_\mathrm{p}}$ (µJ) | $\Delta E_\mathrm{p}$ (%) |
| 1000 | 3.2 | 2000 | 960 | 49 | 1700 | 3700 | 210 | 0.091 | 0.28 | 300 | 0.016 | 85 | 550 |
| | | 2100 | 1200 | 59 | 1500 | 3600 | 240 | 0.14 | 0.44 | 310 | 0.029 | 130 | 470 |
| | 3.5 | 1900 | 1500 | 77 | 1500 | 4100 | 270 | 0.41 | 1.1 | 270 | 0.077 | 250 | 330 |
| | | 1800 | 1600 | 92 | 1600 | 4100 | 260 | 0.42 | 1.2 | 270 | 0.088 | 290 | 320 |
| | 4.9 | 940 | 170 | 18 | 120 | 27 | 23 | 3.2 | 1.4 | 45 | 0.36 | 100 | 28 |
| | | 910 | 150 | 16 | 110 | 22 | 20 | 4.1 | 2.1 | 51 | 0.39 | 170 | 42 |
| | 6.1 | 710 | 92 | 13 | 85 | 15 | 17 | 6.8 | 2.2 | 32 | 0.6 | 160 | 26 |
| | | 670 | 98 | 15 | 81 | 21 | 27 | 8.0 | 2.9 | 36 | 0.6 | 150 | 25 |
| | 7.1 | 640 | 68 | 11 | 84 | 12 | 14 | 8.2 | 2.5 | 31 | 0.69 | 170 | 24 |
| | | 690 | 71 | 10 | 88 | 11 | 12 | 8.1 | 1.9 | 24 | 0.71 | 120 | 17 |
| 5000 | 3.5 | 2100 | 1100 | 54 | 2000 | 3400 | 170 | 0.19 | 0.52 | 270 | 0.013 | 210 | 1600 |
| | | 1800 | 1000 | 55 | 2600 | 2800 | 110 | 0.0062 | 0.011 | 180 | 0.0075 | 3.1 | 42 |
| | 3.8 | 1900 | 1200 | 61 | 1800 | 3900 | 220 | 0.14 | 0.5 | 350 | 0.022 | 130 | 610 |
| | | 1900 | 920 | 47 | 1500 | 3700 | 250 | 0.024 | 0.041 | 170 | 0.023 | 11 | 49 |
| | 4.9 | 1800 | 1600 | 87 | 1400 | 3900 | 270 | 0.39 | 1.2 | 320 | 0.074 | 300 | 400 |
| | | 1700 | 1300 | 77 | 1200 | 3900 | 320 | 0.16 | 0.39 | 240 | 0.069 | 91 | 130 |
| | 6.1 | 1700 | 2000 | 120 | 1500 | 4100 | 270 | 1.3 | 3.6 | 280 | 0.12 | 600 | 490 |
| | | 1600 | 1500 | 98 | 1100 | 3900 | 350 | 0.27 | 0.59 | 220 | 0.11 | 100 | 91 |
| | 7.1 | 1700 | 1900 | 110 | 1500 | 4100 | 270 | 1.1 | 3.7 | 320 | 0.12 | 530 | 430 |
| | | 1500 | 2000 | 130 | 1100 | 4000 | 360 | 0.44 | 0.97 | 220 | 0.15 | 140 | 95 |

# Appendix B

# Benchmark data set - analysis scripts

The following code was used to analyse the benchmark data set. The code is split into four main parts. The first of these, shown in section B.1, is the main file that gets run by the user. This script loops through the output coupling, repetition rate and data run, calling the other functions.

The second function (B.2) imports the data from the specified folder. The data within the folder is organised into csv files named according to the half-wave plate angle used. Also included in the folder is an excel spreadsheet named contents that contains information about each csv file including the length of the file, the pump power corresponding to the half-wave plate angle and the average power recorded. The function returns the data and the pump power and average power for each data set.

Section B.3 shows the PulseParameters function which calculates the pulse parameters from the data and outputs the values for each pulse, the mean value and the standard deviation. The function creates a time axis based on the first waveform it is given and then checks for a pulse in each waveform by comparing the peak of the pulse to the peak of the high-voltage noise. If the pulse is less than 1.5× the noise, it is called a missed pulse and is ignored in the calculation of the mean and standard deviation (the number of missed pulses is kept as another measure of jitter). If a pulse is detected, the function calculates the pulse parameters as described in section 2.3; the build-up time is taken as the time between the peak of the pulse and the peak of the noise, the peak power is the maximum value of the pulse, the energy is the numerical integration (using the trapezoid method) of the area under the pulse and the pulse duration is the Full-Width at Half-Maximum (FWHM) of the pulse. The FWHM is calculated in a separate function included at the end of the PulseParameters function and works by normalising the pulse to 1 and finding the points at which the normalised signal is equal to 0.5. In the event of multiple crossings, the function returns the difference between the first and last crossing. Having calculated the pulse parameters for each pulse in oscilloscope units, the script finds the conversion factor for the energy and peak power using the average power, repetition rate and average area under the pulse. It then converts the power to kW, the energy to mJ and the duration to ns before finding and returning the mean, standard deviation and percentage jitter in each parameter.

The final function is the save function, shown in section B.4, which saves the pulse parameters for each pulse as well as the mean, standard deviation and percentage jitter of each parameter to an excel spreadsheet for each pump power.

## B.1 Main script file:

```matlab
%% Benchmark Analysis v3


% outputs excel files containg pulse parameters per pulse and means & std
% devs

clear
clc

OutputCoupling = {'5%','10%','20%'}; % output couplings to be processed
RepRate = {'050Hz';'125Hz';'250Hz';'500Hz';'1000Hz';'5000Hz'}; % repetition rates to be processed
StartPath = 'N:\BENCHMARK DATA'; % start path of all files
Run = {'run1';'run2'}; % runs to be processed
dirs = regexp(genpath(StartPath),'[^;]*','match'); % start directory

for i = 1:length(OutputCoupling)
    for j = 1:length(RepRate)
        for k = 1:length(Run)
            % find folder of interest by name by checking output coupling,
            % repetition rate and run
            Folder = dirs{~cellfun('isempty',strfind(dirs,OutputCoupling{i})) & ~cellfun('isempty',strfind(dirs,RepRate{j})) & ~cellfun('isempty',strfind(dirs,Run{k}))};

            % Call Import function
            [Data,Ppump,Pavg] = Import(Folder);

```

```
            % Call PulseParameters function
            F = RepRate{j};
            F = str2double(F(1:end-2));
            [PulseParams,Means,Stds,Percents] = PulseParameters(Data,Pavg,F);

            % Call Save function
            Save(Folder,PulseParams,Means,Stds,Percents,Ppump);
        end
    end
end
```

## B.2 Import function:

```
%% Import function

% Imports data from specified folder
function [Data,Ppump,AveragePower] = Import(Folder)

% Read contents file
Contents = [Folder,'\contents.xlsx'];
HWP = xlsread(Contents,'A2:A15');
Ppump = xlsread(Contents,'B2:B15');
WaveformLength = xlsread(Contents,'H2:H15');
AveragePower = xlsread(Contents,'I2:I15');

Data = cell(length(Ppump),1);

for n = 1:length(HWP)
    % create filename
    filename = [Folder,'\',num2str(HWP(n)),'deg ch'];

    % import data from each channel, file not present use NaN
    ID1 = fopen([filename,'1.Wfm.csv']);
    if ID1 == -1
        ch1 = NaN(WaveformLength(n),1);
    else
        ch1 = fscanf(ID1,'%f');
        fclose(ID1);
    end

    ID2 = fopen([filename,'3.Wfm.csv']);
    if ID2 == -1
        ch3 = NaN(WaveformLength(n),1);
    else
        ch3 = fscanf(ID2,'%f');
```

```
        fclose(ID2);
    end

    ID3 = fopen([filename,'4.Wfm.csv']);
    if ID3 == -1
        ch4 = NaN(WaveformLength(n),1);
    else
        ch4 = fscanf(ID3,'%f');
        fclose(ID3);
    end

    % combine data into one array
    data = [ch1,ch3,ch4];

    % calculate number of waveforms and reshape data
    NoWaveforms = length(ch1)/WaveformLength(n);
    Data{n} = reshape(data,WaveformLength(n),NoWaveforms,3);
    clearvars ID1 ID2 ID3 ch1 ch3 ch4

end
end
```

## B.3 PulseParameters function (including FWHM function):

```
%% PulseParameters

function [PulseParams,Means,Stds,Percents] = PulseParameters(Data,
    Pavg,RepRate)

% initialise PulseParams, Means, Stds and Percents cells
PulseParams = cell(length(Data),1);
Means = cell(length(Data),1);
Stds = cell(length(Data),1);
Percents = cell(length(Data),1);

% for each case in Data
for i = 1:length(Data)

    % get data for this loop from cell
    Data_sub = cell2mat(Data(i));

    % Time resolution
    Resolution = 10^-10;

    % WaveformLength from size of data matrix
    WaveformLength = size(Data_sub,1);

    % create time vector t=0 at oscilloscope trigger point (ch1=3V)
    T = NaN(WaveformLength,1);
    ind = find(abs(Data_sub(:,1,1)-3)==min(abs(Data_sub(:,1,1)-3)));
    T(1:ind) = (-(ind-1):0)'*Resolution;
    T(ind:end) = (0:WaveformLength-ind)'*Resolution;

    % initialise variables
    Peak = NaN(size(Data_sub,2),1);
```

```
    tb = NaN(size(Data_sub,2),1);
    tp = NaN(size(Data_sub,2),1);
    Pp = NaN(size(Data_sub,2),1);
    Ep = NaN(size(Data_sub,2),1);

    % find pulse parameters for each waveform
    for j = 1:size(Data_sub,2)

        Peak(j) = max(Data_sub(WaveformLength/4:end,j,2)); % peak of pulse through output coupler
        Noise = max(Data_sub(WaveformLength/4-100:WaveformLength/4,j,2)); % noise level defined by max before PC on
        if Peak(j) >= 1.5*Noise% if peak is not 'visibly' higher than background noise, call it a missed pulse
            ind1 = find(Data_sub(WaveformLength/4:end,j,2)==Peak(j));
            ind2 = find(Data_sub(1:WaveformLength/4,j,2)==max(Data_sub(1:WaveformLength/4,j,2)),1); % find peak of high voltage noise
            tp(j) = findFWHM(T(WaveformLength/4:end),Data_sub(WaveformLength/4:end,j,2)); % call findFWHM, ignore spiking region in signal
            Ep(j) = Resolution*trapz(Data_sub(WaveformLength/4:end,j,2)); % integrate waveform to find area under pulse
            if isempty(ind1)
                tb(j) = NaN; % if no pulse, set build up time to NaN (to be removed later)
            else
                tb(j) = (mean(T(ind1)+T(WaveformLength/4-1))-T(ind2))*10^9; % Build up time in ns (between hi-V noise peak and pulse peak)
            end
        else
            % all NaN for missed pulse
```

```
                tb(j) = NaN;
                tp(j) = NaN;
                Peak(j) = NaN;
                Ep(j) = NaN;
            end
        end

        % calculate V->W conversion factor
        A = Ep; % copy pulse energy values
        A(isnan(A)) = []; % remove NaNs
        Aavg = mean(A); % find average
        C = Pavg(i)/(RepRate*Aavg); % C converts voltage recorded by
            scope to W
        Ep = C.*Ep.*1000; % this converts area in Vs to energy in mJ
        Pp = C.*Peak/1000; % this converts the peak in V to kW
        tp = tp.*10^9; % convert pulse duration to ns

        PulseParams{i} = [tb, tp, Pp, Ep]; % put pulse parameters in to
            cell
        Means{i} = [mean(tb), mean(tp), mean(Pp), mean(Ep)];
        Stds{i} = [std(tb), std(tp), std(Pp), std(Ep)];
        Percents{i} = [3.*std(tb)./mean(tb)*100, 3.*std(tp)./mean(tp)
            *100, 3.*std(Pp)./mean(Pp)*100, 3.*std(Ep)./mean(Ep)*100];
end
end

%% findFWHM function for pulse duration
function FWHM = findFWHM(time,signal)

NormSignal = signal/max(signal); % Normalise so that half max is 0.5

u = 0; % initialise counter

% pre-allocate variables for speed
```

```
m = NaN(length(signal),1);
c  = NaN(length(signal),1);
t  = NaN(length(signal),1);

for v = 2:length(NormSignal)
    if (NormSignal(v) > 0.5 && NormSignal(v−1) < 0.5) || (NormSignal(v) < 0.5 && NormSignal(v−1) > 0.5)
        % if signal crosses 0.5 between 2 points then:
        u = u + 1; % increment counter
        m(u) = (NormSignal(v) − NormSignal(v−1))/(time(v) − time(v−1)); % find gradient between the 2 points (straight line)
        c(u) = NormSignal(v) − m(u) * time(v); % find y−intercept of straight line
        t(u) = (0.5 − c(u)) / m(u); % find time at which NormSignal is exctly 0.5
    end
end

% remove NaNs from t
t(isnan(t)) = [];

if numel(t) < 2
    % if less than 2 elements in t then return NaN
    FWHM = NaN;
else
    % FWHM = difference between 1st and last t
    FWHM = t(u) − t(1);
end

end
```

## B.4 Save function:

```
%% Save function for Benchmark Analysis v3 (LITE)

% saves data to Excel files named by pump power

function Save(Folder, PulseParams, Means, Stds, Percents, Ppump)

for m = 1:length(Ppump)

    % filename
    FileName = [Folder,'\Data for pump power = ',num2str(Ppump(m)),'W.xlsx'];

    % create headers
    PulseParamHead = {'Build-up time (ns)', 'Pulse duration (ns)', 'Peak power (kW)', 'Pulse energy (mJ)'};
    OtherHead = {'Mean value:'; 'Standard dev:'; 'Percent jitter:'};

    % write headers to file
    xlswrite(FileName,PulseParamHead,'A1:D1');
    xlswrite(FileName,PulseParamHead,'G1:J1');
    xlswrite(FileName,OtherHead,'F2:F4');

    % write data to file
    xlswrite(FileName,PulseParams{m},['A2:D',num2str(size(PulseParams{m},1)+1)]);
    xlswrite(FileName,Means{m},'G2:J2');
    xlswrite(FileName,Stds{m},'G3:J3');
    xlswrite(FileName,Percents{m},'G4:J4');

end

end
```

# Bibliography

[1] F. J. McClung and R. W. Hellwarth, “Giant optical pulsations from ruby,” *Journal of Applied Physics*, vol. 33, no. 3, p. 828, 1962.

[2] T. H. Maiman, “Stimulated optical radiation in ruby,” *Nature*, vol. 187, pp. 493–494, 1960.

[3] M. Eichhorn, “Quasi-three-level solid-state lasers in the near and mid infrared based on trivalent rare earth ions,” *Applied Physics B*, vol. 93, pp. 269–316, 2008.

[4] R. C. Stoneman and L. Esterowitz, “Efficient 1.94 µm Tm:YALO laser,” *IEEE Journal of Selected Topics in Quantum Electronics*, vol. 1, no. 1, pp. 78–81, 1995.

[5] E. C. Honea, R. J. Beach, S. B. Sutton, J. A. Speth, S. C. Mitchell, J. A. Skidmore, M. A. Emanuel, and S. A. Payne, “115-W Tm:YAG diode-pumped solid-state laser,” *IEEE Journal of Quantum Electronics*, vol. 33, no. 9, pp. 1592–1600, 1997.

[6] B. M. Walsh, “Review of Tm and Ho materials; spectroscopy and lasers,” *Laser Physics*, vol. 19, no. 4, pp. 855–866, 2009.

[7] N. Fried, “Recent advances in infrared laser lithotripsy,” *Biomedical Optics Express*, vol. 9, no. 9, pp. 4552–4568, 2018.

[8] S. R. Bowman, J. G. Lynn, S. K. Searles, B. J. Feldman, J. McMahon, W. Whitney, D. Epp, G. J. Quarles, and K. J. Riley, “High-average-power operation of a Q-switched diode-pumped holmium laser,” *Optics Letters*, vol. 18, no. 20, pp. 1724–1726, 1993.

[9] R. C. Stoneman and L. Esterowitz, “Efficient, broadly tunable, laser-pumped Tm:YAG and Tm:YSGG cw lasers,” *Optics Letters*, vol. 15, no. 9, pp. 486–488, 1990.

[10] S. W. Henderson, P. J. M. Suni, C. P. Hale, S. M. Hannon, J. R. Magee, D. L. Bruns, and E. H. Yuen, “Coherent laser radar at 2 µm using solid-state lasers,” *IEEE Transactions on Geoscience and Remote Sensing*, vol. 31, no. 1, pp. 4–15, 1993.

[11] Q. Wang, J. Geng, and S. Jiang, “2 µm fiber laser sources for sensing,” *Optical Engineering*, vol. 53, no. 6, p. 061609, 2014.

[12] P. A. Budni, L. A. Pomeranz, M. L. Lemons, C. A. Miller, J. R. Mosto, and E. P. Chicklis, “Efficient mid-infrared laser using 1.9 µm-pumped Ho:YAG and $ZnGeP_2$ optical parametric oscillators,” *Journal of the Optical Society of America B*, vol. 17, no. 5, pp. 723–728, 2000.

[13] P. Černý and D. Burns, “Modeling and experimental investigation of a diode-pumped Tm:$YAlO_3$ laser with *a*- and *b*-cut crystal orientations,” *IEEE Journal of Selected Topics in Quantum Electronics*, vol. 11, no. 3, pp. 674–681, 2005.

[14] K. Mizutani, T. Itabe, S. Ishii, M. Aoki, K. Asai, A. Sato, H. Fukuoka, T. Ishikawa, and K. Noda, “Diode-pumped 2 µm pulse laser with noncomposite Tm,Ho:YLF rod conduction-cooled down to $-80\,^{\circ}$C,” *Applied Optics*, vol. 54, no. 26, pp. 7865–7869, 2015.

[15] A. Godard, “Infrared (2-12 µm) solid-state laser sources: a review,” *Comptes Rendus Physique*, vol. 8, pp. 1100–1128, 2007.

[16] O. Svelto, *Principles of Lasers*, 5th ed. Springer, 2010.

[17] R. G. Smith, “Optical power handling capacity of low loss optical fibres as determined by stimulated Raman and Brillouin scattering,” *Applied Optics*, vol. 11, no. 11, pp. 2489–2494, 1972.

[18] E. P. Ippen, “Low-power quasi-CW Raman oscillator,” *Applied Physics Letters*, vol. 16, no. 8, pp. 303–305, 1970.

[19] U. Sheintop, E. Perez, D. Sebbag, P. Komm, G. Marcus, and S. Noach, “Actively Q-switched tunable narrow bandwidth milli-Joule level Tm:YLF laser,” *Optics Express*, vol. 26, no. 17, pp. 22 135–22 143, 2018.

[20] B. Jalali, V. Raghunathan, R. Shori, S. Fathpour, D. Dimitropoulos, and O. Stafsudd, “Prospects for Silicon Mid-IR Raman Lasers,” *IEEE Journal of Selescted Topics in Quantum Electronics*, vol. 12, no. 6, pp. 1618–1627, 2006.

[21] W. Koechner, *Solid-State Laser Engineering*, 6th ed. Springer, 2006.

[22] D. Welford and P. F. Moulton, “Room-temperature operation of a Co:$MgF_2$ laser,” *Optics Letters*, vol. 13, no. 11, pp. 975–977, 1988.

[23] D. M. Rines, P. F. Moulton, D. Welford, and G. A. Rines, “High-energy operation of a Co:$MgF_2$ laser,” *Optics Letters*, vol. 19, no. 9, pp. 628–630, 1994.

[24] P. P. Sorokin and M. J. Stevenson, “Stimulated infrared emission from trivalent uranium,” *Physical Review Letters*, vol. 5, no. 12, pp. 557–559, 1960.

[25] I. F. Elder and M. J. P. Payne, “Lasing in diode-pumped Tm:YAP, Tm,Ho:YAP and Tm,Ho:YLF,” *Optics Communications*, vol. 145, pp. 329–339, 1998.

[26] I. Baylam, S. Ozharar, and A. Sennaroglu, “1200 nm pumped $Tm^{3+}$:$Lu_2O_3$ ceramic lasers,” *Applied Optics*, vol. 57, no. 8, pp. 1772–1776, 2018.

[27] F. Fusari, S. Vetter, A. A. Lagatsky, B. Richards, S. Calvez, A. Jha, M. D. Dawson, W. Sibbett, and C. T. A. Brown, “Tunable laser operation of a $Tm^{3+}$-doped tellurite glass near 2 µm pumped by a 1211 nm semiconductor disk laser,” *Optical Materials*, vol. 32, no. 9, pp. 1007–1010, 2010.

[28] E. J. Saarinen, E. Vasileva, O. Antipov, J. P. Penttinen, M. Tavast, T. Leinonen, and O. G. Okhotnikov, “2 µm Tm:$Lu_2O_3$ ceramic disk laser intracavity-pumped by a semiconductor disk laser,” *Optics Express*, vol. 21, no. 20, pp. 23 844–23 850, 2013.

[29] D. Creeden, B. R. Johnson, S. D. Setzler, and E. P. Chicklis, “Resonantly pumped Tm-doped fiber laser with >90% slope efficiency,” *Optics Letters*, vol. 39, no. 3, pp. 470–473, 2014.

[30] Y. Tang, F. Li, and J. Xu, “High peak-power gain-switched $Tm^{3+}$-doped fiber laser,” *IEEE Photonics Technology Letters*, vol. 23, no. 13, pp. 893–895, 2011.

[31] X. M. Duan, X. S. Guo, B. Q. Yao, L. H. Zheng, and L. B. Su, “Efficient Ho:$CaF_2$ laser intracavity-pumped by a Tm:LuAG laser in-band pumped at 1.6 µm,” *Laser Physics Letters*, vol. 15, p. 095802, 2018.

[32] P. J. M. Suni and S. W. Henderson, “1-mJ/pulse Tm:YAG laser pumped by a 3-W diode laser,” *Optics Letters*, vol. 16, no. 11, pp. 817–819, 1991.

[33] O. A. Buryy, D. Y. Sugak, S. B. Ubizskii, I. I. Izhnin, M. M. Vakiv, and I. M. Solskii, “The comparative analysis and optimization of the free-running $Tm^{3+}$:YAP and $Tm^{3+}$:YAG microlasers,” *Applied Physics B*, vol. 88, pp. 433–442, 2007.

[34] Jabczynski, J. K. and Zendian, W. and Kwiatkowski, J. and Jelínková, H. and Šulc, J. and Němec, M., “Actively Q-switched, diode pumped thulium laser,” *Laser Physics Letters*, vol. 4, no. 12, pp. 863–867, 2007.

[35] P. A. Budni, M. L. Lemons, J. R. Mosto, and E. P. Chicklis, “High-power/high-brightness diode-pumped 1.9-µm thulium and resonantly pumped 2.1-µm holmium lasers,” *IEEE Journal of Selected Topics in Quantum Electronics*, vol. 6, no. 4, pp. 629–635, 2000.

[36] S. A. Payne, L. L. Chase, L. K. Smith, W. L. Kway, and W. F. Krupke, “Infrared cross-section measurements for crystals doped with $Er^{3+}$, $Tm^{3+}$, and $Ho^{3+}$,” *IEEE Journal of Quantum Electronics*, vol. 28, no. 11, pp. 2619–2630, 1992.

[37] G. Li, H. Liu, F. Lu, X. Wen, Y. Gu, and Y. Wang, “Analysis on preferential free running laser wavelength and performance modeling of $Tm^{3+}$-doped YAP and YLF,” *Applied Optics*, vol. 53, no. 22, pp. 4987–4996, 2014.

[38] H. Kalaycioglu, A. Sennaroglu, and A. Kurt, “Influence of doping concentration on the power performance of diode-pumped continuous-wave $Tm^{3+}$:$YAlO_3$ lasers,” *IEEE Journal of Selected Topics in Quantum Electronics*, vol. 11, no. 3, pp. 667–673, 2005.

[39] A. A. Kaminskii, *Laser Crystals*, 2nd ed. Springer, 1981.

[40] B. Yao, P. Meng, G. LI, Y. Ju, and Y. Wang, “Comparison of Tm:YLF and Tm:YAP in thermal analysis and laser performance,” *Journal of the Optical Society of America B*, vol. 28, no. 8, pp. 1866–1873, 2011.

[41] I. F. Elder and M. J. P. Payne, “YAP versus YAG as a diode-pumped host for thulium,” *Optics Communications*, vol. 148, pp. 265–269, 1998.

[42] M. Schellhorn, “High-power diode-pumped Tm:YLF laser,” *Applied Physics B*, vol. 91, pp. 71–74, 2008.

[43] X. M. Duan, B. Q. Yao, C. W. Song, L. L. Zheng, Y. L. Ju, and Y. Z. Wang, “Diode-pumped high efficient Tm:YLF laser output at 1908 nm with near-diffraction limited beam quality,” *Laser Physics Letters*, vol. 5, no. 5, pp. 347–349, 2008.

[44] S. So, J. I. Mackenzie, D. P. Shepherd, W. A. Clarkson, J. G. Betterton, and E. K. Gorton, “A power-scaling strategy for longitudinally diode-pumped Tm:YLF lasers,” *Applied Physics B*, vol. 84, pp. 389–393, 2006.

[45] X. Peng, L. Xu, and A. Asundi, “High-power efficient continuous-wave $TEM_{00}$ intracavity frequency-doubled diode-pumped Nd:YLF laser,” *Applied Optics*, vol. 44, no. 5, pp. 800–807, 2005.

[46] M. J. Weber, M. Bass, K. Andringa, R. R. Monchamp, and E. Comperchio, “Czochralski growth and properties of $YAlO_3$ crystals,” *Applied Physics Letters*, vol. 15, no. 10, pp. 342–345, 1969.

[47] Y. Lu, J. Wang, Y. Yang, Y. Dai, A. Dong, and B. Sun, “Growth and optical properties of Tm:$YAlO_3$ single crystals with different Tm concentrations,” *Journal of Alloys and Compounds*, vol. 429, pp. 296–300, 2007.

[48] I. F. Elder and J. Payne, "Diode-pumped, room-temperature Tm:YAP laser," *Applied Optics*, vol. 36, no. 33, pp. 8606–8610, 1997.

[49] E. Lippert, S. Nicolas, G. Arisholm, K. Stenerson, and G. Rustad, "Midinfrared laser source with high power and beam quality," *Applied Optics*, vol. 45, no. 16, pp. 3839–3845, 2006.

[50] M. Ganija, N. Simakov, A. Hemming, J. Haub, P. Veitch, and J. Munch, "Efficient, low threshold, cryogenic Ho:YAG laser," *Optics Express*, vol. 24, no. 11, pp. 11 569–11 577, 2016.

[51] S. W. Henderson, C. P. Hale, J. R. Magee, M. J. Kavaya, and A. V. Huffaker, "Eye-safe coherent laser radar system at 2.1 µm using Tm,Ho:YAG lasers," *Optics Letters*, vol. 16, no. 10, pp. 773–775, 1991.

[52] T. Y. Fan, G. Huber, R. L. Byer, and P. Mitzscherlich, "Spectroscopy and diode laser-pumped operation of Tm,Ho:YAG," *IEEE Journal of Quantum Electronics*, vol. 24, no. 6, pp. 924–933, 1988.

[53] X. M. Duan, B. Q. Yao, G. Li, T. H. Wang, X. T. Yang, Y. Z. Wang, G. J. Zhao, and Q. Dong, "High efficient continuous wave operation of a Ho:YAP laser at room temperature," *Laser Physics Letters*, vol. 6, no. 4, pp. 279–281, 2009.

[54] E. Ji, Q. Liu, Y. Shen, M. Nie, and X. Fu, "Generation of Watt-level 2.06 µm polarized light from a diode wing-pumped Ho:YLF laser," *IEEE Photonics Technology Letters*, vol. 29, no. 19, pp. 1695–1698, 2017.

[55] G. A. Newburgh, A. Word-Daniels, A. Michael, L. D. Merkle, A. Ikesue, and M. Dubinskii, "Resonantly diode-pumped $Ho^{3+}$:$Y_2O_3$ ceramic 2.1 µm laser," *Optics Express*, vol. 19, no. 4, p. 140422, 2011.

[56] S. Lamrini, P. Koopmann, M. Schäfer, K. Scholle, and P. Fuhrberg, "Efficient high-power Ho:YAG laser directly in-band pumped by a GaSb-based laser diode stack at 1.9 µm," *Applied Physics B*, vol. 106, pp. 315–319, 2012.

[57] M. E. Storm and W. W. Rohrbach, "Single-longitudinal-mode lasing of Ho:Tm:YAG at 2.091 µm," *Applied Optics*, vol. 28, no. 23, pp. 4965–4967, 1989.

[58] L. J. Li, B. Q. Yao, C. W. Song, Y. Z. Wang, and Z. G. Wang, "Continuous wave and AO Q-switch operation Tm,Ho:YAP laser pumped by a laser diode of 798 nm," *Laser Physics Letters*, vol. 6, no. 2, pp. 102–104, 2009.

[59] J. J. Degnan, "Theory of the optimally Q-switched laser," *IEEE Journal of Quantum Electronics*, vol. 25, no. 2, pp. 214–220, 1989.

[60] T. Y. Fan and R. L. Byer, "Modeling and CW operation of a quasi-three-level 946 nm Nd:YAG laser," *IEEE Journal of Quantum Electronics*, vol. 23, no. 5, pp. 605–612, 1987.

[61] M. Siebold, M. Loeser, U. Schramm, J. Koerner, M. Wolf, M. Hellwing, J. Hein, and K. Ertel, "High-efficiency, room-temperature nanosecond Yb:YAG laser," *Optics Express*, vol. 17, no. 22, pp. 19 887–19 893, 2009.

[62] A. E. Siegman, *Lasers.* University Science Books, 1986.

[63] W. R. Sooy, "The natural selection of modes in a passively Q-switched laser," *Applied Physics Letters*, vol. 7, no. 2, pp. 36–37, 1965.

[64] S. Hooker and C. Webb, *Laser Physics.* Oxford University Press, 2010.

[65] W. G. Wagner and B. A. Lengyel, "Evolution of the giant pulse in a laser," *Journal of Applied Physics*, vol. 34, no. 7, pp. 2040–2046, 1963.

[66] Y. Zhang, B. Yao, T. Dai, H. Shi, L. Han, Y. Shen, and Y. Ju, "Electro-optically cavity-dumped 3 ns Tm:LuAG laser," *Applied Optics*, vol. 55, no. 11, pp. 2848–2851, 2016.

[67] C. Liu, S. Zhao, Y. Li, K. Yang, M. Li, G. Li, D. Li, T. Li, W. Qiao, T. Feng, X. Chen, L. Zheng, L. Su, and J. Xu, "Stable kilo-hertz electro-optically Q-switched Tm,Ho:YAP laser at room temperature," *Optics and Laser Technology*, vol. 81, pp. 189–193, 2016.

[68] G. Martin, T. J. Siemers, and J. R. Thompson, "Modeling structural features of pulse timing jitter in a single-mode, Q-switched, Nd:YAG laser," *Laser Physics*, vol. 27, p. 085005, 2017.

[69] J. Qiao, S. Zhao, K. Yang, W. Song, W. Qiao, C. Wu, J. Zhao, G. Li, D. Li, T. Li, H. Liu, and C. Lee, "High-quality 2 µm Q-switched pulsed solid-state lasers using spin-coating-coreduction approach synthesized $Bi_2Te_3$ topological insulators," *Photonics Research*, vol. 6, no. 4, pp. 314–320, 2018.

[70] Y. Lin, P. Lee, J. Xu, C. Wu, C. Chou, C. Tu, C. Tu, M. Chou, and C. Lee, "High-pulse-energy topological insulator $Bi_2Te_3$-based passive Q-switched solid-state laser," *IEEE Photonics Journal*, vol. 8, no. 4, p. 1502710, 2016.

[71] H. Lee, K. Kim, and H. Kim, "Pulse-amplitude equalization of rational harmonic mode-locked fiber laser using a semiconductor optical amplifier loop mirror," *Optics Communications*, vol. 160, no. 1-3, pp. 51–56, 1999.

[72] Mateos, X. and Loiko, P. and Lamrini, S. and Scholle, K. and Fuhrberg, P. and Suomalainen, S. and Härkönen, A. and Guina, M. and Vatnik, S. and Vedin, I. and Aguiló, M. and Díaz, F. and Wang, Y. and Griebner, U. and Petrov, V., "Ho:KY$(WO_4)_2$ thin-disk laser passively Q-switched by a GaSb-based SESAM," *Optics Express*, vol. 26, no. 7, pp. 9011–9016, 2018.

[73] H. P. H. Cheng, P. Tidemand-Lichtenberg, O. B. Jensen, P. E. Anderson, P. M. Petersen, and C. Pedersen, "Experimental investigation of relative timing jitter in passively synchronized Q-switched lasers," *Optics Letters*, vol. 36, no. 3, pp. 415–417, 2011.

[74] *SPOT datasheet*, Elforlight Ltd., URL: http://www.elforlight.com/_assets/PDF/DataSheets/SPOT.pdf, accessed 12/10/18.

[75] *HELIOS datasheet*, Coherent, URL: https://edge.coherent.com/assets/pdf/COHR_HELIOS_DS_0217_3.pdf, accessed 12/10/18.

[76] *Q-smart 450 & 850 brochure*, Quantel Laser, URL: https://www.quantel-laser.com/tl_files/client/MY%20QUANTEL%20SPACE/Sales%20Literature/Q-smart_Brochure_EN_012016.pdf, accessed 12/10/18.

[77] *Terra datasheet*, Continuum, URL: http://www.continuumlasers.com/images/stories/products/downloads/terra/terra_rev_E.pdf, accessed 12/10/18.

[78] *Q-switched lasers datasheet*, Laser 2000, URL: https://www.laser2000.co.uk/getmedia/2db8dde9-38bc-4daf-b583-832d011d11fe/QL-Datasheet.pdf, accessed 12/10/18.

[79] Y. Sato and T. Taira, "Spectroscopic properties of neodymium-doped yttrium orthovanadate single crystals with high-resolution measurement," *Japanese Journal of Applied Physics*, vol. 41, pp. 5999–6002, 2002.

[80] G. Li, Z. Zhao, K. Yan, D. Li, and J. Zou, "Pulse shape symmetry and pulse width reduction in diode-pumped doubly Q-switched Nd:$YVO_4$/KTP green laser with AO and GaAs," *Optics Express*, vol. 13, no. 4, pp. 1178–1187, 2005.

[81] Y. Sun, Y. Bai, L. Diao, L. Hou, B. Bai, Y. Gong, L. Yu, and J. Bai, "946 nm Nd:YAG double Q-switched laser based on monolayer $WSe_2$ saturable absorber," *Optics Express*, vol. 25, no. 18, pp. 3549–3551, 2017.

[82] T. Chen, K. Chang, J. Chen, J. Lin, and M. Wei, "Role of modulation frequency in a hybrid Q-switched Nd:$LuVO_4$ laser with an acousto-optic modulator and a $Cr^{4+}$:YAG saturable absorber," *Applied Optics*, vol. 53, no. 16, pp. 3459–3464, 2014.

[83] X. Wang and Z. Xu, “Timing jitter reduction and single-frequency operation in an acousto-optic Q-switched Cr,Nd:YAG laser,” *Applied Optics*, vol. 45, no. 33, pp. 8477–8483, 2006.

[84] B. Cole, L. Goldberg, C. W. Trussell, A. Hays, B. W. Schilling, and C. McIntosh, “Reduction of timing jitter in a Q-Switched Nd:YAG laser by direct bleaching of a $Cr^{4+}$:YAG saturable absorber,” *Optics Express*, vol. 17, no. 3, pp. 1766–1771, 2009.

[85] M. Hercher, “Single-mode operation of a Q-switched ruby laser,” *Applied Physics Letters*, vol. 7, no. 2, pp. 39–41, 1965.

[86] J. Dong and K. Ueda, “Longitudinal-mode competition induced instabilities of $Cr^{4+}$,$Nd^{3+}$: $Y_3Al_5O_{12}$ self-Q-switched two-mode laser,” *Applied Physics Letters*, vol. 87, no. 15, p. 151102, 2005.

[87] M. Gong, Y. Wang, D. Wang, and Y. Liao, “Stable 100 kHz operation of passively Q-switched microchip laser,” *Electronics Letters*, vol. 42, no. 13, pp. 760–762, 2006.

[88] A. Steinmetz, D. Nodop, A. Martin, J. Limpert, and A. Tünnermann, “Reduction of timing jitter in passively Q-switched microchip lasers using self-injection seeding,” *Optics Letters*, vol. 35, no. 17, pp. 2885–2887, 2010.

[89] C. Bollig, W. A. Clarkson, and D. C. Hanna, “Stable high-repetition-rate single-frequency Q-switched operation by feedback suppression of relaxation oscillation,” *Optics Letters*, vol. 20, no. 12, pp. 1383–1385, 1995.

[90] D. C. Hanna, B. Luther-Davies, H. N. Rutt, and R. C. Smith, “A two-step Q-switching technique for producing high power in a single longitudinal mode,” *Opto-Electronics*, vol. 3, no. 4, pp. 163–169, 1971.

[91] D. C. Hanna, B. Luther-Davies, and R. C. Smith, “Active Q-switching technique for producing high laser power in a single longitudinal mode,” *Electronics Letters*, vol. 8, no. 15, pp. 369–370, 1972.

[92] D. C. Hanna and Y.-W. J. Koo, “Stable single-mode operation of a Q-switched laser by a simple resonator length control technique,” *Optics Communications*, vol. 43, no. 6, pp. 414–418, 1982.

[93] D. W. Scott, “On optimal and data-based histograms,” *Biometrika*, vol. 66, no. 3, pp. 605–610, 1979.

[94] D. Stothard, C. Rae, and M. Dunn, “An intracavity optical parametric oscillator with very high repetition rate and broad tunability based upon room temperature periodically poled MgO:LiNbO$_3$ with fanned grating design,” *IEEE Journal of Quantum Electronics*, vol. 45, no. 3, pp. 256–263, 2009.

[95] J. Dong, A. Shirakawa, and K. Ueda, “Switchable pulses generation in passively Q-switched multilongitudinal-mode microchip laser,” *Laser Physics Letters*, vol. 4, no. 2, pp. 109–116, 2007.

[96] Y. Lang, Y. Chen, H. Zhang, J. Xin, W. Ge, L. Liao, and Z. Fan, “Passively Q-switched laser based on Nd:YAG/YAG Polygonal Active Mirror with timing jitter improvement,” *Optics Communications*, vol. 435, pp. 81–87, 2019.

[97] C. D. Salzberg and J. J. Villa, “Infrared refractive indexes of silicon germanium and modified selenium glass,” *Journal of the Optical Society of America*, vol. 47, pp. 244–246, 1957.

[98] D. E. Zelmon, D. L. Small, and R. Page, “Refractive-index measurements of undoped yttrium aluminum garnet from 0.4 to 5.0 µm,” *Applied Optics*, vol. 37, pp. 4933–4935, 1998.

[99] T. K. Liang and H. K. Tsang, “Role of free carriers from two-photon absorption in Raman amplification in silicon-on-insulator waveguides,” *Applied Physics Letters*, vol. 84, no. 15, pp. 2745–2747, 2004.

[100] R. Claps, V. Ragunathan, D. Dimitropoulos, and B. Jalali, “Influence of nonlinear absorption on Raman amplification in Silicon waveguides,” *Optics Express*, vol. 12, no. 12, pp. 2774–2780, 2004.

[101] R. Claps, D. Dimiitropoulos, and B. Jalali, “Stimulated Raman scattering in silicon waveguides,” *Electronics Letters*, vol. 38, no. 22, pp. 1352–1354, 2002.

[102] G. J. Dixon, “OEM markets open to diode-based visible lasers,” *Laser Focus World*, vol. 33, no. 4, p. 85, 1997.

[103] SpectralCalc.com high-resolution spectral modeling, http://www.spectralcalc.com/info/about.php, accessed 16/11/18.

[104] H. N. Chaudhry, B. R. Hughes, and S. A. Ghani, “A review of heat pipe systems for heat recovery and renewable energy applications,” *Renewable and Sustainable Energy Reviews*, vol. 16, pp. 2249–2259, 2012.

[105] K. S. Udell, “Heat transfer in porous media considering phase change and capillary - the heat pipe effect,” *International Journal Of Heat And Mass Transfer*, vol. 28, no. 2, pp. 485–495, 1985.

[106] S. W. Henderson, E. H. Yuen, and E. S. Fry, “Fast resonance-detection technique for single-frequency operation of injection-seeded Nd:YAG lasers,” *Optics Letters*, vol. 11, no. 11, pp. 715–717, 1986.

[107] T. Schröder, C. Lemmerz, O. Reitebuch, M. Wirth, C. Wührer, and R. Treichel, “Frequency jitter and spectral width of an injection-seeded Q-switched Nd:YAG laser for a Doppler wind lidar,” *Applied Physics B*, vol. 87, no. 3, pp. 437–444, 2007.

[108] G. J. Koch, M. Petros, J. Yu, and U. N. Singh, “Precise wavelength control of a single-frequency pulsed Ho:Tm:YLF laser,” *Applied Optics*, vol. 41, no. 9, pp. 1718–1721, 2002.

[109] I. Ciapurin, D. Drachenberg, V. Smirnov, G. Venus, and L. Glebov, “Modeling of phase volume diffractive gratings, part 2: reflecting sinusoidal uniform gratings, Bragg mirrors,” *Optical Engineering*, vol. 51, no. 5, 2012.